UC Riverside
UC Riverside Electronic Theses and Dissertations

Title
The Acoustoelectric and Electric Characterization of Single Layer Transition Metal Dichalcogenides

Permalink
https://escholarship.org/uc/item/37g2t9nz

Author
Preciado, Edwin

Publication Date
2017

Peer reviewed|Thesis/dissertation

eScholarship.org Powered by the California Digital Library
University of California

UNIVERSITY OF CALIFORNIA
RIVERSIDE

The Acoustoelectric and Electric Characterization of Single Layer Transition Metal Dichalcogenides

A Dissertation submitted in partial satisfaction
of the requirements for the degree of

Doctor of Philosophy

in

Materials Science and Engineering

by

Edwin Sabas Preciado

March 2017

Dissertation Committee:
Dr. Ludwig Bartels, Chairperson
Dr. Suveen N. Mathaudhu
Dr. Eric Chronister

Copyright by
Edwin Sabas Preciado
2017

The Dissertation of Edwin Sabas Preciado is approved:

____

____

____

Committee Chairperson

University of California, Riverside

Acknowledgment

My graduate school journey was made possible with the support of my lab cohort and family. I would like to take a moment to thank my colleagues and acknowledge the support of everyone throughout these past four years. Without you, this journey in pursuit of my Ph.D. would not be possible. I am eternally grateful for those of you who stood by me and supported me along the way.

Prof. Ludwig Bartels, thank you for lighting my academic path and granting me this opportunity. I still recall the day I came to your office, uncertain of what the future had in store for me. Fortunately, a surprise was at hand as you opened up a door with an invitation to be part of something bigger: an opportunity to enroll in the Materials Science and Engineering Ph.D. program and to be part of your research group. Your endless patience, support, and encouragement motivated me throughout my time researching and writing this dissertation. I cannot thank you enough for being my advisor and mentor for my Ph.D. study. To my doctoral dissertation committee members, Prof. Suveen N. Mathaudhu and Prof. Eric Chronister, a sincere thank you for your time in providing me guidance and feedback.

Prof. Hubert J. Krenner, thank you for granting me the opportunity to conduct research in an excellent working environment and for welcoming me on such short notice to the University of Augsburg. You always had an open ear for questions and were a constant source of suggestions. A hearty thanks to Florian Schülein for mentoring me throughout my time at Experimental Physics I and for all the memorable adventures we had. Not to forget, of course, Mr. Andreas Spörhase, Prof. Achim Wixforth, Mr. Alexander Hupfer, Jörg Kinzel, Moritz Mangold, Jens Pustiowski, Stephan Kapfinger, Matthias Weiß, Lisa Janker, Sebastian Hammer, and Wladislaw Michailow, as well as all other current and former members of Experimental Physics I. Thank you all for the welcoming atmosphere, the help, and the many unforgettable conversations we had in the coffee room.

I would also like to thank my fellow lab mates at UC Riverside, who have accompanied me over the years through their studies; in no particular order: John Mann, Dezheng Sun, Quan Ma, Chen Wang, Jon Wyrick, Greg Pawin, Sarah Bobek, Yeming Zhu, Wenhao Lu, Velveth Klee, Miguel Isarraraz, Koichi Yamaguchi, Michelle Wurch, Ariana Nguyen, David Barroso, KatieMarie Magnone, I-Hsi Daniel Lu, Mike Valentin, Tammy Huang, Joe Martinez, Tom Empante, Michael Gomez, Cindy Merida, Brandon Davis, Ingrid Liao, Gretel von Son, Paulo Fonseca, Kortney Almeida, Sahar Naghibi, Adam Berges, Alison Guan, Aimee Martinez, Natalie Duong, Ariana Naghibi, Hannah Oteng-Quarshie, Dominic Martinez, William Coley, Raymond Acosta, and Edward Benavidez. Truly, it was an amazing experience being a mentee, mentor, colleague, and friend to this group of brilliant researchers.

CNSE cleanroom staff members, thank you for your highly valued technical support that allowed me to learn all of the intricate steps necessary to fabricate complex devices. All was made possible with the guidance of Mark Heiden, Frank Lee, Dexter Humphrey, John Butler, and Dong Yan. Thank you for placing your trust and confidence in my abilities to undertake underlying semiconductor-manufacturing steps.

Mr. Steven Davis and Global Ed Programs, thank you for granting me the opportunity to intern for a six week period with Azcatec on various projects and for coaching me on addressing challenges of working in an international workforce while in Seville, Spain.

Mrs. Angela Newman and Mrs. Martha Topik, thank you for helping me see my true potential, believing in me, and guiding me throughout the AVID program. I was the first in my family to attend college, in part due to your tremendous help. I wouldn't have arrived where I am today without your commitment to excellence, diversity, and outreach.

Mr. Scott Dukes and Mrs. Barbara Barry, thank you for being the spark that electrified my curiosity in science during my time at Newport Harbor High School. You both instilled a passion for teaching and inspired ingenuity, and to this day, I reminisce about all the wonderful experiences that I had as a student in your classrooms, soaking in as much knowledge as possible.

Mr. Todd Deutsch, thank you for all the support and guidance during my time in elementary school. You brought hope to many students at such a young age and embodied the importance of attending a four-year university. Thank you for believing in all of us, and for strengthening our belief that anything is possible if you put your mind to it.

Thank you to my best friends, whom I consider brothers: Carlos Cardenas, David Kufeji, Joseph Smith, Steven Nathan, and Brenton Sherron. Thank you for continuously being by my side and for all the spontaneous and scenic adventures. The endless support you bring to my life is irreplaceable.

Finally, I would also like to thank my parents Maria and Jose Preciado, my sister Stephanie Preciado, and my girlfriend Stephanie Sanchez. Thank you for your patience and inspiring enthusiasm, and for always believing in me. I am the person I am today because of you, and I just want to tell you thank you and I love you. Additionally, I write in memory of my late uncle George Preciado and my grandfather John Preciado, who instilled in me the importance of education. Always you will be by my side and I hope I made you proud. As a great mentor once famously said: Do. Or do not. There is no try.

This work was supported by the US National Science Foundation (NSF) under grant no. ECCS- 1435703, by the Deutsche Forschungsgemeinschaft (DFG) via the Emmy Noether Program (KR3790/2), by the Excellence Initiative of the German Federal Government via the Cluster of Excellence Nanosystems Initiative Munich (NIM), and by the Bavaria-California Technology Center (BaCaTeC). Additional support originates from C-SPIN, part of STARnet, a Semiconductor Research Corporation program sponsored by MARCO and DARPA. I gratefully acknowledge fellowship support under DGE-1326120.

Dedication

I dedicate this dissertation to my beloved mother Maria Preciado and my humble father Jose Preciado, my amazing sister Stephanie Preciado, and my lovely girlfriend Stephanie Sanchez

ABSTRACT OF THE DISSERTATION

The Acoustoelectric and Electric Characterization of Single Layer Transition Metal Dichalcogenides

by

Edwin Sabas Preciado

Doctor of Philosophy, Materials Science and Engineering
University of California, Riverside, March 2017
Dr. Ludwig Bartels, Chairperson

The acoustoelectric effect in single-layer molybdenum disulfide (MoS_2) and tungsten diselenide (WSe_2) is studied in a hybrid setup. Such effects, which rely on the transfer of momentum from surface acoustic waves (SAWs), are generated on the surface of lithium niobate ($LiNbO_3$) to the carriers in MoS_2 and WSe_2, resulting in an attenuation and velocity shift of the wave and giving rise to an acoustoelectric current. This dissertation examines the feasibility of integrating high-quality, single-layer MoS_2 and WSe_2 onto $LiNbO_3$ to ultimately fabricate and characterize a hybrid chip that combines the functionality of a field-effect transistor (FET) and SAW device. MoS_2 and WSe_2 were synthesized by chemical vapor deposition (CVD) directly onto a chemically-reduced $LiNbO_3$ substrate. $LiNbO_3$ is a ferroelectric material that offers a unique blend of piezoelectric and birefringent properties, yet it lacks both optical activity and semiconductor transport. The prototypical device exhibits electrical characteristics that are competitive with MoS_2 and WSe_2 devices on silicon. These results demonstrate both a sound-driven battery and an acoustic photodetector, and ultimately open directions to non-invasive investigation of electrical properties of

single-layer films. The experiments reveal close agreement between transport measurements utilizing conventional contacts and SAW spectroscopy. This approach will set forth the possibility of contact-free transport characterization of two-dimensional (2D) transition metal dichalcogenides (TMD) films, avoiding such concerns as the role of charge transfer at contacts as an artifact of such measurements.

Table of Contents

Acknowledgment iv
Dedication vii
ABSTRACT OF THE DISSERTATION viii
Table of Contents x
List of Tables xiii
List of Figures xiv
List of Equations xx
List of Publications xxii
1 Introduction 1
1.1 Introduction 1
1.2 Two-Dimensional Materials 2
1.3 Transition Metal Dichalcogenides 2
1.3.1 Molybdenum Disulfide 3
1.3.2 Tungsten Diselenide 6
1.4 Surface Acoustic Waves 7
1.4.1 Piezoelectricity 8
1.4.2 The Piezoelectric Effect 9
1.4.3 Piezoelectric Materials 10
1.4.4 Interdigital Transducer 10
1.4.5 Substrate Selection 11
1.5 The Acoustoelectric Phenomena 12
1.5.1 Acoustoelectric Effect in Semiconductors 13
1.5.2 Acoustoelectric Effect in Two-Dimensional Electron Gases 13
1.6 Motivation 15
1.7 Summary and Outline 16
1.8 References 21
2 Experimental Techniques 26
2.1 Introduction 26
2.2 Materials and Structural Characterization Techniques 26
2.2.1 Raman Spectroscopy 27
2.2.2 Photoluminescence Spectroscopy 28
2.3 Fabrication Techniques 28

2.3.1 Lithography ... 28
2.4 Chemical Vapor Deposition ... 30
2.5 Generation and Detection of SAWs ... 30
2.5.1 Generating SAWs ... 30
2.5.2 Network Analyzer ... 31
2.6 Transport Setup ... 31
2.7 Optical Setup ... 32
2.8 References ... 38
3 Hybrid SAW-FET MoS_2 ... 39
3.1 Introduction ... 39
3.2 Experimental Methods ... 39
3.2.1 Sample Preparation of Single-Layer MoS_2 ... 40
3.2.2 Raman Characterization of Single-Layer MoS_2 ... 40
3.2.3 PL Characterization of Single-Layer MoS_2 ... 41
3.2.4 Lithographic Patterning ... 42
3.2.5 Measurement Techniques ... 43
3.3 Experimental Results ... 44
3.3.1 Device Layout ... 44
3.3.2 Post Spatial Map of Single-Layer MoS_2 ... 45
3.3.3 FET Characterization of Single-Layer MoS_2 ... 45
3.3.4 Acoustoelectric Characterization of Single-Layer MoS_2 ... 47
3.4 Conclusion ... 49
3.5 References ... 59
4 Hybrid SAW-FET WSe_2 ... 61
4.1 Introduction ... 61
4.2 Experimental Methods ... 62
4.2.1 Sample Preparation of Single-Layer WSe_2 ... 62
4.2.2 Raman Characterization of Single-Layer WSe_2 ... 63
4.2.3 PL Characterization of Single-Layer WSe_2 ... 64
4.2.4 Lithographic Patterning ... 65
4.2.5 Measurement Techniques ... 66
4.3 Experimental Results ... 66
4.3.1 Post Spatial PL Map of Single-Layer WSe_2 ... 67
4.3.2 FET Characterization of Single-Layer WSe_2 ... 67
4.3.3 Acoustoelectric Characterization of Single-Layer WSe_2 ... 69
4.4 Conclusion ... 71
4.5 References ... 79

5 Acoustic Photodetector MoS_2 ... 81
5.1 Introduction ... 81
5.2 Experimental Methods ... 82
5.2.1 Measurement Techniques ... 83
5.3 Experimental Results ... 83
5.3.1 SAW Attenuation ... 83
5.3.2 SAW Transmission Photoresponse of Single-Layer MoS_2 ... 85
5.3.3 Photoconductance of Single-Layer MoS_2 ... 85
5.3.4 Optical Pump Series of Single-Layer MoS_2 ... 86
5.4 Conclusion ... 86
5.5 References ... 92
6 Conclusion ... 93
6.1 Concluding Remarks ... 93
6.2 Future Directions ... 94

List of Tables

Table 1.1 | $LiNbO_3$ Properties 20

Table 3.1 | FET mobility (μ_{FE}) and threshold voltage (V_{th}) determined by different techniques 56

List of Figures

Figure 1.1 | 2D materials covering a broad spectra range: A) Electromagnetic spectrum and different applications in the top portion. Atomic structures of hBN, MoS_2, BP, & graphene B-E) Band structure of B) hBN, C) MoS_2, D) BP, and E) graphene [1.65] 18

Figure 1.2 | Propagation of a Rayleigh wave on a semi-infinite elastic solid: The energy and field displacements are concentrated within roughly a wavelength from the surface down into the substrate. At the surface, the particles move in an elliptical motion contained in the sagittal plane. The right panel depicts the side view in the sagittal plane [1.44] 19

Figure 1.3 | IDT schematic: The schematic of an input and output transducer used in the generation of SAWS where λ is the SAW wavelength, p is the IDT period, and W is the aperture width. On the right panel, the SAW and electric field are schematically sketched. 19

Figure 2.1 | Raman: Energy-level diagram showing the energy change in Raman (inelastic) and Rayleigh (elastic) scattering, where E_0 is the ground state, hv_m is the energy difference after scattering, and hv_0 is the energy of the incident beam 34

Figure 2.2 | Mechanism of PL in the local space and k-space: A laser pulse (green) with an E > Eg lifts an electron (orange) from the fully occupied VB into the empty CB leaving behind a hole (blue). The charge carriers relax into the band minimum (electrons) or maximum (holes) and in doing so release their excess energy. Subsequently, the electron and hole recombine to emit a photon (red), which is detected as PL signal. On the right panel Horiba LabRAM HR instrument used to measure Raman and PL characteristics 34

Figure 2.3 | Lithographic Patterning. A) Material of interest is identified B) Bi-layer resist is spun onto a substrate to a desired thickness C) The resist is then exposed using an electron beam to change its chemical composition D) The bi-layer resists is developed E) Metals are then deposited F) and the excess is removed by stripping the bi-layer resist, leaving the desired metallized pattern 35

Figure 2.4 | CVD furnace schematic: A typical growth setup is depicted. Transition metal powder is placed inside an alumina crucible, whereas a chalcogen precursor is placed in opposing crucible. 35

Figure 2.5 | RF Characterization: Left) Stanford Research System signal generator is used to source a RF signal to the input IDT Middle) Homemade carrier includes RF and BNC connections for electrical measurements Right) Chip carrier used, where wires bond the metallic pads from the substrate to metallic leads on the gold chip carrier. 36

Figure 2.6 | Vector network analyzer and light wave analogy: Left) A two-port VNA is used to analyze the DUT, where the transmission depicted at frequency of 159 MHz Right) Imagine traveling waves along a transmission line in terms of a light wave. Reflection in RF energy occurs when impedance is not the same, just like mirror in a light analogy. A lens will allow for some light to transmit, just much we would see in the transmission parameter S_{21} [2.02] 36

Figure 2.7 | Transport Setup: SMU used for the electrical characterization of the hybrid device. Keithley 2400 for constant current source and measurement of the voltage drop. Keithley 2600 was used to apply bias voltages and measure leakage current in the system. The right panel identifies the metallic leads used to connect the chip carrier to the BNC cables connected to its according SMU 36

Figure 2.8 | Optical setup for testing the attenuation with a laser source. The chip carrier and its metallic leads are inserted inside open slots inside a helium cryostat 37

Figure 3.1 | Raman spectrum of single-layer MoS_2: The vibration modes E^1_{2g} at 385 cm^{-1} and A_{1g} at 403 cm^{-1} and give rise to a frequency difference of 18 cm^{-1}. The right panel is an optical image of single-layer MoS_2 on a silicon substrate with a thermal oxide of 300 nm 51

Figure 3.2 | Raman spectrum prior to the growth of single-layer MoS_2 on $LiNbO_3$ (left) and post growth (right). The vibration modes in $LiNbO_3$ saturate the vibration modes from MoS_2, but a small hump gives indication that single-layer MoS_2 is present at 403 cm^{-1} 51

Figure 3.3 | PL spectrum comparison of single-layer MoS_2: The following is the PL spectrum of single-layer MoS_2 on $LiNbO_3$ (black) and on a 300 nm thermally grown oxide silicon substrate (red). 52

Figure 3.4 | Spatial PL map of MoS_2: The spatial PL map is used as a reference to locate the area of highest emission of single-layer MoS_2 52

Figure 3.5 | Hybrid SAW-FET device concept: Four Ti/Au contacts form the contacts of a FET fabricated on CVD-grown TMDs. The opposing two, non-impedance matched IDTs are used to excite SAWs propagating across the TMD FET 53

Figure 3.6 | Spatial PL map post fabrication of MoS_2-based hybrid device 53

Figure 3.7 | Electrical wiring configuration: Two-point (left) and four-point (right) configuration 54

Figure 3.8 | Single-layer MoS_2 output characteristics: I_{SD} versus V_{SD} for different V_G recorded in a two-point (left) and four-point (right) configuration. For large negative V_G, the device is weakly conducting: an n-type channel is formed for positive V_G 54

Figure 3.9 | Single-layer MoS_2 transfer characteristics: Left) I_{SD} versus V_G for different V_{SD} recorded in two-point configuration shows pronounced I_{SD} at positive V_G due to formation of an n-type channel. Right) Uncorrected FET transfer characteristics for different V_{SD} (colored) and gate leakage (black). The gate leakage current is weighted by a factor of 2.4 and subtracted from all characteristics. This procedure yields vanishing I_{SD} (V_G) ~ 0 for V_{SD} = 0. 55

Figure 3.10 | Example of V_{th} analysis: From the transfer characteristics, we are able to extract two values for the up and down direction for field-effect mobility (μ_{FE}) and threshold voltage (V_{th}) due to the hysteric nature of the device. 55

Figure 3.11 | Up and down sweep due to hysteric nature: Left) Threshold voltage (V_{th}) obtained from the up (red triangle) and down (blue triangle) sweep of the transfer characteristics as a function of V_{SD}. Right) Field-effect mobility (μ_{FE}) obtained from the slope of the output characteristics for up (red triangle) and down sweep (blue triangle), respectively. 56

Figure 3.12 | Single-layer MoS_2 conductance linear extraction: Comparison of channel conductance derived for two-point (left) and four-point (right) data. The μ_{FE} for two-point and four-point measurements are 33 cm^2 / V s and 43 cm^2 / V s, respectively. The V_{th} voltage of 5.5 V (two-point) exceeds the derived two-point measurement of 15.7 V by a factor of 5 because of the three-fold increase total channel length. 56

Figure 3.13 | Scattering parameters of single-layer MoS_2 hybrid device: Left) Transmission parameter (S_{21}) is measured as a function of frequency. Right) Reflection parameter (S_{11}) is functioning and no visible damage is apparent with the signal 57

Figure 3.14 | Acoustoelectric current as a function of RF signal applied to the IDTs for different RF power levels: Current measurements were performed in a two-point short-circuit (V_{SD} = 0) configuration. The forward direction (left) yields positive sign and reverse direction (right) yields negative sign 57

Figure 3.15 | Acoustoelectric voltage as a function of P_{RF} (mW): Measurements were done in a two-point, open circuit configuration (I_{SD} = 0). For the forward (left) and reverse (right) SAW propagation direction, the expected linear dependence is well reproduced 58

Figure 3.16 | Acoustoelectric current as a function of RF power (dBm): The negative acoustoelectric current forms in the forward propagating direction. This type of behavior corresponds to n-type conductivity of the film and is expected for single-layer MoS_2 58

Figure 4.1 | Raman spectrum of single-layer WSe_2: The vibration modes E^1_{2g} at and A_{1g} merge as expected for single-layer WSe_2 at 249 cm^{-1}. The right panel is an optical image of single-layer WSe_2 islands on a silicon substrate with a thermal oxide of 300 nm along with a gold crosshairs. 72

Figure 4.2 | Raman spectrum of prior (left) and post (right) growth of single-layer WSe_2 on $LiNbO_3$. The vibration modes in $LiNbO_3$ saturate the vibration modes of WSe_2 72

Figure 4.3 | PL characterization of single-layer WSe_2: Comparison of single point normalized PL spectra obtained on SiO_2 (blue) and our 128°YX-cut $LiNbO_3$ substrate (black) reveals a blue shift attributed to the compression of the single-layer WSe_2 film. Similar results were seen on the MoS_2 hybrid device 73

Figure 4.4 | Post growth and spatial PL map of single-layer WSe_2 on $LiNbO_3$: Optical image of CVD-grown single-layer WSe_2 on a $LiNbO_3$ substrate. The rectangle marks the scan region for the spatial PL map of WSe_2. On the right is the PL spatial map. The intensity is color coded with red (dark) correspond to high (low) count rates confirms mm-scale growth. Electrical contacts are placed in the area of highest emission 73

Figure 4.5 | Layout of IDTs: The micrograph shows the double finger (split-2) IDTs used in this study. They have 21 fingers pairs, an aperture of 200 µm, a delay line width of 180 µm and were fabricated 5.4 mm apart. Post single-layer WSe_2 etch: Optical micrograph of our hybrid device covered with resist. The exposed regions are etched with oxygen plasma. 74

Figure 4.6 | Post fabrication spatial map: High emission is still present after etching to ensure no shortcuts affect transport measurements. Dark areas indicate no material is present while the highest emission is color coded in red 74

Figure 4.7 | Single-layer WSe_2 output and transfer characteristics: Output curve measured I_{SD} versus V_{SD} for different V_G recorded in a two-point configuration. For large positive V_G, the device is

weakly conducting: a p-type channel is formed for negative V_G. Transfer curve on the right panel ... 75

Figure 4.8 | Threshold voltages: Threshold voltages (V_{th}) obtained from the up (up red triangle) and down sweep (down blue triangle) of the transfer characteristics as a function of V_{SD} It is to be noted that V_{th} is simply the V_G at which the FET becomes conductive ... 75

Figure 4.9 | Mobility and conductance of single-layer WSe_2: Field-effect mobility obtained from the slope of the transfer characteristics for up (up red triangle) and down sweep (down blue triangle), respectively. Conductance on the right panel exhibited field-effect mobility (μ_{FE}) of 14.5 cm^2 / V s with a threshold voltage (V_{th}) of – 5.5 V. ... 76

Figure 4.10 | SAW transmission and reflection parameter: Transmission parameter (S_{21}) between the IDTs shows a pronounced maximum at the design frequency f_{SAW} = 160 MHz of the 5.4 mm long delay line. Reflection parameter (S_{11}) is on the right ... 77

Figure 4.11 | Acoustoelectric frequency dependence: Current measurements were performed in a two-point short-circuit (V_{SD} = 0) configuration. The forward direction (left) yields positive sign and reverse direction (right) yields negative sign. Frequency dependence of the band of the SAW transmission is replicated when applying higher RF power levels. ... 77

Figure 4.12 | Acoustoelectric voltage as a function of RF power (mW): Acoustoelectric voltage measured in a four-point, open-circuit configuration (I_{SD} = 0). Forward propagation (left) gives a negative value and a reverse propagation (right) gives a positive value, which is opposite the result seen for single-layer MoS_2. ... 78

Figure 4.13 | Acoustoelectric current as a function of RF power (dBm): Positive acoustoelectric current forms for the forward propagating direction. The reverse effect occurs when switching the propagation direction, therefore attaining a negative acoustoelectric current. The signs of the acoustoelectric current and voltages correspond to p-type conductivity of the single-layer WSe_2 film. ... 78

Figure 5.1 | Schematic representation of the hybrid MoS_2/$LiNbO_3$ device: Four Ti/Au electrodes form the contacts of a FET fabricated on CVD-grown single-layer MoS_2. Two opposing, non-impedance matched IDTs are used to excite SAWs across the propagation path. The sample was excited optically using 50x objective microscope with a numerical aperture (NA) of 0.55 ... 88

Figure 5.2 | Transmission parameter: Frequency band of the SAW transmission between IDTs plotted as the scattering parameter S_{21} 88

Figure 5.3 | Comparison of the time-dependent photoresponse detected by the change of the transmitted SAW intensity (ΔS_{21}): Red (left) and black (right) traces were recorded for laser power of 1 mW excitation by a red and infrared laser, respectively. These lasers are switched on for five seconds. No photoresponse detected by the infrared laser while the red laser has a profound photoresponse. 89

Figure 5.4 | Comparison of the time-dependent photoresponse detected by the change of the two-point conductance (ΔG) of the FET: Red (left) and black (right) traces were recorded for laser power of 1 mW excitation by a red and infrared laser, respectively. These lasers are switched on for Δt = 5 s at t = 6 s. Both the instantaneous and persistent features of the photoresponse are consistently resolved by both the SAW transmission and conductance. For excitation with an infrared laser, no photoresponse is detected, proving that the signal detected for the red laser indeed stems from the single-layer MoS_2 89

Figure 5.5 | Laser power: The laser is switched on every 1 minute for Δt = 5 s. Each successive minute P_{laser} is increased 0.1 mW until P_{laser} = 1 mW is reached. Subsequently, P_{laser} is decreased to 0 mW in steps of ΔP_{laser} = 0.1 mW. 90

Figure 5.6 | Comparison of SAW transmission (ΔS_{21}) and photocurrent (I_{SD}) at V_{SD} = + 100 mV 91

Figure 5.7 | Comparison of SAW transmission (ΔS_{21}) and photocurrent (I_{SD}) at V_{SD} = – 100 mV 91

List of Equations

Equation 1.1 9

Equation 1.2 9

Equation 1.3 9

Equation 1.4 10

Equation 1.5 11

Equation 1.6 12

Equation 1.7 13

Equation 1.8 13

Equation 1.9 13

Equation 1.10 14

Equation 1.11 14

Equation 1.12 14

Equation 1.13 14

Equation 1.14 15

Equation 2.1 27

Equation 2.2 31

Equation 2.3 31

Equation 3.1 45

Equation 3.2 46

Equation 4.1 68

Equation 4.2 69

Equation 5.1 81

Equation 5.2 82

Equation 5.3 84

Equation 5.4 84

Equation 5.5 84

List of Publications

[01] Michailow, W., et al. (2017). "Combined electrical transport and capacitance spectroscopy of a MoS2-LiNbO3 field effect transistor." Applied Physics Letters **110**(2): 023505.

[02] Empante, T. A., et al. (2017). "Chemical Vapor Deposition Growth of Few-Layer MoTe2 in the 2H, 1T', and 1T Phases: Tunable Properties of MoTe2 Films." ACS Nano.

[03] Tanabe, I., et al. (2016). "Band structure characterization of WS2 grown by chemical vapor deposition." Applied Physics Letters **108**(25): 252103.

[04] Sun, D., et al. (2015). "Chemical vapor deposition growth of a periodic array of single-layer MoS2islands via lithographic patterning of an SiO2/Si substrate." 2D Materials **2**(4): 045014.

[05] Preciado, E., et al. (2015). "Scalable fabrication of a hybrid field-effect and acousto-electric device by direct growth of monolayer MoS2/LiNbO3." Nat Commun **6**: 8593.

[06] Nguyen, A., et al. (2015). "Toward Ferroelectric Control of Monolayer MoS2." Nano Lett **15**(5): 3364-3369.

[07] Le, D., et al. (2015). "Spin-orbit coupling in the band structure of monolayer WSe2." J Phys Condens Matter **27**(18): 182201.

[08] Klee, V., et al. (2015). "Superlinear composition-dependent photocurrent in CVD-grown monolayer MoS2(1-x)Se2x alloy devices." Nano Lett **15**(4): 2612-2619.

[09] Plechinger, G., et al. (2014). "A direct comparison of CVD-grown and exfoliated MoS2using optical spectroscopy." Semiconductor Science and Technology **29**(6): 064008.

[10] Ma, Q., et al. (2014). "Postgrowth tuning of the bandgap of single-layer molybdenum disulfide films by sulfur/selenium exchange." ACS Nano **8**(5): 4672-4677.

[11] Mann, J., et al. (2014). "2-dimensional transition metal dichalcogenides with tunable direct band gaps: MoS(2)((1)-x) Se(2)x monolayers." Adv Mater **26**(9): 1399-1404.

[12] Mann, J., et al. (2013). "Facile growth of monolayer MoS2 film areas on SiO2." The European Physical Journal B **86**(5).

1 Introduction

1.1 Introduction

This thesis describes work that aims to understand the acoustoelectric and electric properties of two-dimensional (2D) transition metal dichalcogenides (TMD), particularly single-layer molybdenum disulfide (MoS_2) and tungsten diselenide (WSe_2). This is investigated by applying surface acoustic waves (SAWs) in a hybrid device configuration that combine field-effect transistor (FET) functionality with response to SAWs and the cross-validation of the respective signals. The hybrid device configuration is used to propel charge carriers through the material to measure the interaction of propagating waves on TMDs, enabling an examination of the influence of electrical contacts used for the detection of the acoustoelectric charge. Additionally, electrical transport with conventional contacts is also examined on a traditional FET setup to determine the charge carrier mobility. Furthermore, optical excitation is used to demonstrate the versatility that SAWs provide for probing poorly-conductive films that are sensitive to optical wavelengths through the acoustoelectric effect. For example, when exposed to a certain wavelength, the semiconducting TMD generates charge carriers, which interact with the electric fields produced in the piezoelectric substrate by the traveling SAW. This research demonstrates the versatility and power of this approach by measuring of the photoconductivity of a single-layer MoS_2 film. Experimental data and analysis addressing these effects will be presented throughout the thesis.

1.2 Two-Dimensional Materials

Nearly 60 years ago, Richard Feynman proposed the concept of miniaturization by envisioning how “one could arrange structures with just the right layers” to uncover unique properties at their physical limit [1.01]. This vision encouraged scientists and engineers to separate materials into individual layers, which exhibit enhanced properties that differ from their bulk counterparts. For example, in 2004, Novoselov isolated a single atomic layer of graphene from its bulk counterpart, graphite [1.02]. This process was recently honored with the Nobel Prize in Physics and has become the foundation of atomically-thin layers of van der Waals materials [1.03]. Graphene has since been recognized as a promising candidate for future electronic applications because of its high carrier mobility [1.04] and high thermal conductivity [1.05]. However, there are also aspects that impose limitations for graphene, such as its lack of a bandgap [1.06]. As a result, many researchers have sought to uncover alternative materials with a direct bandgap. This has triggered an explosive interest in creating a new field of research based on 2D materials. Figure 1.1 lists a growing field of 2D materials that are currently under investigation. Among these materials are various kinds of TMDs, which harness diverse properties that are favorable for various energy-related applications [1.65]. The following subsection introduces a brief description of the material properties found in TMDs.

1.3 Transition Metal Dichalcogenides

Two-dimensional TMDs are part of an emerging class of materials that exhibit exceptional electrical and optical properties and are becoming one of the most studied areas of solid-state physics and technology. These unusual properties arise in their unique hexagonal structure, compromising individual layers (X-M-X) composed of a transition metal plane (M = Mo, W) that is covalently bonded between two chalcogen (X = Se, Se) planes. In terms of molecular geometry, 2D TMDs mainly exist in trigonal prismatic (2H semiconducting phase) or octahedral (1T metallic phase) structure; these terms refer to the coordination of the transition

metal atom. In contrast with graphene, TMDs do have a native bandgap, and have attracted considerable attention when produced in their single-layer limit. Particularly, the bandgap in a semiconducting TMD transforms from an indirect bandgap at its bulk state to a direct bandgap in its single-layer state [1.07]. This transition occurs in the electronic band structure and has been computed by using density functional theory [1.08-12]. Literature has stated the indirect bandgap occurs in the gamma point for bulk and the direct bandgap in the K point. Therefore, selecting the material and layering it appropriately can tune these 2D materials to precise wavelengths. By offering a tunable bandgap of 1.1 – 1.9 eV ($MoTe_2$ to WS_2), these 2D semiconductors can complement the properties of graphene through their strong photoluminescence (PL) [1.07], significant spin-orbit coupling [1.13], and carrier mobility competitive to silicon [1.14]. The rest of this thesis mainly focuses on molybdenum disulfide (MoS_2) and tungsten diselenide (WSe_2).

1.3.1 Molybdenum Disulfide

The following section provides an extensive literature review on MoS_2 and all of its unique properties. Currently, MoS_2 is one of the more stable TMDs and will be extensively examined throughout this thesis.

In terms of crystal structure, MoS_2 is hexagonal (2H) and has a layered structure with D_{6h} point group symmetry [1.15]. It occurs naturally as a bulk crystal, and is constructed from layers consisting of an atomic plane of molybdenum sandwiched between two atomic planes of sulfur in a trigonal prismatic arrangement. These layers are linked through weak van der Waals forces, with strong covalent bonds between the molybdenum and sulfur atoms [1.14]. Each individual layer has D_{3h} point group symmetry and an approximate thickness of 6.5 Å, with a distance between each sulfur atom of roughly 3.2 Å [1.16]. The lattice constants of a single layer are reported to be ≈ 3.22 Å, with a covalent bond length of Mo-S of 2.43 Å and an S–Mo–S bond angle of ≈ 80.56° [1.15,1.17].

An electronic band structure describes the range of energies that an electron may have within a solid material. The primary focus of this research is the unique band structure of MoS_2 in its semiconducting 2H

phase. Since MoS_2 is a semiconductor, the conductivity will likely vary by temperature, light, and electric field. A semiconductor has a bandgap between the lowest point of the conduction band and the highest point of the valence band, which can be categorized as direct or indirect. In order to achieve a direct bandgap, a semiconductor must have the edges of the conduction and valence band aligned in the K direction. This permits an electron to travel from the valence band to conduction band, resulting in the emission of a photon. However, an indirect bandgap is not aligned and requires momentum for the electron to reach the conduction band. Similarly, bulk MoS_2 has the valence band maximum centered at the Γ point and the conduction band minimum located midway in the Γ– K direction, resulting in an indirect bandgap of 1.2 eV [1.18]. The unique electronic property of MoS_2 is the crossover from a bulk indirect bandgap material to establish a direct K–K band transition with a gap of 1.9 eV in its single-layer limit. As the number of MoS_2 layers decrease, the conduction band states between Γ and K and the valence band states at the Γ point spread out; meanwhile, the bands at K Brillouin point remain the same [1.19-20]. This dramatic change of the electronic structure could explain why single-layer MoS_2 exhibits such a high PL [1.08]. Single-layer MoS_2 exhibits two excitonic peaks, which are denoted as A (1.9 eV) and B (2.05 eV) around the K zone [1.07].

Raman spectroscopy is a technique used to determine the vibrational modes of van der Waals materials, such as MoS_2 [1.21]. It provides useful information based on the vibration modes present in the hexagonal Brillouin zone of the 2H phase of MoS_2 [1.22-23]. Amongst them, the two modes on which this research focuses are the in-plane mode of two sulfur atoms with respect to the molybdenum atom (E^1_{2g} band) and the out-of-plane mode of sulfur atoms in the opposite direction (A_{1g} band). Single-layer MoS_2 exhibits some differences from its bulk counterpart in terms of the frequency shift difference between the E^1_{2g} and the A_{1g} peaks. For example, in a Raman spectrum of single-layer MoS_2, the E^1_{2g} is at 385 cm^{-1} and the A_{1g} at 403 cm^{-1}. A typical frequency shift difference of 18 cm^{-1} indicates single-layer MoS_2. As the number of layers increase, the E^1_{2g} band red shifts (softens) and the A_{1g} band blue shifts (stiffens) consistently until reaching a

frequency difference of ≈ 25 cm^{-1} for bulk MoS_2. As a result, the utilization of Raman can estimate the number of layers present in MoS_2 [1.24].

Field-effect transistors are the fundamental building block of the electronics industry, and their dimensions have shrunk exponentially over the past years to produce faster device architectures. Unlike conventional silicon FETs, 2D FETs offer an opportunity to add thinner channel materials that are free from short-channel effects. As a result, the incorporation of 2D materials, such as MoS_2, provides miniaturization beyond the physical limits of the current silicon-based technology [1.11]. In 2005, Novoselov et al. reported on the first MoS_2-based FET and presented a mobility of 3 cm^2 / V s [1.03]. A top-gate, high-K dielectric, such as HfO_2, was used to improve the carrier mobility of single-layer MoS_2 up to 200 cm^2 / V s. This ultimately demonstrated the first switchable transistor with a drain current on/off ratio of 10^8 utilizing exfoliated single-layer MoS_2 by Radisavljevic et al. [1.14]. The highest reported mobility was achieved by Kis of 1090 cm^2/ V s at a drain voltage of 20 mV [1.25].

MoS_2 has a direct bandgap in the visible range and allows for detection of the photoelectric effect. The irradiation of photons provided by a laser source with a wavelength greater than the bandgap of a semiconductor produces a photocurrent upon the separation of photogenerated excitons through an applied field (phototransistor) or built-in field (photodiode). For example, Yin et al. fabricated the first exfoliated single-layer MoS_2 phototransistor [1.26]. This exhibited an increased photocurrent for excitation wavelengths below 670 nm, with a 7.5 mA/W photoresponsivity and a 50 ms current rise or decay. Later, Lopez-Sanchez et al. demonstrated an exfoliated, single-layer MoS_2 photodetector with a maximum photoresponsivity of 880 A/W at an excitation of 561 nm and with a low-intensity optical power of 150 pW [1.27]. This enhancement is the result of a higher mobility and improved electrode quality. Recently, Zhang et al. demonstrated a photodetector based on a chemical vapor deposition (CVD)-grown MoS_2/graphene heterostructure that was able to provide a photogain of 10^8 with a 10^7 A/W when exposed to a 650 nm wavelength at V_G = – 10 V and V_{SD} = 1 V [1.28]. The light-generated carriers from MoS_2 were injected into

graphene as a result of a perpendicular effective electric field at the 2D interface. Rathi et al. highlighted a representation of this graphene-MoS_2 phototransistor behavior [1.29].

1.3.2 Tungsten Diselenide

WSe_2 features unique properties that are well suited for a range of optoelectronic applications in the near infrared regime. The following section provides and discusses an extensive literature review on the properties of WSe_2.

In terms of crystal structure, WSe_2 displays a hexagonal (2H)-layered structure with D_{6h} point group symmetry [1.30]. The tungsten atoms form a trigonal prismatic geometry and favor a six-fold coordinated structure [1.30]. Strong covenant bonds hold together the tungsten and selenium atoms. Each layer has a thickness of approximately ~ 7 Å and is vertically connected via van der Waals forces [1.31]. Literature has reported values for the lattice constants of WSe_2 to be ≈ 3.27 Å with a covalent bond length W-Se of 2.55 Å and Se–W–Se bond angle of ≈ 82.43° [1.31]. The interlayer distance is greater for WSe_2 compared to MoS_2 due to the large size of the Se atom.

Similarly to MoS_2, the evolution of the band structure of WSe_2 from indirect to direct is associated with the change of the valence band maximum from Γ to K in single layer, as computed by theory and experimental groups [1.13,1.32]. Bulk WSe_2 has the valence band maximum centered at the Γ point, and the conduction band minimum is located midway in the Γ– K direction. This results in an indirect band gap of 1.20 eV [1.12]. A crossover from a bulk indirect bandgap to a K-K band transition with a gap of 1.63 eV at the single-layer limit establishes a direct bandgap, although some research has reported an indirect to direct transition for bi-layer WSe_2 [1.32]. The dramatic change of the electronic structure explains the high PL emission of single-layer WSe_2. The excitonic peaks for WSe_2 are A (1.63 eV) and B (2.07 eV) [1.33].

WSe_2 has two Raman-active vibration modes, which include the in-plane E^1_{2g} mode and out-of-plane A_{1g} mode. The two dominant peaks appear around 250 cm^{-1}, but minimal systematic trend could be observed for both modes [1.34]. At the single-layer limit of WSe_2, the E^1_{2g} and A_{1g} peak merge at around 249 cm^{-1} and progressively separate at the bulk limit.

WSe_2 has attracted significant attention for electronic applications due to its p-type capability. For example, a recent study of bulk WSe_2 FETs reported hole-mobility approaching 500 cm^2 / V s [1.35]. Shortly after, single-layer WSe_2 FETs with a body thickness of 0.7 nm were first demonstrated with heavily p-doped contacts, which enabled the demonstration of p-FETs with a hole-mobility of 250 cm^2 / V s [1.36]. Other few-layered WSe_2 FETs have also been demonstrated with high on/off ratios and ambipolar mobilities [1.37]. A possible reason for the difference in mobility values is visible in theoretical and experimental calculations that reveal that defects and grain boundaries all assist in significantly decreasing the conductivity of CVD-grown TMDs when compared to single-crystalline exfoliated WSe_2 [1.38]. Although candidates such as $MoTe_2$ offer p-type capabilities, they lack stability in ambient conditions. Therefore, the well-developed science of WSe_2 distinguishes it as a viable candidate for a channel material for 2D p-FETs [1.36].

1.4 Surface Acoustic Waves

A surface wave is like a nano-earthquake that combines longitudinal and transverse motion to propagate along the surface of a material. This in-plane elliptical motion is called a Rayleigh wave and was first demonstrated by Lord Rayleigh in 1885 [1.39]. Figure 1.2 depicts the energy and field displacements, which are roughly concentrated within a wavelength from the surface down into the substrate. In general, the mechanical amplitude is relatively small in the order of one nanometer, in which the elastic deformation produces electric fields. The coupling between the elastic and electromagnetic contributions is minor because the SAW sound velocity (3,980 m/s) is much lower than the electromechanical velocity of light ($3.0x10^8$) in a medium. As a result, SAWs can function as delay lines in a circuit to separate direct

electromagnetic crosstalk from acoustic crosstalk. This yields the development of interdigital transducers (IDT) that could generate radio frequency (RF) waves along the surface of a solid. A brief introduction in this section provides a basic understanding of the generation, propagation, and detection of SAWs.

1.4.1 Piezoelectricity

Piezoelectricity is an important topic to discuss when describing how SAW devices work. This unique property was discovered experimentally in 1880, when French physicists Jacques and Pierre Currie applied stress to a number of crystals, such as quartz and tourmaline. They observed that applying either compressive or tensile stress to a crystal generated voltages of opposite polarities [1.41]. Hankel later termed this the piezoelectric effect, a name which derives from Greek and means "electricity resulting from pressure". Shortly afterwards, Lippman [1.42] predicted that electrical fields can deform piezoelectric materials, which the Curries later confirmed [1.43]. This inverse effect revealed that a piezoelectric material exposed to an electric field would stretch or compress to the polarity of the field.

The direct piezoelectric effect works through the following steps. Initially, two equal and opposite forces are applied to a piezoelectric crystal. This generates a tensile stress that creates a deformation in the crystal lattice and produces a separation of positive and negative charges. This separation yields electrical dipoles, and the crystal electrically polarizes to form a new electrical charge on the surface of the electrodes. The removal of the forces releases the strain within the crystal lattice, enabling the current to flow. Therefore, electrical energy is produced from mechanical energy [1.44]. In contrast, when an external voltage is applied to the electrodes, the crystal lattice deforms by an amount proportional to the applied voltage. In this case, electrical energy is transformed into mechanical potential energy [1.44].

1.4.2 The Piezoelectric Effect

Within a solid medium, the components of the stress field T_{ij} describe the mechanical forces, while the components of the strain field S_{ij} describe the mechanical deformations. In piezoelectric materials, coupling between the electrical and mechanical parameter gives rise to mechanical strain upon the application of an electrical field, and vice versa. The mechanical stress relationship is thus extended to (Hookes Law is $T_{ij} = c_{ijkl}S_{kl}$):

$$T_{ij} = c_{ijkl}^{E} S_{kl} - e_{kij} E_K \qquad \text{Equation 1.1}$$

Here, T_{ij} represents the mechanical stress second-rank tensor components (N/m^2) and S_{kl} is the strain second-rank tensor components (dimensionless). c_{ijkl} is the elastic stiffness constant (N/m^2) represented by a fourth-rank tensor that is either measured under zero or a constant electric field. e_{kij} is the piezoelectric constant (C/m^2), and E_k is the kth component of the electrical field.

The elastic stiffness (c) can be reduced to a 6 x 6 matrix. Depending on the crystal symmetry, these 36 constants can be reduced to a maximum of 21 independent constants. For example, lithium niobate contains a trigonal symmetry, and its independent constants are reduced to just six [1.40].

$$\begin{pmatrix} c_{11} & c_{12} & c_{12} & c_{14} & 0 & 0 \\ c_{12} & c_{11} & c_{13} & -c_{14} & 0 & 0 \\ c_{12} & c_{13} & c_{33} & 0 & 0 & 0 \\ c_{14} & -c_{14} & 0 & c_{44} & 0 & 0 \\ 0 & 0 & 0 & 0 & c_{44} & c_{14} \\ 0 & 0 & 0 & 0 & c_{14} & \frac{1}{2}(c_{11} - c_{12}) \end{pmatrix} \qquad \text{Equation 1.2}$$

For piezoelectric materials, the electrical displacement is related to the electric field applied by:

$$D_i = e_{ikl} S_{kl} + \varepsilon_{ik}^{S} E_K \qquad \text{Equation 1.3}$$

Here, e_{kij} is the piezoelectric constant. S_{kl} is the strain second-rank tensor components, and e_E is the permittivity measured at constant or zero strain. E_k is the kth component of the electric field. These equations are often referred to as piezoelectric constitutive equations.

1.4.3 Piezoelectric Materials

The consideration of important material properties is key when selecting a piezoelectric substrate. In particular, research has indicated that the use of different piezoelectric material would influence how a SAW device works. It is necessary to examine many factors prior to substrate selection, including the SAW velocity, coupling coefficient, functional frequency range, high quality factor, and low attenuation. For example, the elasticity is coupled with the electric fields that help the transduction procss by converting the electric field into acoustic waves, and vice versa. As a result, when metal electrodes short the surface of a piezoelectric material, the velocity changes from v_f (free surface velocity) to v_m (metallized surface velocity) [1.44]. Subsequently, this change in velocity can be used to determine the extent of the electromechanical coupling efficiency constant:

$$K^2 = 2\left(\frac{v_f - v_m}{v_f}\right) \quad \text{Equation 1.4}$$

Therefore, the change in the velocity is a method for measuring the electromechanical coupling efficiency of the material. As a result, a strong piezoelectric material with a high coupling constant is considered to establish a significant effect.

1.4.4 Interdigital Transducer

In 1965, White and Voltmer integrated surface waves in the field of electronics by introducing the IDT to generate SAWs of various shapes on a piezoelectric substrate [1.45]. Interdigital transducers consist of an

input electrode, a delay path, and an output electrode. To understand the response, consider two identical electrode transducers (input and output) with a pitch length p and transducer width W. Applying a voltage to the RF source triggers a transduction from electrical into mechanical energy at the input electrode due to the inverse piezoelectric effect. The alternating electric field induces a mechanical displacement on the piezoelectric substrate and results in a SAW in both directions that is perpendicular to the IDT propagating along the surface of the delay path. The transmitted mechanical displacement is converted back into an electric field through the direct piezoelectric effect. The frequency of a SAW device depends on the material properties of the piezoelectric substrate and the geometry of the IDT, given by the following equation:

$$v = \lambda f \qquad \text{Equation 1.5}$$

Here, v is the sound velocity in the piezoelectric substrate, λ is the SAW wavelength or pitch of the IDT, and f is the frequency of the propagating SAW. A schematic displays an IDT in Figure 1.3. The invention of IDTs allowed for the development of multiple SAW devices and laid the foundation for key components, such as filters and single processors in mobile communication. This then paved the way for the invention and implementation of SAW identification tags and sensor devices [1.46].

1.4.5 Substrate Selection

Surface acoustic wave devices have been used in the field of electronics for many years, notably in quartz resonators. Research has revealed that the use of different piezoelectric substrates would influence the sound velocity of the wave. Subsequently, there was a substantial effort to replace quartz and find a new material that would not lack processing techniques [1.45]. As a result, single-crystalline substrates brought forth a range of materials, such as $LiNbO_3$, that offer a series of propagating velocities in the range of 3,000 to 6,000 m/s [1.47]. The material selection is not only based on the sound velocity; features such as high quality factor, low attenuation, and the lossyness of a material are some of the other requirements that

depend on the substrate material. For example, $LiNbO_3$ has a large piezoelectric coupling coefficient of 5.6%, making it a popular choice [1.44]. Through a combination of substantial piezoelectric and birefringent properties, $LiNbO_3$ offers pronounced electro-optic, acousto-optic, and acoustoelectric activities, which render it the material of choice for number applications in RF signal processing [1.48] and passive integrated optics [1.49]. $LiNbO_3$, the "silicon of photonics" [1.50], exhibits a large ~ 3.95 eV indirect bandgap [1.51]. Table 1.1 summarizes relevant properties for a $LiNbO_3$ substrate.

1.5 The Acoustoelectric Phenomena

The acoustoelectric phenomenon refers to the interaction of charge carriers in the presence of a SAW, which exhibits two types of effects. The first type of effect occurs when charge carriers are in the path of the SAW, and therefore change the amplitude and velocity of the wave. The second type of effect utilizes SAWs to trap the charge carriers in their potential minima and generate a DC electric current (short circuit) or voltage (open circuit) along the propagation path of an acoustic wave [1.52]. Parmenter observed this phenomenon in 1953, and it was later termed the acoustoelectric effect. He suggested a transfer of momentum to the charge carriers resulting from a periodic modulation in the conduction and valence band of a material due to the SAW. These carriers surf on the wave and generate a current in the SAW propagation direction. Shortly afterwards, Weinreich explained this effect in detail by investigating the motion of charge carriers in a semiconductor in the presence of a propagating wave [1.53]. In this effort, he measured the acoustoelectric effect in n-type germanium and defined the following relationship for the current density j [1.54]:

$$j = -\mu Q = -\mu\left(\frac{\Gamma F}{v}\right) \qquad \text{Equation 1.6}$$

Here, μ is the carrier mobility, Q is the phonon pressure, F is the SAW intensity flux, Γ is the attenuation per unit length, and v is the velocity of the wave.

1.5.1 Acoustoelectric Effect in Semiconductors

Following the discovery of the acoustoelectric phenomenon, Hutson and White explored the interaction of bulk semiconductors with uniform conductivity σ along the propagation of bulk waves [1.55]. In a classical relaxation model, they obtained the following equations for the velocity change Δv/v and attenuation Γ:

$$\Gamma = K^2 \frac{\pi}{\lambda} \left[\frac{\left(\frac{\omega_c}{\omega}\right)}{1 + \left(\frac{\omega_c}{\omega}\right)^2} \right] \qquad \text{Equation 1.7}$$

$$\frac{v - v_0}{v_0} = \frac{\Delta v}{v_0} = \frac{K^2}{2} \left[\frac{1}{1 + \left(\frac{\omega_c}{\omega}\right)^2} \right] \qquad \text{Equation 1.8}$$

$$\omega_c = \frac{\sigma}{\varepsilon} \qquad \text{Equation 1.9}$$

Here, ω_c is the conductivity relaxation frequency, ω is the piezoelectric relaxation frequency, σ is the conductivity, ε is the dielectric constant of the piezoelectric substrate, K^2 is the electromechanical coupling coefficient, and λ is the wavelength of the wave [1.56]. The acoustoelectric model served to explain the concept of charge carriers clustering in the wave troughs [1.57]. As a result, the dragging of charge carriers consumes the energy of the wave, which is detected in its attenuation Γ and change of velocity Δv. This form of spectroscopy has been performed on bulk semiconductors and their hetero-structures, even in the quantum regime [1.56].

1.5.2 Acoustoelectric Effect in Two-Dimensional Electron Gases

Surface acoustic waves in particular offer a versatile approach, since fully-electronic excitation and detection of these nano-scale sound waves is possible on a chip. For more than 15 years, the interaction of SAWs with a two-dimensional electron gases (2DEG) over a piezoelectric substrate have been realized in a

hybrid system [1.58]. In particular, SAWs on a piezoelectric substrate are accompanied by a potential wave and generate an electric field originating from the substrate's polarization under mechanical deformation. These electric fields interact with charge carriers in a 2DEG film in close vicinity to the surface, such that a separation is much smaller than the SAW wavelength. Ingebrigtsen revealed the importance of the thickness of the semiconductor film compared to the SAW wavelength on a piezoelectric insulator [1.59]. In turn, this relationship allows for the 2DEG conductivity σ_{2D} and characteristic conductivity σ_M to substitute the conductivity relaxation frequency ω_c and frequency of the piezoelectric ω as the following:

$$\omega_c = \frac{k_{SAW}\sigma_{2D}}{\varepsilon_0 + \varepsilon_r}$$ Equation 1.10

$$\omega = \frac{k_{SAW}\sigma_M}{\varepsilon_0 + \varepsilon_r}$$ Equation 1.11

Here, k_{SAW} is the SAW wave vector, ε_0 is permittivity of free space, and ε_r is the relative permittivity of the piezoelectric substrate. These hybrids have an interaction between SAWs and the charge carriers confined in the 2DEG, and the induced acoustoelectric current is assumed to be only in the 2DEG. The 2DEG influences the propagation of the SAW, therefore changing the wave velocity and producing an attenuation of the wave. Wixforth describes the piezoelectric interaction between the SAW and charge carriers in a 2D system using a simple classical relaxation model [1.56,1.60]:

$$\Gamma = K^2 \frac{\pi}{\lambda}\left[\frac{\left(\frac{\sigma_{2D}}{\sigma_M}\right)}{1+\left(\frac{\sigma_{2D}}{\sigma_M}\right)^2}\right]$$ Equation 1.12

$$\frac{v - v_0}{v_0} = \frac{\Delta v}{v_0} = \frac{K^2}{2}\left[\frac{1}{1+\left(\frac{\sigma_{2D}}{\sigma_M}\right)^2}\right]$$ Equation 1.13

Here, Γ is the attenuation per unit length, K^2 is the electromechanical coupling efficiency, λ is the SAW wavelength, σ is the sheet conductivity, σ_M is the characteristic conductivity, and v_0 is the SAW velocity when the surface is shorted. The characteristic conductivity is determined by the following equation:

$$\sigma_M = v_{SAW}\ \varepsilon_0(\varepsilon_r + 1) \qquad \text{Equation 1.14}$$

Here, ε_0 is permittivity of free space and ε_r is the relative permittivity of the piezoelectric substrate. This attenuation causes a loss of energy from the SAW, which leads to a proportional loss of momentum. This appears as a force on the carrier system and is the mechanism behind the acoustoelectric effect. As a result, the attenuation and velocity modulation of the acoustic signal can be used to determine the conductivity of the 2DEG. Recently, similar hybrids have been reported for graphene [1.61-64]. The commonality of these applications is that the semiconducting layer is loosely attached to the substrate via weak van der Waals interactions. This serves a critical role when growing a semiconducting layer on a piezoelectric substrate to create the hybrid device.

1.6 Motivation

In 2004, Novoselov et al. isolated a single-atomic layer of graphene from its bulk counterpart, graphite [1.02]. Graphene has since been a promising candidate for future electronic applications because of its unique properties, such as its high carrier mobility and high thermal conductivity. One drawback includes its lack of a native bandgap. This finding triggered an explosive interest in an entirely new field of research of 2D materials. Transition metal dichalcogenides are a different class of 2D materials that have attracted considerable attention for optoelectronic applications because of their direct bandgap semiconducting property at the single-layer limit [1.07,1.08]. Offering a tunable bandgap of 1.1–1.9 eV ($MoTe_2$ to WS_2), these 2D semiconductors can complement the properties of graphene through their strong PL, significant spin–orbit coupling [1.13], and mobility and carrier concentrations completive to silicon [1.14]. Acoustoelectric

spectroscopy has a long-standing tradition of probing and controlling solid-state materials [1.52, 1.53]. Surface acoustic waves in particular offer a versatile approach, since these nanoscale sound waves can be excited and detected all-electrically on a chip. Surface acoustic wave spectroscopy has been performed on bulk semiconductors and their hetero-structures, even in the quantum regime [1.56]. For more than 15 years, semiconductor-$LiNbO_3$ hybrids have been realized by epitaxial lift-off and transfer onto the $LiNbO_3$ substrate [1.58]. Recently, similar hybrids have been reported for graphene [1.61-64]. The commonality of these applications is that the semiconducting layer is loosely attached to the substrate via weak van der Waals interactions. Astonishingly, acoustoelectric measurements have hardly been performed on TMDs. It is logical to examine the acoustoelectric properties in greater detail, as there are a number of useful construction elements on the basis of SAWs. This work examines both the electrical and acoustoelectric properties of TMDs, specifically MoS_2 and WSe_2.

The main objective of this thesis is to design, fabricate, and test a hybrid acousto-electric device. The goal is to see the interaction of propagating waves on single-layer semiconducting TMD films, such as single-layer MoS_2 and WSe_2. For this purpose, SAWs are created with this hybrid device and a single-layer TMD layer is placed on it to allow for an interaction with the propagating wave. The objectives are as follows: (i) demonstrate large-scale mm-size growth via chemical vapor deposition of single layer MoS_2/WSe_2 directly onto a piezoelectric $LiNbO_3$ substrate, (ii) fabricate a hybrid FET – SAW device by lithographic definition, (iii) measure transport utilizing conventional electrical contacts, and (iv) investigate the acoustoelectric properties of MoS_2/WSe_2.

1.7 Summary and Outline

The experiments presented in this thesis explore the acoustoelectric and electric properties in single-layer TMDs. This chapter introduces the background of 2D materials and the acoustoelectric effect. It then proposes the implementation of $LiNbO_3$ with a lower bandgap material, such as single-layer MoS_2 and

WSe_2, in order to hybridize a device with the functionality of SAWs and FETs. Chapter 2 reviews the experimental techniques used to conduct the experiments contained in this thesis. After these preliminary chapters, the main body of this thesis presents the experimental results. Chapter 3 reports on the acoustoelectric charge transport and the analysis of the electrical transport measurements of a MoS_2-based hybrid device. Chapter 4 presents the integration of a WSe_2-based hybrid device and reports on the acoustoelectric and electrical transport. Chapter 5 explains the photoresponse of MoS_2 and the creation of an acoustic photodetector. Lastly, Chapter 6 presents a concluding discussion of the experiments and analyses presented in this thesis.

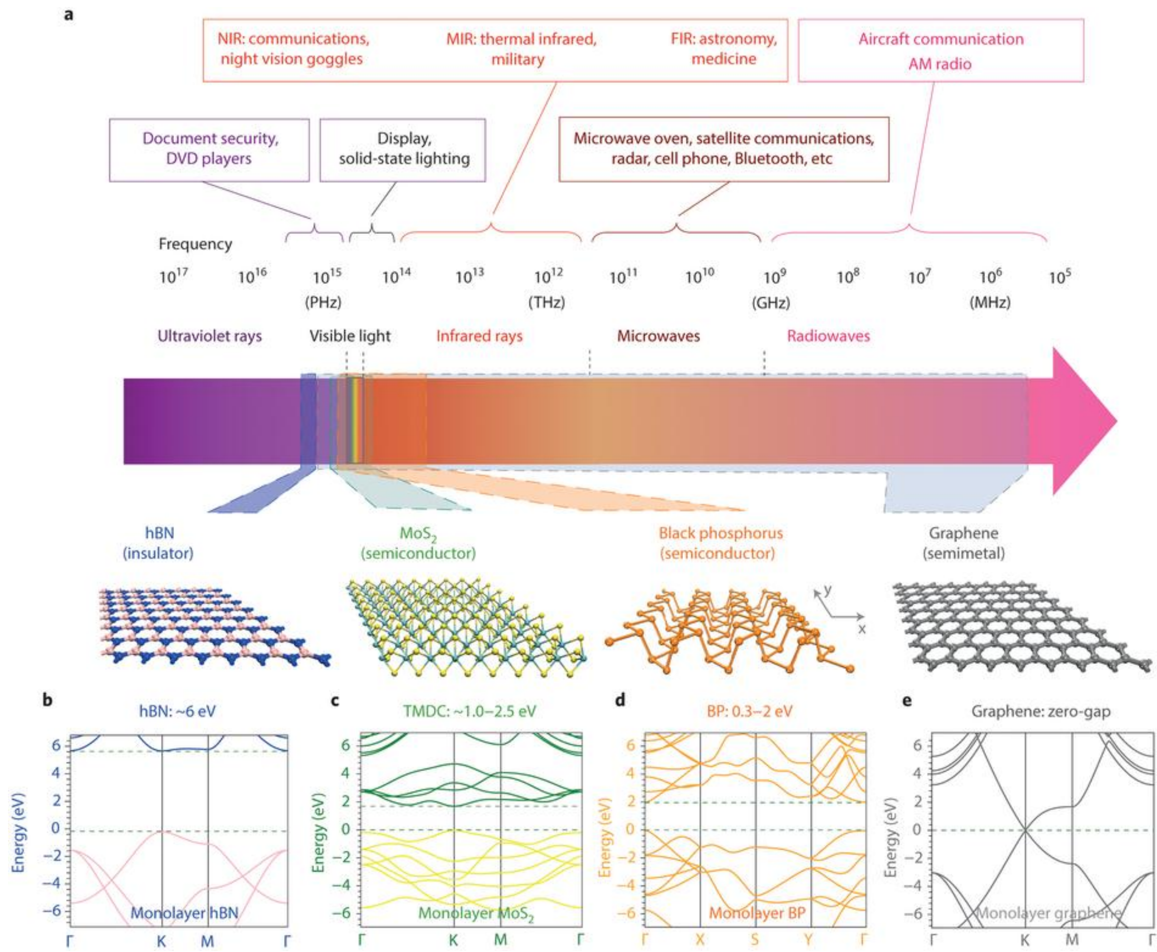

Figure 1.1 | 2D materials covering a broad spectra range: A) Electromagnetic spectrum and different applications in the top portion. Atomic structures of hBN, MoS_2, BP, & graphene B-E) Band structure of B) hBN, C) MoS_2, D) BP, and E) graphene [1.65]

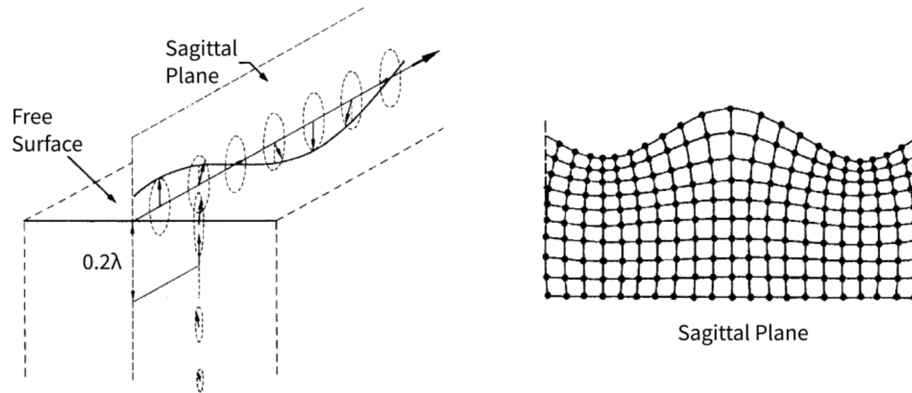

Figure 1.2 | Propagation of a Rayleigh wave on a semi-infinite elastic solid: The energy and field displacements are concentrated within roughly a wavelength from the surface down into the substrate. At the surface, the particles move in an elliptical motion contained in the sagittal plane. The right panel depicts the side view in the sagittal plane [1.44]

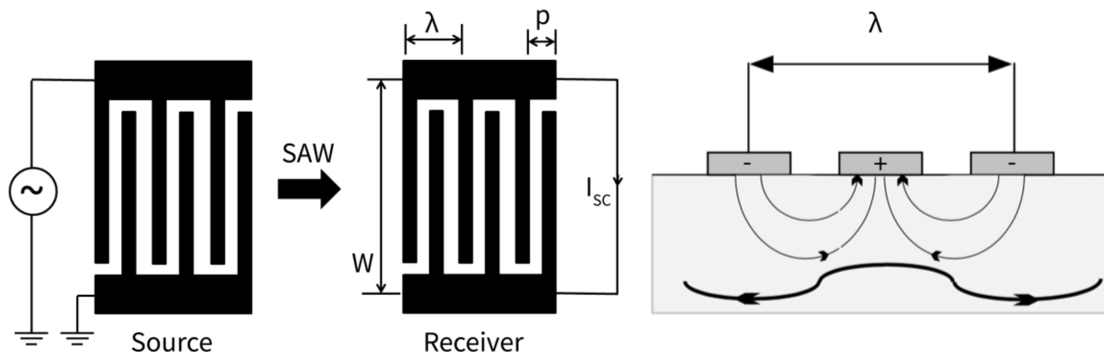

Figure 1.3 | IDT schematic: The schematic of an input and output transducer used in the generation of SAWS where λ is the SAW wavelength, p is the IDT period, and W is the aperture width. On the right panel, the SAW and electric field are schematically sketched.

Table 1.1 | $LiNbO_3$ Properties

Material:	$LiNbO_3$
Crystal Class	Trigonal, 3m
Elastic Constant [10^{10} N/m^2]:	$c_{ij} = \begin{pmatrix} 20.3 & 5.3 & 7.5 & 0.9 & 0 & 0 \\ 5.3 & 20.3 & 7.5 & -0.9 & 0 & 0 \\ 7.5 & 7.5 & 24.5 & 0 & 0 & 0 \\ 0.9 & -0.9 & 0 & 6.0 & 0 & 0 \\ 0 & 0 & 0 & 0 & 6.0 & 0.9 \\ 0 & 0 & 0 & 0 & 0.9 & 7.5 \end{pmatrix}$
Piezoelectric Constant [C/m^2]	$e_{ij} = \begin{pmatrix} 0 & 0 & 0 & 0 & 3.7 & -2.5 \\ -2.5 & 2.5 & 0 & 3.7 & 0 & 0 \\ 0.2 & 0.2 & 1.3 & 0 & 0 & 0 \end{pmatrix}$
Dielectric Constant [ε_0]	$\varepsilon_{ik}^{S} = \begin{pmatrix} 85 & 0 & 0 \\ 0 & 85 & 0 \\ 0 & 0 & 85 \end{pmatrix}$

1.8 References

[1.01] Feynman, R. P. (1999). There's plenty of room at the bottom. Feynman and computation. J. G. H. Anthony, Perseus Books: 63-76.

[1.02] Novoselov, K. S., et al. (2004). "Electric field effect in atomically thin carbon films." Science **306**(5696): 666-669.

[1.03] Novoselov, K. S., et al. (2005). "Two-dimensional atomic crystals." Proc Natl Acad Sci U S A **102**(30): 10451-10453.

[1.04] Bolotin, K. I., et al. (2008). "Ultrahigh electron mobility in suspended graphene." Solid State Communications **146**(9-10): 351-355.

[1.05] Balandin, A. A., et al. (2008). "Superior thermal conductivity of single-layer graphene." Nano Lett **8**(3): 902-907.

[1.06] Wang, X., et al. (2008). "Room-temperature all-semiconducting sub-10-nm graphene nanoribbon field-effect transistors." Phys Rev Lett **100**(20): 206803.

[1.07] Mak, K. F., et al. (2010). "Atomically thin MoS(2): a new direct-gap semiconductor." Phys Rev Lett **105**(13): 136805.

[1.08] Splendiani, A., et al. (2010). "Emerging photoluminescence in monolayer MoS2." Nano Lett **10**(4): 1271-1275.

[1.09] Yun, W. S., et al. (2012). "Thickness and strain effects on electronic structures of transition metal dichalcogenides: 2H-MX2semiconductors (M=Mo, W;X=S, Se, Te)." Physical Review B **85**(3).

[1.10] Ramasubramaniam, A. (2012). "Large excitonic effects in monolayers of molybdenum and tungsten dichalcogenides." Physical Review B **86**(11).

[1.11] Yazyev, O. V. and A. Kis (2015). "MoS2 and semiconductors in the flatland." Materials Today **18**(1): 20-30.

[1.12] Kumar, A. and P. K. Ahluwalia (2012). "Electronic structure of transition metal dichalcogenides monolayers 1H-MX2 (M = Mo, W; X = S, Se, Te) from ab-initio theory: new direct band gap semiconductors." The European Physical Journal B **85**(6).

[1.13] Le, D., et al. (2015). "Spin-orbit coupling in the band structure of monolayer WSe2." J Phys Condens Matter **27**(18): 182201.

[1.14] Radisavljevic, B., et al. (2011). "Single-layer MoS2 transistors." Nat Nanotechnol **6**(3): 147-150.

[1.15] Ataca, C., et al. (2012). "Stable, Single-Layer MX2Transition-Metal Oxides and Dichalcogenides in a Honeycomb-Like Structure." The Journal of Physical Chemistry C **116**(16): 8983-8999.

[1.16] Stewart, J. A. and D. E. Spearot (2013). "Atomistic simulations of nanoindentation on the basal plane of crystalline molybdenum disulfide (MoS2)." Modelling and Simulation in Materials Science and Engineering **21**(4): 045003.

[1.17] Ganatra, R. and Q. Zhang (2014). "Few-layer MoS2: a promising layered semiconductor." ACS Nano **8**(5): 4074-4099.

[1.18] Ellis, J. K., et al. (2011). "The indirect to direct band gap transition in multilayered MoS2 as predicted by screened hybrid density functional theory." Applied Physics Letters **99**(26): 261908.

[1.19] Kuc, A., et al. (2011). "Influence of quantum confinement on the electronic structure of the transition metal sulfideTS2." Physical Review B **83**(24).

[1.20] Kadantsev, E. S. and P. Hawrylak (2012). "Electronic structure of a single MoS2 monolayer." Solid State Communications **152**(10): 909-913.

[1.21] Chakraborty, B., et al. (2013). "Layer-dependent resonant Raman scattering of a few layer MoS2." Journal of Raman Spectroscopy **44**(1): 92-96.

[1.22] Wieting, T. J. and J. L. Verble (1971). "Infrared and Raman Studies of Long-Wavelength Optical Phonons in Hexagonal MoS2." Physical Review B **3**(12): 4286-4292.

[1.23] Ramana, C. V., et al. (2008). "Oxidation and metal-insertion in molybdenite surfaces: evaluation of charge-transfer mechanisms and dynamics." Geochem Trans **9**: 8.

[1.24] Lee, C., et al. (2010). "Anomalous lattice vibrations of single- and few-layer MoS2." ACS Nano **4**(5): 2695-2700.

[1.25] Lembke, D. and A. Kis (2012). "Breakdown of high-performance monolayer MoS2 transistors." ACS Nano **6**(11): 10070-10075.

[1.26] Yin, Z., et al. (2012). "Single-layer MoS2 phototransistors." ACS Nano **6**(1): 74-80.

[1.27] Lopez-Sanchez, O., et al. (2013). "Ultrasensitive photodetectors based on monolayer MoS2." Nat Nanotechnol **8**(7): 497-501.

[1.28] Zhang, W., et al. (2014). "Ultrahigh-gain photodetectors based on atomically thin graphene-MoS2 heterostructures." Sci Rep **4**: 3826.

[1.29] Rathi, S., et al. (2015). "Tunable Electrical and Optical Characteristics in Monolayer Graphene and Few-Layer MoS2 Heterostructure Devices." Nano Lett **15**(8): 5017-5024.

[1.30] Voß, D., et al. (1999). "Atomic and electronic structure ofWSe2fromab initiotheory: Bulk crystal and thin film systems." Physical Review B **60**(20): 14311-14317.

[1.31] Chang, C.-H., et al. (2013). "Orbital analysis of electronic structure and phonon dispersion in MoS2, MoSe2, WS2, and WSe2monolayers under strain." Physical Review B **88**(19).

[1.32] Zhang, Y., et al. (2016). "Electronic Structure, Surface Doping, and Optical Response in Epitaxial WSe2 Thin Films." Nano Lett **16**(4): 2485-2491.

[1.33] Zhao, W., et al. (2013). "Evolution of electronic structure in atomically thin sheets of WS2 and WSe2." ACS Nano **7**(1): 791-797.

[1.34] Zeng, H., et al. (2013). "Optical signature of symmetry variations and spin-valley coupling in atomically thin tungsten dichalcogenides." Sci Rep **3**: 1608.

[1.35] Podzorov, V., et al. (2004). "High-mobility field-effect transistors based on transition metal dichalcogenides." Applied Physics Letters **84**(17): 3301-3303.

[1.36] Fang, H., et al. (2012). "High-performance single layered WSe(2) p-FETs with chemically doped contacts." Nano Lett **12**(7): 3788-3792.

[1.37] Resta, G. V., et al. (2016). "Polarity control in WSe2 double-gate transistors." Sci Rep **6**: 29448.

[1.38] Ghorbani-Asl, M., et al. (2013). "Defect-induced conductivity anisotropy in MoS2monolayers." Physical Review B **88**(24).

[1.39] Rayleigh, L. (1885). "On Waves Propagated along the Plane Surface of an Elastic Solid." Proceedings of the London Mathematical Society **s1-17**(1): 4-11.

[1.40] Auld, B. A. and B. A. Auld (1973). Acoustic fields and waves in solids, Wiley.

[1.41] Curie, J. and P. Curie (1880). "Development, via compression, of electric polarization in hemihedral crystals with inclined faces." Bulletin de la Societe de Minerologique de France **3**: 90-93.

[1.42] Lippmann, G. (1881). "Principe de la conservation de l'électricité, ou second principe de la théorie des phénomènes électriques." Journal de Physique Théorique et Appliquée **10**(1): 381-394.

[1.43] Curie, J. and P. Curie (1881). "Contractions and expansions produced by voltages in hemihedral crystals with inclined faces." Comptes Rendus **93**: 1137-1140.

[1.44] Campbell, C. (1989). Surface acoustic wave devices and their signal processing applications, Academic Press.

[1.45] White, R. M. and F. W. Voltmer (1965). "Direct Piezoelectric Coupling to Surface Elastic Waves." Applied Physics Letters **7**(12): 314-316.

[1.46] Reindl, L. M., et al. (2001). "SAW-based radio sensor systems." IEEE Sensors Journal **1**(1): 69-78.

[1.47] Slobodnik, A. J. (1976). "Surface acoustic waves and SAW materials." Proceedings of the IEEE **64**(5): 581-595.

[1.48] Ruppel, C. C. W., et al. (2002). "SAW devices and their wireless communications applications." IEEE Microwave Magazine **3**(2): 65-71.

[1.49] Arizmendi, L. (2004). "Photonic applications of lithium niobate crystals." physica status solidi (a) **201**(2): 253-283.

[1.50] Kösters, M., et al. (2009). "Optical cleaning of congruent lithium niobate crystals." Nature Photonics **3**(9): 510-513.

[1.51] Bhatt, R., et al. (2012). "Urbach tail and bandgap analysis in near stoichiometric LiNbO3 crystals." physica status solidi (a) **209**(1): 176-180.

[1.52] Parmenter, R. H. (1953). "The Acousto-Electric Effect." Physical Review **89**(5): 990-998.

[1.53] Weinreich, G. (1956). "Acoustodynamic Effects in Semiconductors." Physical Review **104**(2): 321-324.

[1.54] Weinreich, G., et al. (1959). "Acoustoelectric Effect inn-Type Germanium." Physical Review **114**(1): 33-44.

[1.55] Hutson, A. R. and D. L. White (1962). "Elastic Wave Propagation in Piezoelectric Semiconductors." Journal of Applied Physics **33**(1): 40-47.

[1.56] Wixforth, A., et al. (1989). "Surface acoustic waves on GaAs/AlxGa1−xAs heterostructures." Physical Review B **40**(11): 7874-7887.

[1.57] Tien, P. K. (1968). "Nonlinear Thoery of Ultrasonic Wave Amplification and Current Saturation in Piezoelectric Semiconductors." Physical Review **171**(3): 970-986.

[1.58] Rotter, M., et al. (1998). "Giant acoustoelectric effect in GaAs/LiNbO3 hybrids." Applied Physics Letters **73**(15): 2128-2130.

[1.59] Ingebrigtsen, K. A. (1970). "Linear and Nonlinear Attenuation of Acoustic Surface Waves in a Piezoelectric Coated with a Semiconducting Film." Journal of Applied Physics **41**(2): 454-459.

[1.60] Wixforth, A., et al. (1986). "Quantum oscillations in the surface-acoustic-wave attenuation caused by a two-dimensional electron system." Phys Rev Lett **56**(19): 2104-2106.

[1.61] Miseikis, V., et al. (2012). "Acoustically induced current flow in graphene." Applied Physics Letters **100**(13): 133105.

[1.62] Bandhu, L., et al. (2013). "Macroscopic acoustoelectric charge transport in graphene." Applied Physics Letters **103**(13): 133101.

[1.63] Santos, P. V., et al. (2013). "Acousto-electric transport in epitaxial monolayer graphene on SiC." Applied Physics Letters **102**(22): 221907.

[1.64] Poole, T., et al. (2015). "Acoustoelectric photoresponse in graphene." Applied Physics Letters **106**(13): 133107.

[1.65] Fengnian Xia, H. W., Di Xiao, Madan Dubey and Ashwin Ramasubramaniam (2010). "Two-dimensional material nanophotonics." Nature Photonics **8**(12): 899-907.

[1.66] Preciado, E., et al. (2015). "Scalable fabrication of a hybrid field-effect and acousto-electric device by direct growth of monolayer $MoS_2/LiNbO_3$." Nat Commun **6**: 8593.

2 Experimental Techniques

2.1 Introduction

The following chapter describes the specific steps involved in the scalable fabrication and characterization of 2D TMDs. The growth quality of these materials is particularly crucial for device integration and requires attention to detail. Therefore, this chapter also describes the techniques used to identify single-layer TMDs. Upon achieving the precise thickness, the next necessary step is to measure charge carrier transport properties of TMDs in devices, which requires precise patterning techniques. The ability to pattern devices allows for materials physics at the single-layer limit, which cannot be observed in its bulk counterpart. To accomplish this, lithographic patterning and deposition techniques provide an ideal method to allow for the fabrication of hybrid devices. Additionally, quantification of the electrical and optical properties of the devices discussed in this thesis requires sensitive experimental techniques. The details of the measurement setup are provided to define how the data is extracted from the experiments. The methodologies described in this chapter provide a foundation for the successful execution of these experiments.

2.2 Materials and Structural Characterization Techniques

The following section introduces the equipment used to identify the unique properties found in 2D materials. Each tool provides imperative information for continuing towards device integration. All

instruments used were readily available in facilities at the University of California, Riverside and University of Augsburg.

2.2.1 Raman Spectroscopy

Raman spectroscopy is an effective and non-destructive method for measuring rotational, vibrational, and electronic energy levels in a system. This powerful tool is based on the inelastic scattering of light, wherein the frequency of light changes upon interaction with a sample. For example, photons of a constant wavelength irradiated by a laser source are absorbed by the electrons in the sample and then reemitted when these excited electrons relax back to the ground state. Some of the reemitted photons provided by the laser are shifted up or down in comparison with the original light. This shift in energy between the input and the output light yield information about the material's unique modes of vibration. Figure 2.1 illustrates in this process.

The Raman shift (Δw) is given in wavenumbers as the following:

$$\Delta w = \frac{1}{\lambda_0} - \frac{1}{\lambda_1} \qquad \text{Equation 2.1}$$

Here, λ_0 and λ_1 are the wavelengths of the incident and emitted photons, respectively. The Raman shift is measured in inverse centimeters (cm^{-1}). This technique has been used to determine the vibrational modes of van der Waals materials, such as TMDs and graphene [2.01].

All measurements were done with the confocal Horiba LabRAM HR instrument, depicted in Figure 2.2. A green laser with an excitation wavelength of 532 nm was directed towards the sample with a 100x objective. The spatial resolution was diffraction limited to a laser spot that was about 1 μm in size. Each measurement was performed at an acquisition time of two seconds and at room temperature. The Raman

signal was recorded on a grating setting of 1,800 lines per mm. During the measurement, the laser was maintained at 0.1 mW to avoid thinning the sample.

2.2.2 Photoluminescence Spectroscopy

Photoluminescence is an optical method used to characterize the direct bandgap of semiconductors by analyzing the optical response of an object exposed to excitation light. In the PL experiment, a light source with photon energies larger than the bandgap is used to create electron holes pairs. In particular, a photo-generated electron drops to the bottom of the valence band (VB) as a photo-generated hole floats to top of the conduction band (CB) to attain lower energies. The electron hole pair recombines and the emission of photons is detected. Figure 2.2 depicts the PL process. Photoluminescence spectroscopy was performed with the same laser excitation and conditions on the same instrument utilized to measure Raman.

2.3 Fabrication Techniques

The following section introduces the specific steps involved in fabricating devices. All devices used in this thesis were the result of an intricate fabrication process inside of a class 100 cleanroom and were developed by analysis over several samples. The following techniques were made possible in either CNSE facility at UC Riverside or Experimental Physics Cleanroom at University of Augsburg. These locations provided the necessary tools for the successful fabrication of all devices.

2.3.1 Lithography

Lithography is the foundation of fabrication. This process comprises the exposition and development of a polymer resist to form a pattern. The patterned features serve as templates for selectively adding or removing material, which is referred to as lift-off or etch process, respectively. In this case, electron beam

lithography (EBL) defines patterns to selectively add metal to the structure. Figure 2.3 depicts the general scheme.

Polymer resists are classified into two groups: positive and negative. A positive resist breaks down polymer chains during electron beam exposure and softens the resist exposed to the beam to assist in its removal with developer. Alternatively, a negative resist cross-links, and the retention of exposed areas is achieved through immersion in developer while the rest of the area washes away. The majority of patterning undertaken in this study was accomplished using a Leo SUPRA 55 EBL system with SEM capability. The e-beam voltages ranged up to 30 kV, with a resolution of 1.1 nm at 20 kV.

Design CAD software is used to design the device layout and create pattern files. A separate run process file must be created using the Nano Pattern Generation System (NPGS) software. The run process file allows the user to define parameters, such as exposure dose, spacing, beam current, and magnification.

After e-beam exposure, the sample is developed. This requires immersion of the sample in a developer solution that contains one part methyl isobutyl ketone (MIBK) and three parts isopropyl alcohol (IPA) for 30 seconds at room temperature. The developed patterned is rinsed in IPA for 30 seconds to stop the development process and gently dried with N_2 gas. The developed pattern is checked under the optical microscope to verify the structure is well defined.

After finalizing the developed structure, the pattern is ready for metal deposition. This is typically accomplished by using processes such as electron beam evaporation or magnetron sputtering. The deposition rate was kept low to avoid heating of the resist above the glass transition temperature in PMMA.

The last stage of the fabrication process involves a lift-off step to remove any excess resist that was not patterned. In turn, the metal that was placed inside the pattern is not removed due to strong adhesion to the sample. A solvent, such as acetone, is boiled at 60 °C to ensure a clean surface and remove any polymer

residue. The sample is then blown dry with N_2 and inspected under the microscope to verify the device completion.

2.4 Chemical Vapor Deposition

The most convenient and cost-effective method for synthesizing high-quality and large-area films is chemical vapor deposition (CVD). This method is widely employed in the semiconductor industry to deposit a large class of semiconductors. Only recently has it been applied for the growth of low-dimensional materials, such as graphene and TMDs. Such efforts include assortment of CVD schemes that include solid and/or gas precursors. The CVD technique used for growing TMDs in Bartels group consists of vaporizing elemental precursors to a certain temperature. An inert gas allows for the vapor to flow and coalesce into a continuous film and onto a substrate. The growth process normally runs for 5 to 10 minutes. Different growth parameters provide various film compositions. For example, different compositions are possible, such as large-scale films in the order of millimeters or small micron-sized islands in the shape of triangles. Figure 2.4 provides a schematic of a typical CVD setup.

2.5 Generation and Detection of SAWs

A SAW requires an IDT to propagate waves in a piezoelectric substrate. The following instrumentation assists in creating such waves, which is useful for later chapters in this thesis.

2.5.1 Generating SAWs

This section provides the instruments necessary to propagate SAWs. Figure 2.5 depicts an RF generator that is utilized to excite the IDT for the creation of propagating surface waves. The particular model used in this study is an SG362 model from Stanford Research Systems. This has two outputs and covers a frequency

range of up to 2.02 GHz. The maximum output power is 16.5 dBm, with an output impedance of 50 Ω. The system is capable of generating and modulating different types of waveforms. An amplifier is frequently used to amplify the signal from the function generator by a factor of + 17 dB.

2.5.2 Network Analyzer

A vector network analyzer was used to verify the frequency response (Figure 2.6). This instrument provides a controlled signal to the input of a device under test (DUT), then records and displays the output of the DUT in terms of magnitude relative to the input as a function of frequency. Light waves are used to illustrate a comparison. For example, when light is sent to a lens, some of the incident light is reflected back, while some is transmitted through the lens. Figure 2.6 highlights this process.

The reflection and transmission parameters of this study were defined in terms of scattering (S) parameters in a two-port network system [2.02]. The S parameter is a ratio of input signal to output signal that is represented by $S_{\text{Input / Output}}$. The S-parameters are given by:

Forward Reflection Coefficient $$S_{11} = \frac{\text{Reflected}}{\text{Incident}} = \frac{b_1}{a_1}\bigg|\, a_2 = 0$$ Equation 2.2

Forward Transmission Coefficient $$S_{21} = \frac{Transmitted}{Incident} = \frac{b_2}{a_1}\bigg|\, a_2 = 0$$ Equation 2.3

2.6 Transport Setup

Source meter units (SMUs) were utilized to supply a voltage or current and were limited to a certain compliance in order to avoid damaging the DUT. Two-point characterization was performed using a Keithley 2400 SMU. For four-point characterization, a Keithley K2400 SMU was used only as a constant current source (no measurement probes connected) and the voltage at the potential probes was recorded directly by a Keithley K2000 digital multimeter. The gate voltage was applied by a Keithley K2600 SMU,

which measured the gate leakage current at the same time. The Keithley K2600 SMU is limited to a voltage range of ± 40 V. All the instruments connect to a main computer via GPIB cables and given commands by LabView. This software allows multiple parameters for each measurement. Remote connection allowed researchers to work from another computer in order to prevent any interference from the lab while the measurements were running. Figure 2.7 depicts the setup used for the electrical transport characterization.

2.7 Optical Setup

All optical measurements were performed on a typical micro-PL setup. This process consists of a laser beam that is focused by a lens onto a sample, resulting in the excitation of charge carrier pairs. After a short time decay, the electron-hole pairs recombine and emit a photon that is collected by the same objective. A beam splitter collects and sends the emitted photon to the detection path. The setup used for this study included two 50x objectives: one for the visible spectral range (N.A. = 0.50) and the other for the near-infrared range (N.A. = 0.55). The sample is placed inside of helium flow cryostat and can be pumped down to a certain pressure. Different lasers are available to generate charge carriers, and each laser can be coupled into the beam path individually. Additional filters are used to adjust the power, as well as to suppress any noise from the laser. A power meter is coupled to the beam splitter to measure the laser power. The experiment relied on a red (660 nm ~ 1.88 eV) and an infrared (850 nm ~ 1.46 eV) pulsed semiconductor laser, with an 80-MHz repetition rate and pulse duration of ≤ 100 ps. The laser spot size was likely greater than 2 µm, as the glass cryostat cover may have influenced the beam path; otherwise, the diffraction-limited beam size would be 1.5 µm for infrared and 1.3 µm for red (d = wavelength / N.A.). A piezoelectric translation stage is used to move the laser beam with magnitude precision. The beam splitter supplies the light that is collected from the lens for detection. The signal is focused on the entrance slit of a spectrometer. A cooled CCD with liquid nitrogen was used as the detector, with a grid of 1,200 lines per mm. Once the CCD reached an adequate temperature, it was possible to perform a large-area PL scan on

the as-grown TMD film to validate the extent of single-layer thickness before device fabrication. Figure 2.8 presents how the instrument is set up.

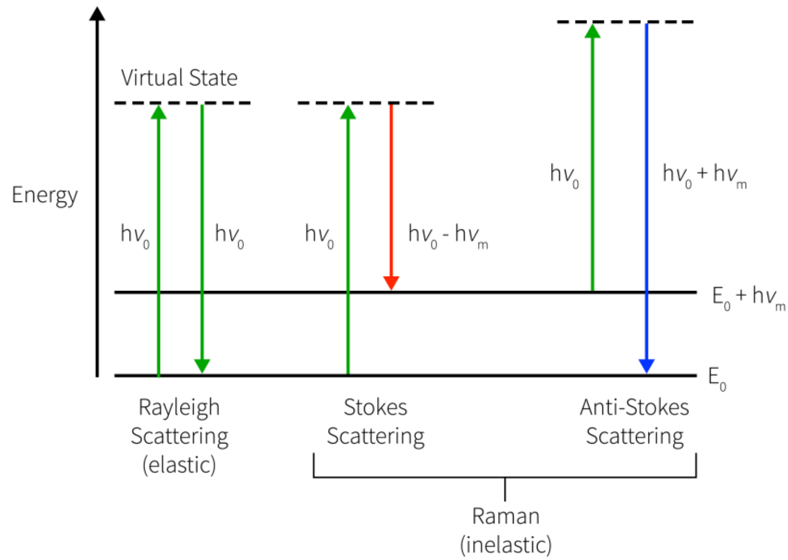

Figure 2.1 | Raman: Energy-level diagram showing the energy change in Raman (inelastic) and Rayleigh (elastic) scattering, where E_0 is the ground state, hv_m is the energy difference after scattering, and hv_0 is the energy of the incident beam

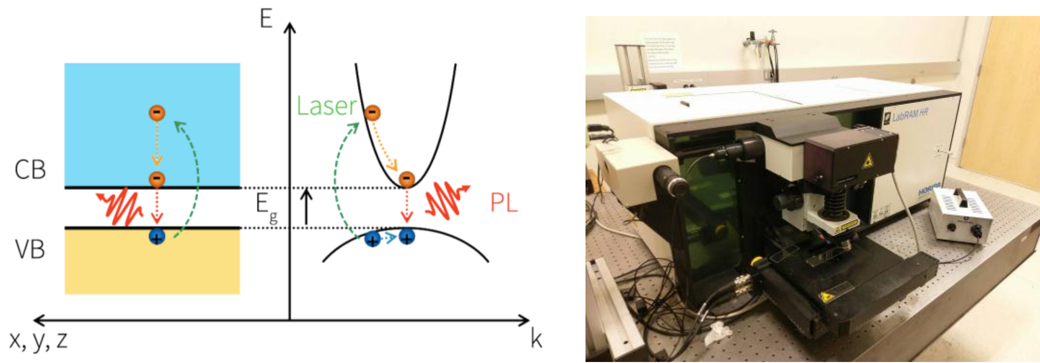

Figure 2.2 | Mechanism of PL in the local space and k-space: A laser pulse (green) with an E > Eg lifts an electron (orange) from the fully occupied VB into the empty CB leaving behind a hole (blue). The charge carriers relax into the band minimum (electrons) or maximum (holes) and in doing so release their excess energy. Subsequently, the electron and hole recombine to emit a photon (red), which is detected as PL signal. On the right panel Horiba LabRAM HR instrument used to measure Raman and PL characteristics

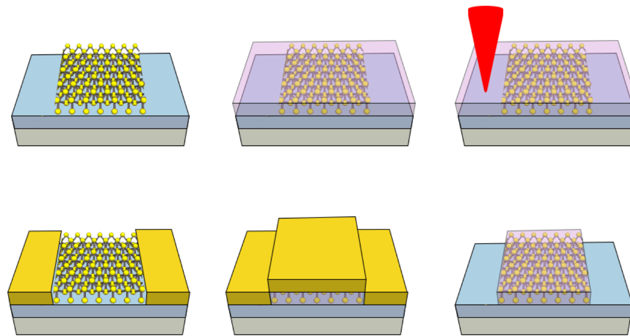

Figure 2.3 | Lithographic Patterning. A) Material of interest is identified B) Bi-layer resist is spun onto a substrate to a desired thickness C) The resist is then exposed using an electron beam to change its chemical composition D) The bi-layer resists is developed E) Metals are then deposited F) and the excess is removed by stripping the bi-layer resist, leaving the desired metallized pattern

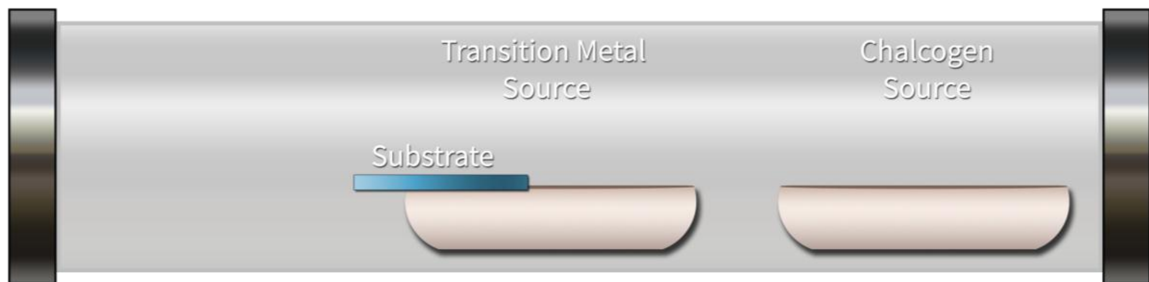

Figure 2.4 | CVD furnace schematic: A typical growth setup is depicted. Transition metal powder is placed inside an alumina crucible, whereas a chalcogen precursor is placed in opposing crucible.

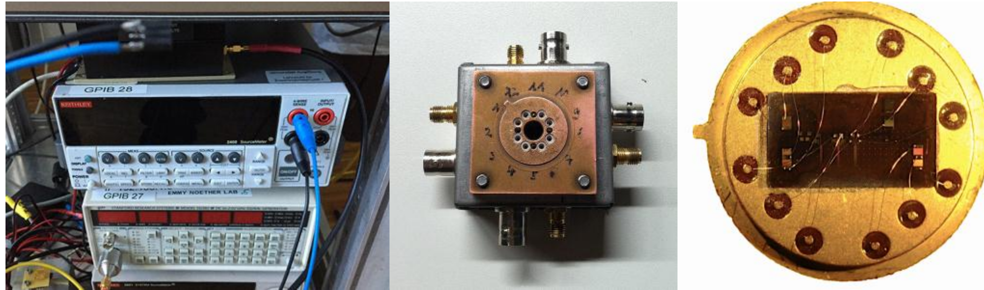

Figure 2.5 | RF Characterization: Left) Stanford Research System signal generator is used to source a RF signal to the input IDT Middle) Homemade carrier includes RF and BNC connections for electrical measurements Right) Chip carrier used, where wires bond the metallic pads from the substrate to metallic leads on the gold chip carrier.

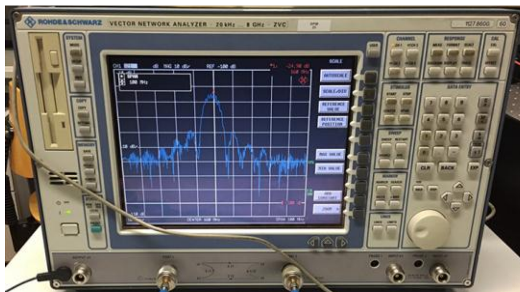

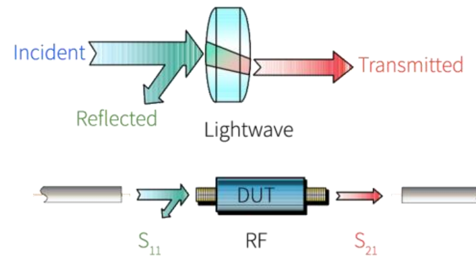

Figure 2.6 | Vector network analyzer and light wave analogy: Left) A two-port VNA is used to analyze the DUT, where the transmission depicted at frequency of 159 MHz Right) Imagine traveling waves along a transmission line in terms of a light wave. Reflection in RF energy occurs when impedance is not the same, just like mirror in a light analogy. A lens will allow for some light to transmit, just much we would see in the transmission parameter S_{21} [2.02]

Figure 2.7 | Transport Setup: SMU used for the electrical characterization of the hybrid device. Keithley 2400 for constant current source and measurement of the voltage drop. Keithley 2600 was used to apply bias voltages and measure leakage current in the system. The right panel identifies the metallic leads used to connect the chip carrier to the BNC cables connected to its according SMU

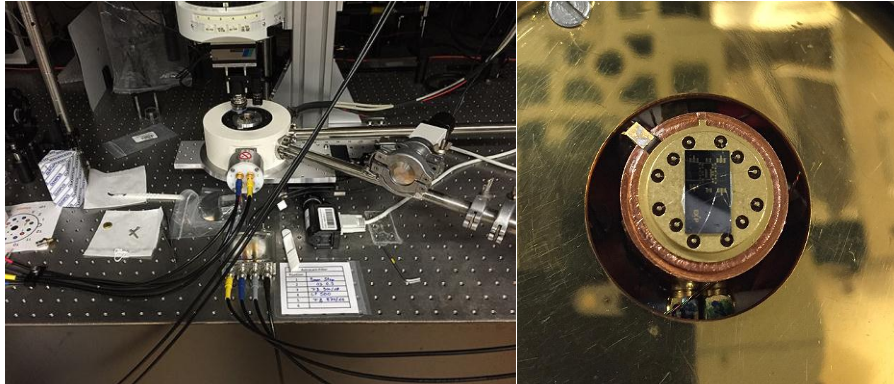

Figure 2.8 | Optical setup for testing the attenuation with a laser source. The chip carrier and its metallic leads are inserted inside open slots inside a helium cryostat

2.8 References

[2.01] Chakraborty, B., et al. (2013). "Layer-dependent resonant Raman scattering of a few layer MoS2." Journal of Raman Spectroscopy **44**(1): 92-96.

[2.02] Ndagijimana, F. (2014). "The S-Parameters Testing Technique." 89-115.

[2.03] Preciado, E., et al. (2015). "Scalable fabrication of a hybrid field-effect and acousto-electric device by direct growth of monolayer MoS2/LiNbO3." Nat Commun **6**: 8593.

3 Hybrid SAW-FET MoS_2

3.1 Introduction

$LiNbO_3$ is the archetypical ferroelectric material and substrate of choice for numerous applications, including SAW RF devices and integrated optics. It offers a unique combination of substantial piezoelectric and birefringent properties, yet its lack of optical activity and semiconducting transport hampers application in optoelectronics. This study fabricates and characterizes a hybrid $MoS_2/LiNbO_3$ acoustoelectric device via a scalable route that uses millimeter-scale direct CVD of MoS_2, followed by lithographic definition of a FET structure on top. The prototypical device exhibits electrical characteristics that are competitive with MoS_2 devices on silicon. Surface acoustic waves excited on the substrate can manipulate and probe the electrical transport in the monolayer device where a sound-driven battery is realized.

3.2 Experimental Methods

The following section introduces the growth process necessary to grow single-layer MoS_2. It is imperative to establish strong adhesion to the substrate in order to measure acoustoelectric effects directly from the accompanying electric fields that correlate to the propagating SAW. From that point forward, Raman and PL spectroscopy are used to determine the extent of single-layer material present on the substrate. Spatial

PL maps measure the area of highest emission and therefore help determine the proper placement of electrical structures, such as electrodes and IDTs.

3.2.1 Sample Preparation of Single-Layer MoS_2

This thesis used a CVD method that consists of a solid-source scheme to synthesize single-layer MoS_2, which was established by the Bartels research group [3.01]. A typical setup utilized two alumina crucibles containing 25 mg of molybdenum trioxide (MoO_3) powder and 1 g of sulfur powder as the Mo and S sources, respectively. These precursors were placed inside a two-inch diameter quartz process tube, which was inserted into a Mellen TT12 furnace. The alumina crucible containing the Mo source was placed at the center of the heated zone. A black 128°YX-cut $LiNbO_3$ 9 mm x 5 mm substrate with a thickness of 500 µm or a silicon substrate 20 mm x 20 mm with an oxide thickness of 300 nm was mounted with a Mo mesh on the edge of the crucible. The other crucible, which contained S, was placed upstream at a distance of 25 cm from the center. The position of the crucible was optimized to allow for the S powder to melt and form a uniform liquid as soon as the furnace reached a desired temperature. Once the precursors and substrate were placed inside the tube furnace, a rapid flow of nitrogen gas at 5 SCFH was used to purge the tube. Subsequent film growth occurred at a reduced nitrogen flow rate of 0.5 SCFH. The center zone of the furnace was heated at a rate of 12.5 °C min^{-1}, held at ~ 650 °C for 20 minutes, and then allowed to cool naturally to room temperature. Nitrogen carrier gas aided the transfer of the sulfur vapor to the sample region for optimal growth. The temperature was measured by a type-K thermocouple at the outer surface of the process tube.

3.2.2 Raman Characterization of Single-Layer MoS_2

Raman spectroscopy is used to estimate the number of layers present in MoS_2 with regards to the frequency shift difference of the in-plane and out-of-plane mode. As a comparison, silicon with a 300 nm

thermal oxide reference substrate was grown under the same conditions as $LiNbO_3$ to identify the dominant vibration modes present in MoS_2 (Figure 3.1). Particularly, the contrast of MoS_2 above this type of oxide thickness assists with optical identification of the film. This research focused on the in-plane mode of two sulfur atoms with respect to the molybdenum atom (E^1_{2g} band) and the out-of-plane mode of sulfur atoms in the opposite direction (A_{1g} band). The experimental Raman spectrum exhibited three main peaks, which were taken in a range between 150 cm^{-1} and 550 cm^{-1} when using a laser wavelength of 532 nm. The peak with the strongest intensity stemmed from silicon and was centered at 520 cm^{-1}. The in-plane mode (E^1_{2g}) was observed at 385 cm^{-1}, and out-of-plane mode (A_{1g}) at 403 cm^{-1}. The change in frequency separation of the in-plane and out-of-plane mode yielded a value of 18 cm^{-1}, which was in good agreement with single-layer MoS_2. Therefore, this confirmed the growth of MoS_2 on the reference substrate to be single layer and provided a reference to compare the growth of MoS_2 on $LiNbO_3$ substrate.

In this process, a blank 128°YX-cut $LiNbO_3$ spectrum was measured prior to growth. Evaluation of the spectrum shown on the left panel of Figure 3.2 revealed many vibration modes. This result stems from the direction of polarization and propagation present in the 128°YX-cut $LiNbO_3$ cut substrate [3.02]. For example, the E transverse symmetry vibration modes present in $LiNbO_3$ have values of 369 cm^{-1} and 430 cm^{-1}, which broaden in the regime where it was expected to see single-layer MoS_2. After the CVD process, the $LiNbO_3$ substrate displayed elongated areas of millimeter size growth continuously covered by MoS_2 film. However, the single-layer MoS_2 signal was hampered due to the dominant signal of the $LiNbO_3$ substrate, and is plotted on the right panel of Figure 3.2. This is visible as the $LiNbO_3$ signal overlaps the E^1_{2g} mode of single-layer MoS_2 at 385 cm^{-1}.

3.2.3 PL Characterization of Single-Layer MoS_2

Figure 3.3 compares normalized PL spectra from the single-layer MoS_2 films grown under nominally-identical conditions on $LiNbO_3$ (black) and on a SiO_2/Si reference substrate (red). For both samples, a PL

peak is clearly resolved, corroborating the single-layer nature of MoS_2. There is a single emission peak at photon energy of 1.86 eV for the silicon reference; however, MoS_2 grown 128°YX-cut $LiNbO_3$ yields PL signal at photon energies larger by 40–50 meV. This shift was attributed to the five-fold larger thermal expansion coefficient of $LiNbO_3$ of 12.6 x 10^{-6} K^{-1} [3.03] compared to that of Si [3.04] of 2.6 x 10^{-6} K^{-1} near room temperature. These dissimilar values caused a net relative compressive strain of 0.35% for the MoS_2 film on $LiNbO_3$ during cool-down from growth temperatures. Compressive strain is expected to give rise to a blue shift of the PL emission. Extrapolation of the data on uniaxial strain reported in reference [3.05] of ΔE = 60 – 70 meV per 1% strain predicts a blue shift of ~ 23 meV, about half of the observed blue shift. Using the values of ΔE = 300 meV per 1% strain that were reported by Hui et al. [3.06] for compressive strain in tri-layer MoS_2, the expected blue shift amounts to 105 meV, which is larger than the value observed here. Thus, the observation of a blue shift in this study is compatible in magnitude with recent work and validates a rigid connection of the MoS_2 film to the $LiNbO_3$ substrate, a precondition for maximum interaction with the SAW.

Figure 3.4 presents an overview map that demonstrates mm-scale growth of single-layer MoS_2. The PL intensity is encoded in a color scale with red and dark regions corresponding to high and low counts, respectively. Intensity differences are likely due to variations in the film domain size [3.01]. In addition, the position of the IDTs and electrical contacts of the FET are placed in region of highest intensity.

3.2.4 Lithographic Patterning

Prior to CVD growth, the $LiNbO_3$ substrate was chemically reduced to yield a crystal with enhanced electrical conductivity and optical absorption [3.07]. The need for a higher conductivity is required to avoid various problems, such as charging during device fabrication and operation. Afterwards, the fabrication of the hybrid device was performed on a region with the highest MoS_2 emission, validated by scanning PL spectroscopy. All lithographic patterning of the IDTs and contacts proceeded in a single-exposure step using an electron beam writer. The fabrication process started as the lithography machine used a serial

writing technique that rasterizes a focused beam of electrons over the sample. A bi-layer of PMMA was used, where the lower layer was exposed more rapidly than the upper layer due to its higher sensitivity. This created an undercut in the resist profile, which facilitated the final lift-off step. To avoid errors in the periodicity of the finger sequence, all fingers of an IDT were positioned within a single write field. Contacts were fabricated by sequential deposition of 10 nm of Ti, followed by 60 nm of Au in an e-beam evaporation tool. Subsequent lift-off defined the active structures. After the fabrication of the electrical contacts, the TMD of interest was selectively removed in a second e-beam exposure step and a subsequent oxygen plasma treatment at a plasma power of 200 W at a pressure of 500 mTorr for 13 s. A 180-µm-wide region across, which the SAW propagates, was left intact.

3.2.5 Measurement Techniques

Surface acoustic wave excitation and transmission experiments: For measurement of the acoustoelectric current and acoustoelectric voltage, the output of an RF signal generator was amplified and connected to one of the IDTs. The RF characteristics of the IDTs and SAW transmission lines were characterized using a vector network analyzer. This measured scattering parameters of the RF network and particularly the scattering parameters S_{11} (reflection) and S_{21} (transmission and insertion loss).

Electrical characterization: Two-point characterization was performed using a Keithley K2400 source meter unit (SMU). For four-point characterization, a K2400 SMU was used only as a constant current source (no measurement probes connected) and the voltage at the potential probes was recorded directly by a K2000 digital multimeter. The gate voltage was applied by a Keithley K2600 SMU, which measured the gate leakage current at the same time. Short-circuit acoustoelectric current and open-circuit acoustoelectric voltage were recorded using a K2400 SMU with $V_{SD} = 0$ and $I_{SD} = 0$, respectively.

Optical Spectroscopy: Photoluminescence and Raman spectroscopy, as well as mapping, utilized a Horiba LabRAM HR spectroscopy system using a 532 nm wavelength excitation laser and 1,800 lines per mm grating.

3.3 Experimental Results

The following section summarizes the experimental results for an assortment of measurements that were utilized to characterize the hybrid device. The configuration allows for measurement of the FET and SAW characteristics. It is notable that electrical transport measurement was applied in both a two-point and four-point electrical wiring configuration, corroborating the presence of an n-type material, as seen in literature. Surface acoustic wave spectroscopy confirmed this attribute with a powerful tool used to identify majority charge carriers present in the system.

3.3.1 Device Layout

Figure 3.5 presents a schematic of the hybrid device. This device consists of two components: (i) a SAW delay line formed by a pair of IDTs and (ii) a single-layer MoS_2 FET between two IDTs. This configuration enabled the researchers to probe and manipulate the electrical characteristics of the FET by exciting and detecting SAWs that were interacting with the carriers in the MoS_2. A four-terminal FET was monolithically defined on the $LiNbO_3$ substrate in the region of maximum emission of our monolayer TMD of choice. Ti/Au metal contacts and IDTs were fabricated for electric and acoustic interfacing to the TMD film, respectively. The layout of the IDT was a split-two design, with 21 finger pairs and a duty cycle of 1:1. The aperture was set at 200 µm so that the connections were also in the direction within the writing field. The IDTs design wavelength was chosen as λ_{SAW} = 25 µm, corresponding to a design frequency of f_{SAW} = 160 MHz. The two IDTs were located at opposite ends of the substrate in a delay line configuration (length 5.4 mm), which

enabled the launch and recording of SAWs propagating at v_{SAW} = 3,980 m s^{-1} in opposite directions across the chip. The studied FET device features a channel length of L = 35 µm and a total width of the conducting channel of W = 360 µm.

3.3.2 Post Spatial Map of Single-Layer MoS_2

Figure 3.6 presents a spatial map of the characteristic single-layer MoS_2 PL emission in the channel region of the FET [3.09]. The PL intensity is encoded in color scale, with red and dark regions respectively corresponding to high and low count rates. In all other areas, the MoS_2 was selectively removed to avoid any signal contributions from these regions. The upper and lower boundaries of the FET were aligned with the SAW propagation path to ensure tight correspondence of the electrically- and acoustically-addressed film area. The $LiNbO_3$ substrate served as the dielectric for back gating to ensure full FET operation. Full electrical characterization of this device is provided later in this chapter.

3.3.3 FET Characterization of Single-Layer MoS_2

The hybrid device is expected to exhibit FET properties. The following equation estimated how much of an electric field can be generated when applying a bias voltage (V_G):

$$D = \frac{\varepsilon_r V_{GS}}{d_{sub}} \quad \text{Equation 3.1}$$

Owing to the immense dielectric constant ε_r ~ 50 for this cut of $LiNbO_3$, moderate electric fields of ± 40 kV/cm can be achieved by applying V_G = ± 40 V between the $LiNbO_3$ backside (thickness $d_{substrate}$ = 500 µm) and the MoS_2 layer. The electrical configuration in Figure 3.7 illustrates a schematic diagram for a two-point and four-point measurement.

Figure 3.8 plots a set of output characteristics by measuring the source drain current (I_{SD}) as a function source drain voltage (V_{SD}), recorded in a two-point (left) and four-point (right) configuration and for different back gate voltages (V_G) ranging between V_G = ± 40 V. As V_G is turned from negative to positive polarity, the sheet resistance is reduced due to accumulation of electrons in the MoS_2 monolayer, as expected. This observation clearly demonstrates FET operation in the hybrid device in the linear regime and the formation of an n-type transport channel, which is in agreement with prior work [3.10-13].

The next step determines the transfer characteristics of the material. This is done by measuring the source drain current (I_{SD}) as a function of back gate voltage (V_G), recorded in a two-point configuration. Transfer characteristics are plotted on the left panel of Figure 3.9 for different source drain voltages (V_{SD}). Again, the increase of I_{SD} as V_G turns to positive bias at constant V_{SD} is consistent with n-type character. In the data, a small leakage current through the substrate was subtracted for clarity. The gate leakage current was weighted by a factor of 2.4 and subtracted from all characteristics. This procedure yields vanishing I_{SD} (V_G) ~0 for V_{SD} = 0. The right side of Figure 3.9 contains the graphs before subtraction of gate leakage and its according graph for each V_{SD}. The transfer characteristics exhibit a small hysteresis, which may arise from poling effects of $LiNbO_3$ at the interface of the MoS_2 layer. Notably, MoS_2-based FETs on dielectric SiO_2/Si substrates have been found to be sensitive to the local environment and, in particular, to the surrounding gas atmosphere [3.14]. Adsorption and desorption of impinging gas atoms and molecules have been suggested as an origin of hysteric I–V characteristics [3.12].

The turn-on behavior allows for the derivation of the threshold voltage V_{th}. This analysis determines the field-effect mobility in the device given by [3.15]:

$$\mu_{FE} = \frac{L}{W} \frac{d_{substrate}}{\varepsilon_r \varepsilon_0} \frac{1}{V_{SD}} \frac{dI_{SD}}{dV_{GS}} \qquad \text{Equation 3.2}$$

Here, L and W are the length and width of the channel, respectively, and $d_{substrate}$ denotes the thickness of the $LiNbO_3$ substrate. Figure 3.10 presents an example analysis.

Due to the hysteric nature of the transfer characteristics, two values were obtained. The field-effect mobility was derived for up-and-down sweep, independently from slop at high gate voltages V_G. Figure 3.11 provides the V_{SD} dependence of the values threshold voltage (V_{th}) and mobility (μ_{FE}).

The output characteristics set allows for the extraction of the channel's electrical properties as a function of back gate voltage V_G. Figure 3.12 depicts the channel conductance extracted from two-point (left) and four-point (right) output characteristics evaluated at $V_{SD} = 0$ and plotted versus V_G. Moreover, from a linear fit of the conductance for $V_G > 20$ V, it is possible to determine the field-effect mobility μ_{FE} and threshold voltage V_{th} from the slope and from the intersection at $I_{SD} = 0$, respectively.

Table 3.1 summarizes the results for μ_{FE} and V_{th}. The error estimates originate from the accuracy of the linear fit and from the standard deviation of 12 V_G up-and-down sweeps for output and transfer characteristics, respectively. The values for μ_{FE} and V_{th} derived from these independent sets of data are in good agreement. It is noted that the values obtained on the high piezoelectric architecture are competitive with back-gated devices fabricated by exfoliation on the SiO_2/Si platform [3.16].

3.3.4 Acoustoelectric Characterization of Single-Layer MoS_2

The hybrid device configuration of this study enables probing of the acoustoelectric properties by exciting and detecting SAWs interacting with carriers in the MoS_2. Interdigital transducers were used for all-electrical excitation and detection of SAWs at a velocity of 3,980 m/s and designed for a frequency of $f_{SAW} = 160$ MHz that corresponds to a wavelength of 25 µm. Their arrangement allows for measurement of the scattering parameters – i.e., the SAW transmission (S_{21}) and reflection (S_{11}) from one IDT to the other. Figure 3.13 plots S_{21} as a function of the RF signal applied to the sending IDT. In this trace, the delay line resonance is resolved as a 40 dB high transmission maximum, very close to the nominal design frequency of $f_{SAW} = 160$ MHz, and it also matches with the frequency response model. Likewise, reflected signals (S_{11}) can be helpful in diagnosing problems with the IDTs. The following scattering parameters were measured as assurance

that the device is working. Figure 3.13 indicates that the reflection parameters are functioning fine and permits a move forward to further characterization of the hybrid device.

After establishing the scattering parameters, the acoustoelectric properties in the hybrid device were measured. The first measurement is of short-circuit (V_{SD} = 0) acoustoelectric current in a two-probe configuration as a function of an RF signal of varying frequency and power P_{RF} applied to each of the two IDTs. For a forward propagating SAW excited by constant P_{RF}, the acoustoelectric current exhibits a characteristic frequency-dependence. This dependence faithfully reproduces the scattering parameter S_{21} data depicted in Figure 3.13. As the propagation direction of the SAW is reversed, the polarity of the acoustoelectric current reverses. This finding indicates that the propagation direction of the SAW determines the direction of the carrier flow between the two contacts (that is, momentum transfer between the SAW and the mobile carriers in the MoS_2 film). The observed polarities provide an independent verification of n-type majority charge carriers in the MoS_2 film and are visible in Figure 3.14.

It is noted that the different acoustoelectric current levels measured for the two IDTs at constant P_{RF} arise from a combination of variations in their absolute conversion efficiencies, distances from the location of the measurements, and SAW attenuation along the propagation path. The lower amplitudes of the acoustoelectric current compared with reports on graphene on $LiNbO_3$ are expected due to the lower carrier concentrations in the MoS_2 films compared to zero-bandgap graphene [3.17, 3.18].

The frequency dependence is followed by a demonstration of the P_{RF} power dependence of the acoustoelectric effect for both SAW directions in a complementary experiment, which measured the open-circuit voltage in a four-point configuration with open connection to the back contact. Here, the total current between the two outer contacts was set to I_{SD} = 0, and the acoustoelectric voltage was picked up between the two inner contacts. In the left panel of Figure 3.15, the measured acoustoelectric voltage is plotted as a function of P_{RF} (in mW) applied for a forward (black). The right panel plots the reverse (red) propagating SAW. The expected linear power dependence of the acoustoelectric effect is observed. As

evident, when the power reaches 150 mW in the forward direction, a positive acoustoelectric voltage value of 16 mV is attained. Alternatively, the opposing direction amounts to a negative value of –5.5 V.

A stronger understanding of the outcomes of the experiment was obtained by measuring the P_{RF} power dependence of the acoustoelectric effect for both SAW directions in a complementary experiment. This experiment measured the short-circuit current in a two-point configuration where the voltage was set to zero. This allowed for measurement of the acoustoelectric current. In Figure 3.16, the acoustoelectric current flows through the contacts as a function of P_{RF} (in dBm). The polarity further provides evidence that the material is n-type if a negative acoustoelectric current is visible and starting to accumulate in the forward direction. A negative acoustoelectric current (black) starts to increase as the P_{RF} to reach a value of -165 nA at 20 dBm. It is noted that the acoustoelectric current and acoustoelectric voltage represent sound-driven constant current and voltage sources, respectively. The SAW remotely drives such an acoustic battery.

3.4 Conclusion

In conclusion, the direct growth of single-layer MoS_2 onto the 128°YX-cut of $LiNbO_3$ permits acoustoelectric spectroscopy on the TMD overlayer, as validated by the hybrid device assembled in this work. This finding opens many new avenues of research. While the hybrid device relied on metal contacts to the TMD film so as to validate congruence between electric transport measurements, subsequent experiments may dispense with the contacts, such as with acousto-mechanically driven approaches, since it ensures close coupling of the SAW to the film. This study highlights that the device fabrication exclusively used scalable techniques to avoid transfer or exfoliation steps. This indicates a move towards the incorporation of TMD films, such as optically-active elements, into conventional and inexpensive $LiNbO_3$-based SAW devices of a type similar to those currently in use, such as frequency filters in cell phones. Consequently, it is anticipated that the fundamental device concept introduced in this article will attain widespread application both in

the fundamental study of properties of TMD films and in the technological realm, where optically-active, thin, inorganic, and durable films are desired. The SAW device in this study remained functional for nine months in air, withstanding multiple intermittent thermal cycles of heating to temperatures as high as 450 K and cooling to as low as 10 K in a vacuum in the meantime. Measurements on different TMD materials indicate promising initial results upon which the next chapter reports.

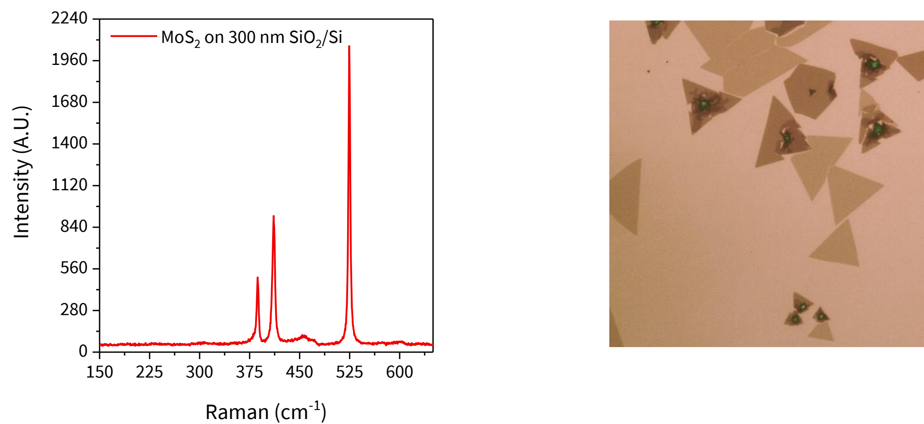

Figure 3.1 | Raman spectrum of single-layer MoS_2: The vibration modes E^1_{2g} at 385 cm^{-1} and A_{1g} at 403 cm^{-1} and give rise to a frequency difference of 18 cm^{-1}. The right panel is an optical image of single-layer MoS_2 on a silicon substrate with a thermal oxide of 300 nm

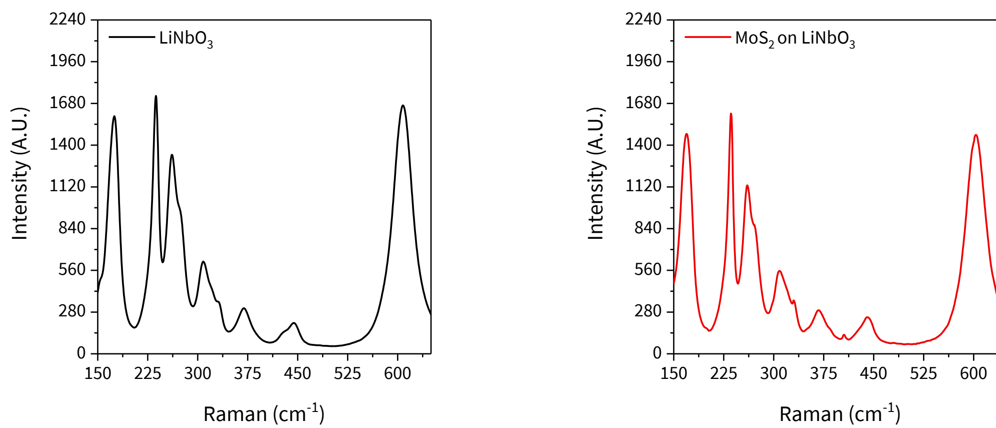

Figure 3.2 | Raman spectrum prior to the growth of single-layer MoS_2 on $LiNbO_3$ (left) and post growth (right). The vibration modes in $LiNbO_3$ saturate the vibration modes from MoS_2, but a small hump gives indication that single-layer MoS_2 is present at 403 cm^{-1}

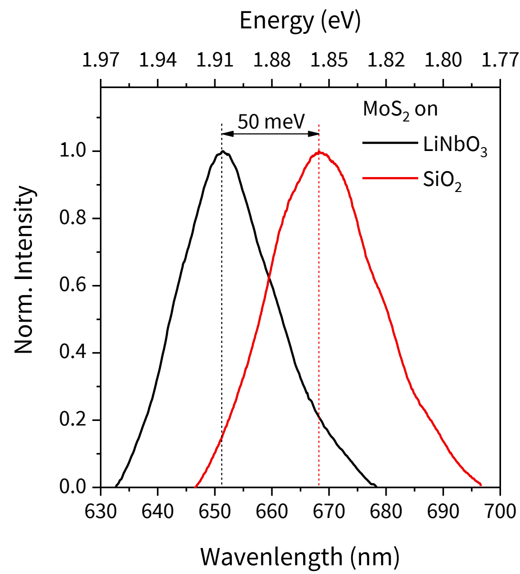

Figure 3.3 | PL spectrum comparison of single-layer MoS_2: The following is the PL spectrum of single-layer MoS_2 on $LiNbO_3$ (black) and on a 300 nm thermally grown oxide silicon substrate (red).

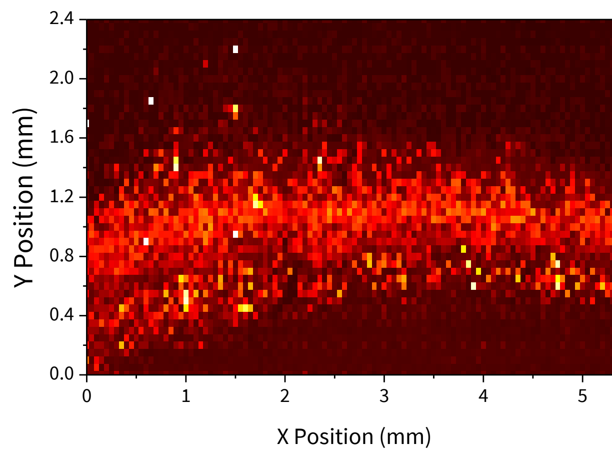

Figure 3.4 | Spatial PL map of MoS_2: The spatial PL map is used as a reference to locate the area of highest emission of single-layer MoS_2

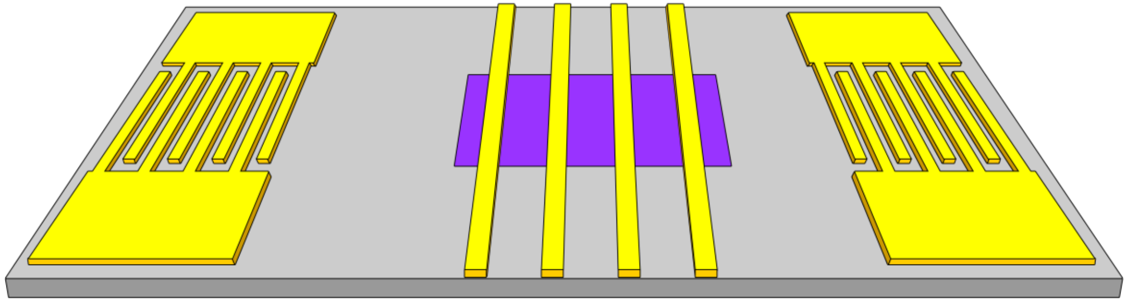

Figure 3.5 | Hybrid SAW-FET device concept: Four Ti/Au contacts form the contacts of a FET fabricated on CVD-grown TMDs. The opposing two, non-impedance matched IDTs are used to excite SAWs propagating across the TMD FET

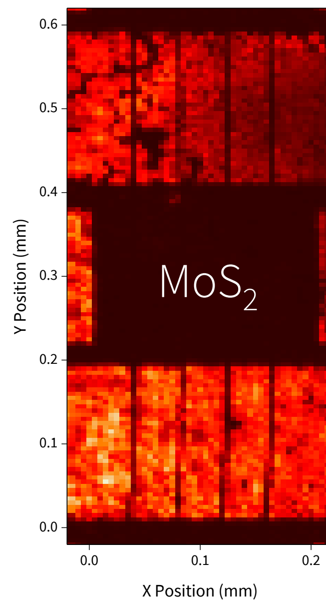

Figure 3.6 | Spatial PL map post fabrication of MoS_2-based hybrid device

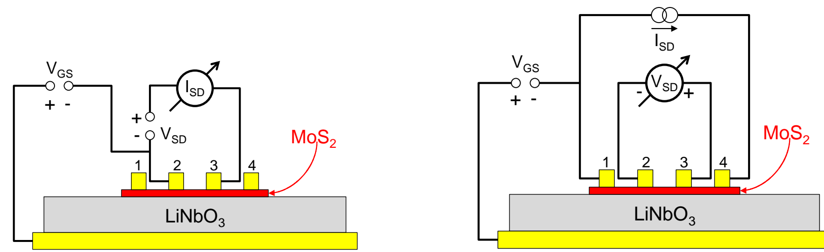

Figure 3.7 | Electrical wiring configuration: Two-point (left) and four-point (right) configuration

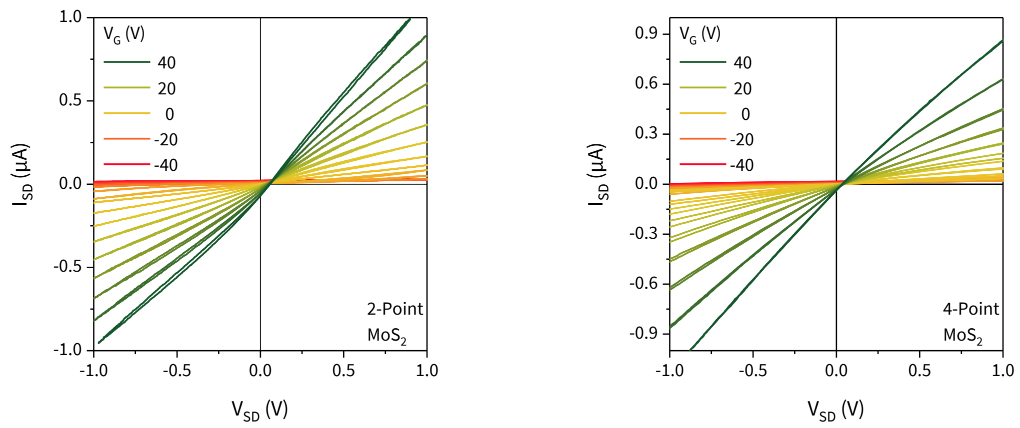

Figure 3.8 | Single-layer MoS_2 output characteristics: I_{SD} versus V_{SD} for different V_G recorded in a two-point (left) and four-point (right) configuration. For large negative V_G, the device is weakly conducting: an n-type channel is formed for positive V_G

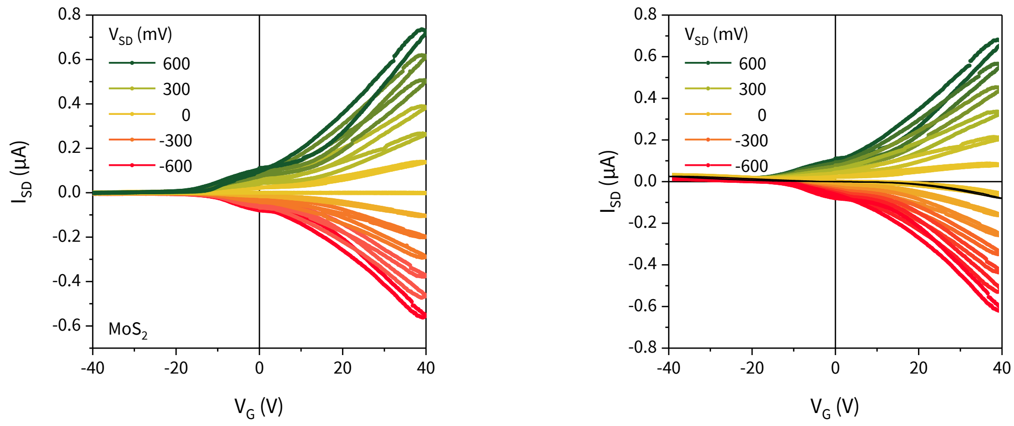

Figure 3.9 | Single-layer MoS_2 transfer characteristics: Left) I_{SD} versus V_G for different V_{SD} recorded in two-point configuration shows pronounced I_{SD} at positive V_G due to formation of an n-type channel. Right) Uncorrected FET transfer characteristics for different V_{SD} (colored) and gate leakage (black). The gate leakage current is weighted by a factor of 2.4 and subtracted from all characteristics. This procedure yields vanishing I_{SD} (V_G) ~ 0 for V_{SD} = 0.

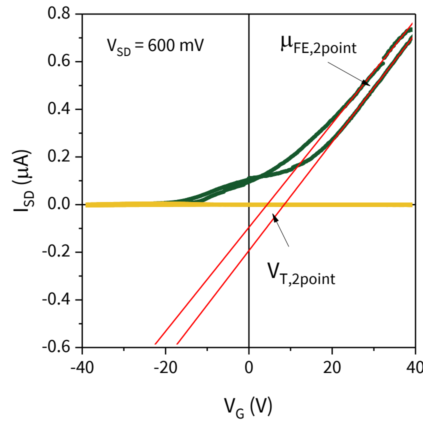

Figure 3.10 | Example of V_{th} analysis: From the transfer characteristics, we are able to extract two values for the up and down direction for field-effect mobility (μ_{FE}) and threshold voltage (V_{th}) due to the hysteric nature of the device.

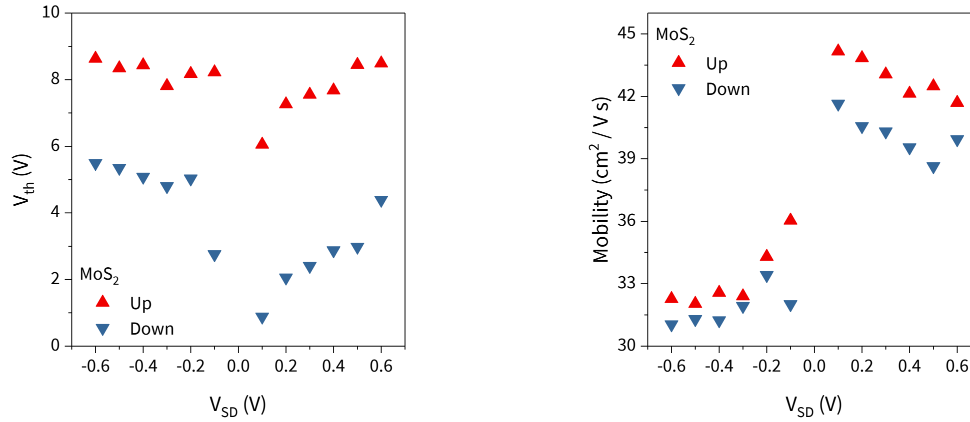

Figure 3.11 | Up and down sweep due to hysteric nature: Left) Threshold voltage (V_{th}) obtained from the up (red triangle) and down (blue triangle) sweep of the transfer characteristics as a function of V_{SD}. Right) Field-effect mobility (μ_{FE}) obtained from the slope of the output characteristics for up (red triangle) and down sweep (blue triangle), respectively.

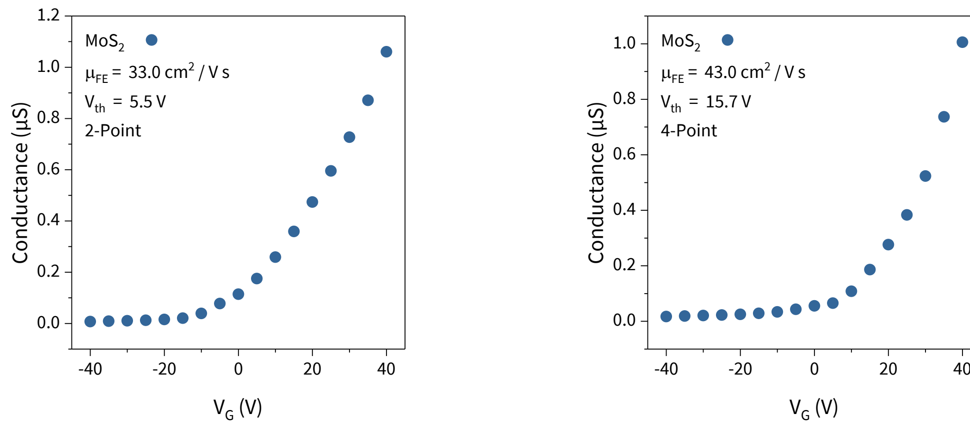

Figure 3.12 | Single-layer MoS_2 conductance linear extraction: Comparison of channel conductance derived for two-point (left) and four-point (right) data. The μ_{FE} for two-point and four-point measurements are 33 cm^2 / V s and 43 cm^2 / V s, respectively. The V_{th} voltage of 5.5 V (two-point) exceeds the derived two-point measurement of 15.7 V by a factor of 5 because of the three-fold increase total channel length.

Table 3.1 | FET mobility (μ_{FE}) and threshold voltage (V_{th}) determined by different techniques

	4-Point Output $V_{SD} = 0$	2-Point Output $V_{SD} = 0$	2-Point Transfer
μ_{FE} (cm^2 / V s)	43 ± 5	33 ± 5	37 ± 5
V_{th} (V)	5.2 ± 1.5	5.5 ± 1.5	5.8 ± 2.5

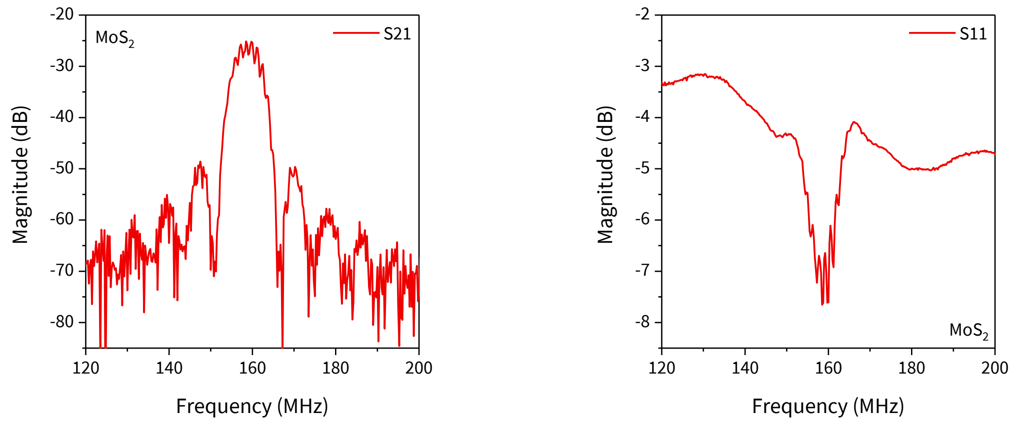

Figure 3.13 | Scattering parameters of single-layer MoS_2 hybrid device: Left) Transmission parameter (S_{21}) is measured as a function of frequency. Right) Reflection parameter (S_{11}) is functioning and no visible damage is apparent with the signal

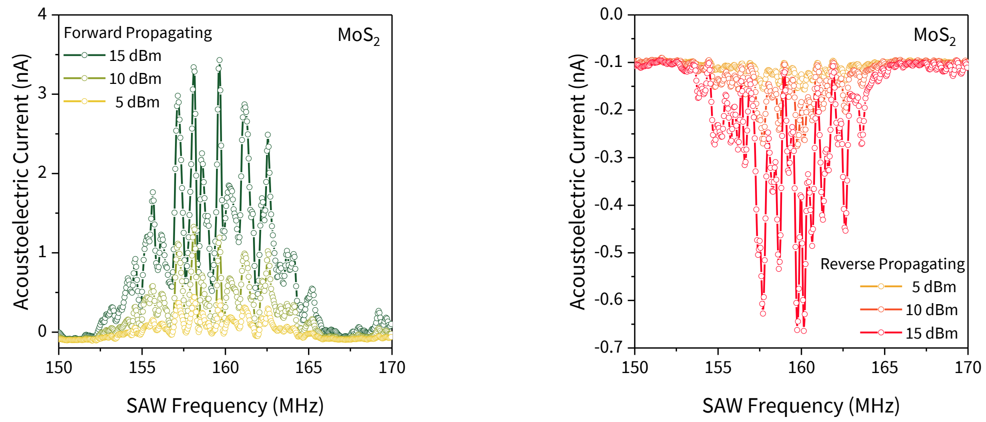

Figure 3.14 | Acoustoelectric current as a function of RF signal applied to the IDTs for different RF power levels: Current measurements were performed in a two-point short-circuit (V_{SD} = 0) configuration. The forward direction (left) yields positive sign and reverse direction (right) yields negative sign

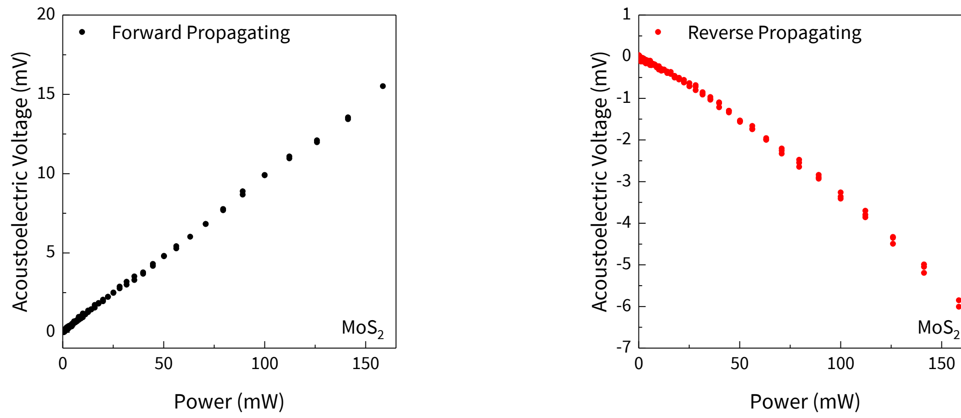

Figure 3.15 | Acoustoelectric voltage as a function of P_{RF} (mW): Measurements were done in a two-point, open circuit configuration (I_{SD} = 0). For the forward (left) and reverse (right) SAW propagation direction, the expected linear dependence is well reproduced

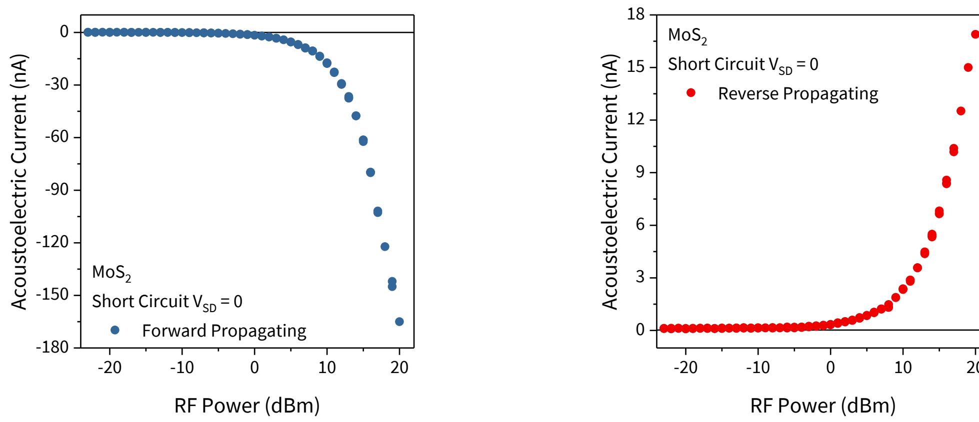

Figure 3.16 | Acoustoelectric current as a function of RF power (dBm): The negative acoustoelectric current forms in the forward propagating direction. This type of behavior corresponds to n-type conductivity of the film and is expected for single-layer MoS_2

3.5 References

[3.01] Mann, J., et al. (2013). "Facile growth of monolayer MoS2 film areas on SiO2." The European Physical Journal B **86**(5).

[3.02] Schaufele, R. F. and M. J. Weber (1966). "Raman Scattering by Lithium Niobate." Physical Review **152**(2): 705-708.

[3.03] Pignatiello, F., et al. (2007). "Measurement of the thermal expansion coefficients of ferroelectric crystals by a moiré interferometer." Optics Communications **277**(1): 14-18.

[3.04] Okada, Y. and Y. Tokumaru (1984). "Precise determination of lattice parameter and thermal expansion coefficient of silicon between 300 and 1500 K." Journal of Applied Physics **56**(2): 314-320.

[3.05] He, K., et al. (2013). "Experimental demonstration of continuous electronic structure tuning via strain in atomically thin MoS2." Nano Lett **13**(6): 2931-2936.

[3.06] Hui, Y. Y., et al. (2013). "Exceptional Tunability of Band Energy in a Compressively Strained Trilayer MoS2Sheet." ACS Nano **7**(8): 7126-7131.

[3.07] Bordui, P. F., et al. (1999). "Chemically reduced lithium niobate single crystals: Processing, properties and improved surface acoustic wave device fabrication and performance." Journal of Applied Physics **85**(7): 3766-3769.

[3.08] Wilson, W. and G. Atkinson (2006). "Mixed Modeling of a SAW Delay Line using VHDL." 34-39.

[3.10] Mak, K. F., et al. (2010). "Atomically thin MoS(2): a new direct-gap semiconductor." Phys Rev Lett **105**(13): 136805.

[3.11] Radisavljevic, B., et al. (2011). "Single-layer MoS2 transistors." Nat Nanotechnol **6**(3): 147-150.

[3.12] Ghatak, S., et al. (2011). "Nature of electronic states in atomically thin MoS(2) field-effect transistors." ACS Nano **5**(10): 7707-7712.

[3.13] Late, D. J., et al. (2012). "Hysteresis in single-layer MoS2 field effect transistors." ACS Nano **6**(6): 5635-5641.

[3.14] Bao, W., et al. (2013). "High mobility ambipolar MoS2 field-effect transistors: Substrate and dielectric effects." Applied Physics Letters **102**(4): 042104.

[3.15] Lee, K., et al. (2013). "High-performance sensors based on molybdenum disulfide thin films." Adv Mater **25**(46): 6699-6702.

[3.16] Wong, H.-S., et al. (1987). "Modeling of transconductance degradation and extraction of threshold voltage in thin oxide MOSFET's." Solid-State Electronics **30**(9): 953-968.

[3.17] Radisavljevic, B. and A. Kis (2013). "Mobility engineering and a metal-insulator transition in monolayer MoS(2)." Nat Mater **12**(9): 815-820.

[3.18] Miseikis, V., et al. (2012). "Acoustically induced current flow in graphene." Applied Physics Letters **100**(13): 133105.

[3.19] Bandhu, L., et al. (2013). "Macroscopic acoustoelectric charge transport in graphene." Applied Physics Letters **103**(13): 133101.

[3.20] Preciado, E., et al. (2015). "Scalable fabrication of a hybrid field-effect and acousto-electric device by direct growth of monolayer MoS2/LiNbO3." Nat Commun **6**: 8593.

4 Hybrid SAW-FET WSe_2

4.1 Introduction

Two-dimensional materials, such as graphene, offer new opportunities in the field of electronics. However, they lack a direct bandgap and therefore limit potential applications. Alternatively, TMDs provide a direct bandgap in the visible and near-infrared range. Interestingly, most investigations of TMDs have focused on conventional semiconductor platforms, typically applied for functional FET devices [4.01], gas sensing [4.02], extended to ferroelectric gating [4.03], and were used to construct a memory element [4.04]. Among them, WSe_2 is highly appealing, as it exhibits p-type behavior with reported mobility values of 140 cm^2 / V s and on/off ratios of ~10^7 [4.05]. A range of CVD-based growth methods has been developed for WSe_2 films on various substrates, but rarely on $LiNbO_3$. $LiNbO_3$ is routinely used in numerous commercial SAW devices, ranging from RF filters to wirelessly-interrogated and identity-tagged devices [4.06]. In addition, $LiNbO_3$ is the material of choice for integrated photonic devices that harness its native nonlinear optical properties for classical and quantum communication. Hence, the hybridization of single-layer WSe_2 with 128°YX-cut $LiNbO_3$ is a key technological advancement. This chapter demonstrates a fully-functional hybrid device. Millimeter-scale CVD growth of single-layer WSe_2 onto piezoelectric 128°YX-cut $LiNbO_3$ is achieved. Field-effect transistors fabricated on these films exhibit p-type behavior and hole mobilities that are competitive with WSe_2 devices established on silicon. Acoustoelectric effects in single-layer WSe_2 induced by a

propagating SAW were observed and the expected dependence on applied RF and power were investigated.

4.2 Experimental Methods

The following section summarizes the growth process and instruments necessary to identify single-layer WSe_2. In particular, single-layer WSe_2 films were CVD grown on two substrates. Raman spectroscopy and PL measured the vibration modes and emission intensity, respectively. These reliable and non-destructive techniques were used to investigate the single-layer nature of WSe_2.

4.2.1 Sample Preparation of Single-Layer WSe_2

Single-layer WSe_2 films were deposited on 128°YX-$LiNbO_3$ and SiO_2/Si substrates using a CVD process operating at atmospheric pressure. Initially, the substrates were cleaned to obtain a smooth surface that was free of residual contaminants. It should be noted that single-layer WSe_2 films were grown in separate runs under identical process conditions for each substrate. A typical setup is composed of tungsten and selenium sources that serve as precursors. Using this approach, the substrate was placed polish-side down in a tungsten mesh holder on an alumina crucible that was filled with 32 mg of high purity $W(CO)_6$ powder at the center of the single zone furnace. Meanwhile, a separate alumina crucible with 33 mg of Se powder was placed upstream with respect to the gas flow in the furnace. The distance between two sources was optimized at a distance of 20 cm for maximum film coverage. The 1-inch diameter quartz tube was first displaced by 3 inches upstream and then purged for 20 minutes at 400 °C under 1 SCFH argon flow rate in order to create an inert atmosphere. When the desired temperature was achieved, CO_2 with a gas flow rate of 0.2 SCFH was introduced into the quartz tube and the argon gas flow rate was reduced to 0.5 SCFH. The furnace was then ramped for 30 minutes to reach a center zone temperature of 750 °C at a ramp rate of 8.3

°C/min. During the synthesis process, the flow rates of argon and CO_2 were both decreased to 0.1 SCFH. At this point, the quartz tube was pushed 3 inches downstream to position the $W(CO)_6$ and Se to a set temperature of 750 °C and 250 °C, respectively. These temperatures were maintained for 10 minutes. After finishing growth, the furnace was decreased to 600 °C for 20 minutes under argon, CO_2, and H_2, with gas flow rates of 0.3, 0.1, and 0.1 SCFH, respectively. The use of hydrogen was introduced in the CVD process to reduce the $W(CO)_6$ and allow for WSe_2 growth, consistent with recent literature [4.20, 4.24-25]. Shortly after, the furnace was set to 500 °C for 10 minutes, and the hydrogen flow rate was turned off. Finally, the power was shut down to naturally cool the quartz tube to room temperature under 0.3 SCHF argon flow rate.

4.2.2 Raman Characterization of Single-Layer WSe_2

Raman spectroscopy was performed to gain insight into the quality of single-layer WSe_2. In particular, Raman spectroscopy has been extensively used to identify the vibration modes present in WSe_2. Single-layer WSe_2 was nominally grown onto 128°YX-$LiNbO_3$ or SiO_2/Si substrates. The latter consisted of silicon with a 300 nm thermally-grown oxide layer. The 300 nm SiO_2/Si substrate served as a reference to compare with the $LiNbO_3$ substrate. Figure 4.1 shows two peaks to the left of the silicon peak at 520 cm^{-1} measured in the range between 150 cm^{-1} and 550 cm^{-1}. In numerous studies available on Raman spectroscopy of WSe_2, the leftmost peak was identified as the E^1_{2g} in-plane mode and the broad feature at its right as the A_{1g} out-of-plane mode. As the layers decrease in thickness, the prominent E^1_{2g} and A_{1g} modes degenerate and a broad 2LA(M) phonon peak appears [4.07]. The resulting 2LA(M) resonance peak is a second-order Raman mode due to longitudinal acoustic phonons at the M point of the Brillouin zone [4.08]. Experimentally, prominent peak values of 249 cm^{-1} and 260 cm^{-1} were obtained for E^1_{2g} and A_{1g} mode and 2LA(M) mode, respectively. The sharp peak and full width at half maximum for the E^1_{2g} and A_{1g} mode was 3 cm^{-1}, which indicates a high degree of crystallinity and good agreement with previous studies [4.07, 4.9-11].

To corroborate this interpretation, Raman measurements on blank $LiNbO_3$ and WSe_2 on $LiNbO_3$ substrates were also performed. The left panel of Figure 4.2 reveals that many vibrations modes were present on the blank 128°YX-$LiNbO_3$ cut substrate prior to growth [4.12]. Evidently, the vibration modes of $LiNbO_3$ overlap with the expected WSe_2 regime. The WSe_2 signal was hampered due to the dominant $LiNbO_3$ signal, as depicted on the right panel of Figure 4.2.

4.2.3 PL Characterization of Single-Layer WSe_2

The optical properties of single-layer WSe_2 were measured using PL spectroscopy. In the case of single-layer WSe_2, the pronounced increase of the PL intensity is attributed to the formation of a direct bandgap. Figure 4.3 presents resultant normalized PL spectra for single-layer WSe_2 grown under identical conditions on $LiNbO_3$ (black) and SiO_2/Si (blue) over the spectral range of 1.52 – 1.78 eV. A PL peak is clearly resolved for both samples, indicating the single-layer nature of WSe_2. It was further noted that emission peak responses differ significantly for SiO_2/Si compared to that of 128°YX-cut $LiNbO_3$. In the former case, a single-emission peak was indicated at photon energy of 1.65 eV, in agreement with recent reports [4.13-15,18-19]. On the other hand, for 128°YX-cut $LiNbO_3$, the single-emission peak was identified at 1.63 eV photon energy larger by 20 meV. This shift may arise from the thermal expansion of the crystal, which was ascribed to a five-fold difference in the thermal expansion coefficient of $LiNbO_3$ (12.6×10^{-6} K^{-1}) [4.16] compared to that of Si (2.6×10^{-6} K^{-1}) [4.17] near room temperature. In a similar manner to the MoS_2 hybrid device, compressive strain during the cool-down growth process of WSe_2 is attributed to a blue shift of the PL emission. Another possibility may be related to the formation of Se vacancies, which is fairly common for CVD-grown TMDs with non-uniform PL [4.18-19].

As seen in Figure 4.4, spatial PL mapping can allow for the analysis of different areas of a substrate in order to identify single-layer WSe_2. In Figure 4.4, the resultant PL map corresponds to the optical quality of single-layer WSe_2, where a focused laser with an excitation wavelength of 520 nm was stepped in 1 µm increments

along the sample, and PL spectra were recorded at each point. The PL intensity is encoded in a color scale, with red and dark regions corresponding to high and low intensity counts, respectively. The FET channels were placed within the region of highest intensity, and IDTs were placed on opposite ends of the substrate. It should be noted that intensity differences are likely the result of variations in film domain size [4.18].

4.2.4 Lithographic Patterning

Electron-beam lithography was selected for the fabrication of contacts (L = 35 µm, W = 360 µm) and IDTs (spilt-2 design, 21 finger pairs, duty cycle 1:1, 200 µm aperture, 5.4 mm delay path) for electrical and acoustic interfacing to WSe_2 film, respectively. In the case of WSe_2, the spatial PL map demonstrated in Figure 4.4 determined the extent of single-layer film and allowed for the preparation of lithographically-defined structures. The as-grown sample was cleaned by sonication using acetone for 5 minutes and rinsed in isopropanol. After drying with a nitrogen gun, the sample was baked for approximately 2 minutes at 190 °C. The PMMA films were prepared using a bi-layer method, where the lower layer (PMMA 150K MW, 4%) was exposed more rapidly than the upper layer (PMMA 500K MW, 2%) due to its higher sensitivity. The e-beam resist was baked on a hot plate for 90 seconds at 190 °C to drive off solvents and solidify. E-beam exposure proceeded with an acceleration voltage of 10 kV and area dose of 100 µA / cm^2, followed by development in MIBK:IPA (1:5) for 30 seconds and IPA for 15 seconds. Remaining PMMA residuals in the exposed vicinity were removed with light oxygen plasma. Subsequent deposition of 10 nm Ti followed by 60 nm Au was performed in an e-beam evaporator. Lift-off was done immediately after metal deposition. It should be noted that a portion of the WSe_2 film was selectively removed in a second lithographic step in order to avoid any electrical shorts in the system. Etching was completed with an oxygen plasma treatment (200 W, 500 mTorr, 13 s) and remaining resist was washed off with acetone at 60 °C.

4.2.5 Measurement Techniques

Optical characterization was performed on the Horiba LabRAM HR spectroscopy system using a 532 nm wavelength excitation laser. Raman and PL were performed on 1,800 and 600 lines per mm grating, respectively. Spatial PL maps were measured using a 520 nm wavelength excitation laser. Electrical characterization for a two-point configuration was measured using the Keithley 2400 SMU, whereas for a four-point configuration, the Keithley 2400 was used only as a constant current source (no measurement probes connected) and voltages at the potential probes were recorded directly by a Keithley 2000 digital multimeter. Bias voltages and leakage currents were applied and measured simultaneously by a Keithley 2600 SMU, respectively. Surface acoustic wave spectroscopy was performed with RF signal generator model SG382 from Stanford Research Systems and operated in conjunction with an amplifier in order to deliver high-frequency SAWs, which were then launched from an input IDT and detected from an output IDT. Short-circuit acoustoelectric currents and open-circuit acoustoelectric voltages were recorded using a K2400 SMU with V_{SD} = 0 and I_{SD} = 0, respectively. Radio frequency characteristics of the IDTs and SAW scattering parameters were characterized using a vector network analyzer.

4.3 Experimental Results

This section summarizes the use of SAWs and FETs to investigate the acoustoelectric and electric transport properties of single-layer WSe_2, respectively. The SAW and FET experiments were performed on the WSe_2 hybrid device, which consists of two components: (i) SAW delay line formed by a pair of IDTs located at opposite ends of the substrate in a delay line configuration of 5.4 mm and (ii) single-layer WSe_2 FET between the two IDTs. The fundamental frequency of operation of the SAW was designed for 160 MHz, corresponding to a design wavelength of 25 µm. Surface acoustic waves propagating at a velocity of 3,980 m s^{-1} were launched and detected across the substrate via input and output IDTs, respectively. It is to

be noted that the hybrid device maintained the same layout as the MoS_2 hybrid device to ensure reproducibility. A micrograph of a portion of the hybrid device is visible below in Figure 4.5.

4.3.1 Post Spatial PL Map of Single-Layer WSe_2

Post-spatial PL mapping was performed after etching the outside region of the WSe_2 FET channel and propagation path. PMMA served as a mask to protect WSe_2 during the etching process (Figure 4.5). In Figure 4.6, the post-spatial PL map is encoded with red and dark regions corresponding to high and low intensity count rates, respectively. Evidently, the high PL emission remains intact on the WSe_2 channel to confirm successful etching.

4.3.2 FET Characterization of Single-Layer WSe_2

In this study, WSe_2 channels were tested to determine FET operation of the hybrid device by measurement of its transport characteristics as a function of back gate voltage (V_G) across the $LiNbO_3$ substrate. Notably, the dielectric constant associated with $LiNbO_3$ (ε_r ~ 50) is much larger compared to SiO_2 (ε_r ~ 3.9). As a result, moderate electric fields of ± 40 kV/cm can be achieved by applying a gate voltage V_G = ± 40 V between the $LiNbO_3$ backside and the WSe_2 layer. Figure 4.5 presents a schematic illustration of the transistor structure and its electrical wiring configuration. From recent studies, but in contrast with ref [4.13, 4.20-21], WSe_2 is expected to show p-type behavior on a silicon-based platform [4.18, 4.22-23]. Therefore, the hybrid device is expected to only exhibit sizable currents for negative gate voltages.

Output measurements of the WSe_2 hybrid device were measured in ambient conditions. The left panel on Figure 4.7 depicts the current flowing through the source-drain current (I_{SD}) contacts as a function of the source-drain voltage (V_{SD}) from – 1 V to 1 V in 5 mV steps in a two-point configuration. Different back gate voltages (V_G) ranging from V_G = – 40 V to + 40 V with a waiting time of 10 seconds per 10 V_G step were applied.

As the V_G turns from positive to negative polarity, a substantial increase of current is observed. A formation of a p-type channel forms with negative V_G values, where I_{SD} reaches 500 nA at V_{SD} = 1.0 V for V_G = – 40 V. Therefore, the reduction of sheet resistance is due to the accumulation of holes in WSe_2, as evidenced in literature [4.22, 4.23].

The right panel of Figure 4.7 displays the transfer characteristics of the WSe_2 FET. The I_{SD} was measured as a function of V_G and recorded in a two-point configuration for varying V_{SD} ranging from – 400 mV to + 400 mV in 100 mV increments, current limited to 4 µA compliance. The V_G is swept from + 40 V to – 40 V (up sweep) and back from – 40 V to + 40 V (down sweep), with a waiting time of 1.6 seconds per 0.5 V_G step. No significant current was observed for large positive bias or indication of ambipolar behavior. However, the channel allows sizeable I_{SD} to form for negative V_G. The highest I_{SD} measured was 300 nA for a V_{SD} = 400 mV at – 40 V_G. The I_{SD} increased when V_G was negative, which was consistent with the behavior of p-type material and hole conductivity found in solid-state devices. It is to be noted that the measured currents were corrected to minimize the influence of the gate current (I_G):

$$I_{SD\ Corrected} = I_{SD\ Measured} + 0.38\ (I_G) \qquad \text{Equation 4.1}$$

The factor for I_G was determined so that I_{SD} (V_G) for V_{SD} ~ 0 V was as close to zero as possible. Subsequently, the small leakage currents were weighted by a factor of 0.38 and subtracted from all characteristics. The minor leakage did not affect the overall I_{SD} signal.

In this section, the threshold voltage (V_{th}) and field-effect mobility (μ_{FE}) were extracted from the transfer characteristics. In order to determine V_{th}, it is customary to apply a tangent to the linear region of the transfer curve. Here, the slope of tangent (dI_{SD} / V_G) and x-intercept (V_{th}) were each extracted at constant V_{SD}. However, due to the hysteric nature of the transfer curve, two sets of values were obtained when extracting the slope and x-intercept (Figure 4.8). The first set corresponds to sweep in the up direction (V_G = + 40 V to – 40 V) and the second set to the sweep in the down direction (V_G = – 40 V to + 40 V). It is noted that charges

could be trapped at the interface of $LiNbO_3$ and WSe_2 due to V_G stress during the sweep. As a result of the small hysteresis, a positive or negative shift for the Vth was observed [4.23]. Alternatively, hysteresis may arise from adsorption and desorption of impinging gas atoms and molecules, such as oxygen and moisture at the $LiNbO_3/WSe_2$ interface, acting as charge trap sites [4.02, 4.26-27].

The field-effect mobility (μ_{FE}) was extracted through the equation:

$$\mu_{FE} = \frac{L}{W} \frac{d_{substrate}}{\varepsilon_r \varepsilon_0} \frac{1}{V_{SD}} \frac{dI_{SD}}{dV_G} \qquad \text{Equation 4.2}$$

Here, L is the distance between source and drain contacts, W is the width of the channel, $d_{substrate}$ = 500 µm denotes the thickness of the $LiNbO_3$ substrate, ε_0 is permittivity of free space, ε_r = 50.1 is the relative permittivity of the $LiNbO_3$, and V_{SD} is the constant source-drain voltage. The μ_{FE} was plotted on the left panel of Figure 4.9.

The right panel of Figure 4.9 depicts the channel conductance extracted from the two-point output curve evaluated at V_{SD} = 0 and plotted as a function V_G. A linear fit on the conductance curve determined the μ_{FE} and V_{th} from the slope and from the intersection at I_{SD} = 0, respectively. Based on the slope value, a μ_{FE} of 14.5 cm^2 / V s with a V_{th} of – 5.5 V in a two-point configuration was extracted.

4.3.3 Acoustoelectric Characterization of Single-Layer WSe_2

Surface acoustic wave spectroscopy was used to validate the acoustoelectric properties of the WSe_2 hybrid device. To characterize the SAW modes, the reflection (S_{11}) and transmission (S_{21}) parameters of the IDT were measured with a vector network analyzer. Figure 4.10 presents the magnitude of transmission parameter in decibels as a function of RF signal for the WSe_2 SAW device. In this spectrum, the expected resonance frequency (f_{SAW}) of 160 MHz, which corresponded to a SAW wavelength (λ_{SAW}) of 25 µm, was

resolved. The RF characterization demonstrates high-efficiency generation, transmission, and detection of SAWs on the $LiNbO_3$ host substrate, even after its exposure to the WSe_2 growth conditions.

The acoustoelectric current was generated in single-layer WSe_2 by applying a RF signal to each IDT in the range 120-200 MHz, at varying power P_{RF}. Measurements were detected using a SMU in a short-circuit (V_{SD} = 0) configuration between the source/drain electrodes in contact with the WSe_2 region. It is noted that SAWs were launched in a forward and reverse direction by switching IDTs. The left panel of Figure 4.11 displays a positive acoustoelectric current accumulating in a forward-propagating SAW, which exhibits a value of 6 nA at + 15 dBm, and diminishing in magnitude as P_{RF} was lowered. As the propagation direction is reversed, the polarity of the acoustoelectric current switched and detected a value of –2 nA at +15 dBm (right panel of Figure 4.11). In this connection, it is interesting to note the frequency trace between the acoustoelectric current closely resembles the transmission parameter (S_{21}) at 160 MHz (Figure 4.10).

The acoustoelectric voltage was measured between the inner contacts in an open-circuit configuration (I_{SD} = 0 for outer contacts) and was plotted as a function of P_{RF}. Two different schemes of the acoustoelectric voltage of WSe_2 were proposed, as illustrated in Figure 4.12, where the left panel exhibits that SAWs propagating in forward direction were indicating negative polarity. Alternatively, the polarity of the acoustoelectric voltage became positive when the propagation direction was reversed, as plotted on the right panel of Figure 4.12. A negative value of – 11 mV and a positive value of 2.4 mV were obtained for a forward- and reverse-propagating direction, respectively. The observed linear behavior of the acoustoelectric voltage curve of the WSe_2 SAW device in both propagating directions indicates that the trace is in agreement with the acoustoelectric effect [4.28].

It should be indicated that the power dependence was additionally applied in a short-circuit configuration (V_{SD} = 0), where the acoustoelectric current was detected as a function of P_{RF} (dBm) and plotted in Figure 4.13. A positive acoustoelectric current as high as 18.6 nA was measured in a forward-propagating direction at + 20 dBm, whereas a value of – 3.93 nA was measured for a reverse-propagating direction [4.28].

Subsequently, the direction of the propagating SAW confirmed the polarity of the acoustoelectric current and signified hole transport in the single-layer WSe_2 that was indicative of p-type behavior and corroborating transport characteristics in Figure 4.7. Similar results were measured for an n-type based MoS_2 hybrid device [4.29].

4.4 Conclusion

In summary, mm-scale CVD single-layer growth of WSe_2 was achieved directly on piezoelectric $LiNbO_3$. Raman and PL spectroscopy were performed to verify the single layer thickness. Spatial PL mapping identified the area of interest in accordance for the placement of IDTs and contacts for propagating SAWs and electrical transport, respectively. Moreover, electrical transport verified the p-type nature in single-layer WSe_2 and in good agreement with literature. For this particular device, hole mobility values up to 29.5 cm^2 / V s was achieved. FETs fabricated on the sample allowed for the detection and measurement acoustoelectric effect, typically detected when charge carriers from semiconductors surf in the electric field associated with propagating SAWs. Measurements such as the acoustoelectric current as a function of frequency displayed a frequency dependence on the signature frequency response associated with the transmission parameter (S_{21}). Additionally, acoustoelectric current and voltage displayed hole carrier dominant material, displaying a positive current in a forward propagating SAW. These results point out the potential influence SAW spectroscopy can have for future measurements based on single-layer TMDs on a hybrid SAW – FET configuration.

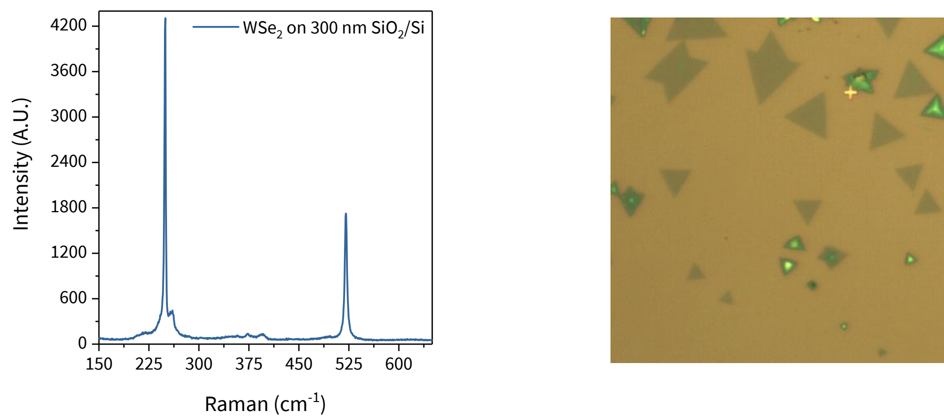

Figure 4.1 | Raman spectrum of single-layer WSe_2: The vibration modes E^1_{2g} at and A_{1g} merge as expected for single-layer WSe_2 at 249 cm^{-1}. The right panel is an optical image of single-layer WSe_2 islands on a silicon substrate with a thermal oxide of 300 nm along with a gold crosshairs.

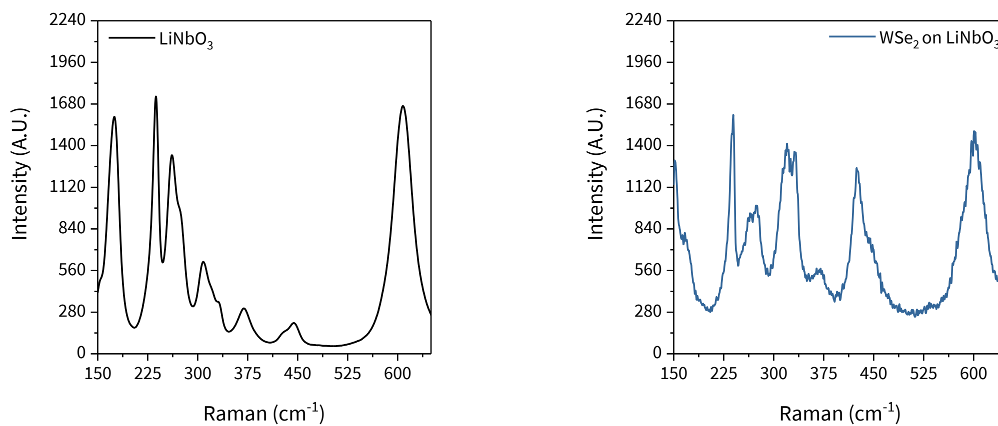

Figure 4.2 | Raman spectrum of prior (left) and post (right) growth of single-layer WSe_2 on $LiNbO_3$. The vibration modes in $LiNbO_3$ saturate the vibration modes of WSe_2

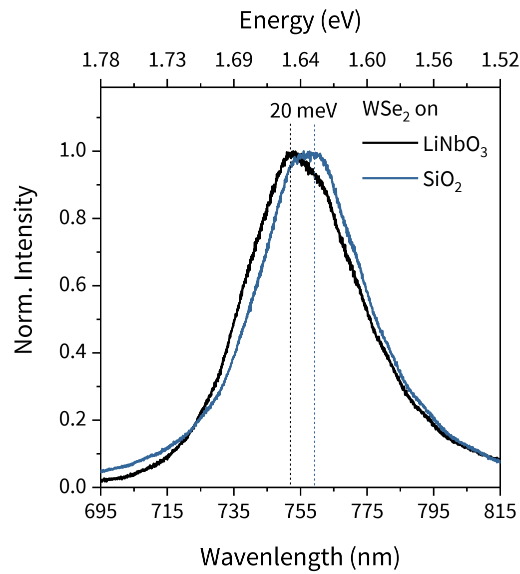

Figure 4.3 | PL characterization of single-layer WSe_2: Comparison of single point normalized PL spectra obtained on SiO_2 (blue) and our 128°YX-cut $LiNbO_3$ substrate (black) reveals a blue shift attributed to the compression of the single-layer WSe_2 film. Similar results were seen on the MoS_2 hybrid device

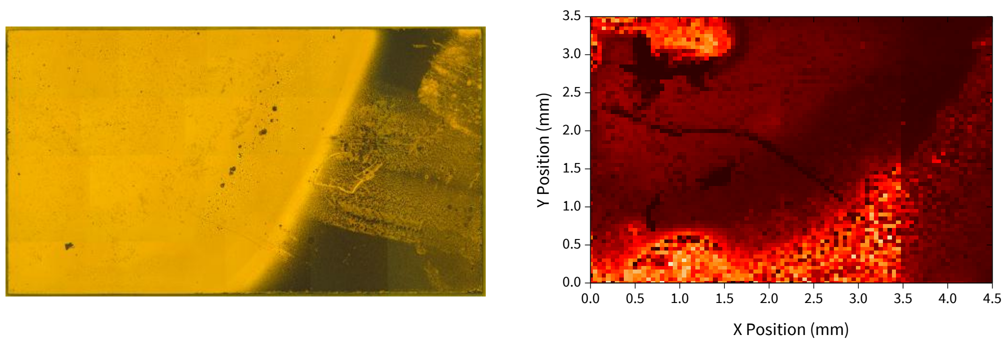

Figure 4.4 | Post growth and spatial PL map of single-layer WSe_2 on $LiNbO_3$: Optical image of CVD-grown single-layer WSe_2 on a $LiNbO_3$ substrate. The rectangle marks the scan region for the spatial PL map of WSe_2. On the right is the PL spatial map. The intensity is color coded with red (dark) correspond to high (low) count rates confirms mm-scale growth. Electrical contacts are placed in the area of highest emission

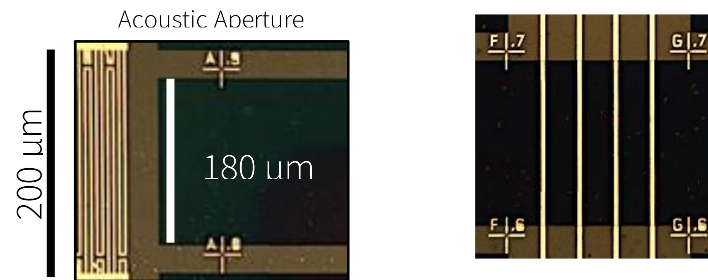

Figure 4.5 | Layout of IDTs: The micrograph shows the double finger (split-2) IDTs used in this study. They have 21 fingers pairs, an aperture of 200 µm, a delay line width of 180 µm and were fabricated 5.4 mm apart. Post single-layer WSe_2 etch: Optical micrograph of our hybrid device covered with resist. The exposed regions are etched with oxygen plasma.

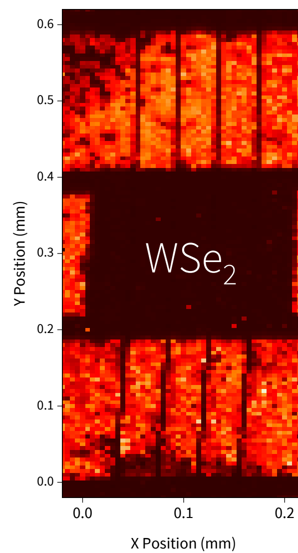

Figure 4.6 | Post fabrication spatial map: High emission is still present after etching to ensure no shortcuts affect transport measurements. Dark areas indicate no material is present while the highest emission is color coded in red

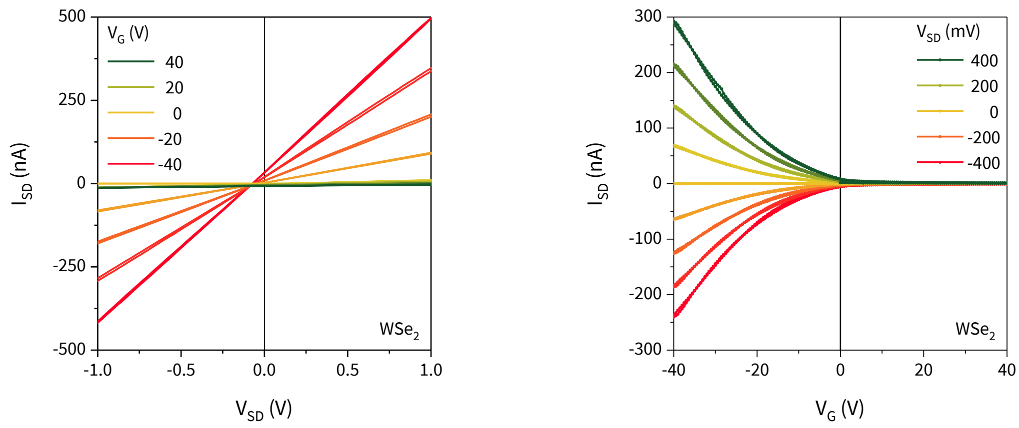

Figure 4.7 | Single-layer WSe_2 output and transfer characteristics: Output curve measured I_{SD} versus V_{SD} for different V_G recorded in a two-point configuration. For large positive V_G, the device is weakly conducting: a p-type channel is formed for negative V_G. Transfer curve on the right panel

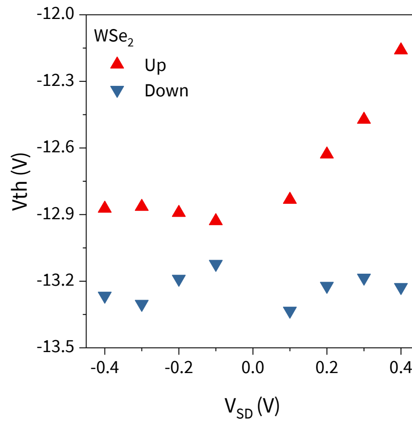

Figure 4.8 | Threshold voltages: Threshold voltages (V_{th}) obtained from the up (up red triangle) and down sweep (down blue triangle) of the transfer characteristics as a function of V_{SD} It is to be noted that V_{th} is simply the V_G at which the FET becomes conductive

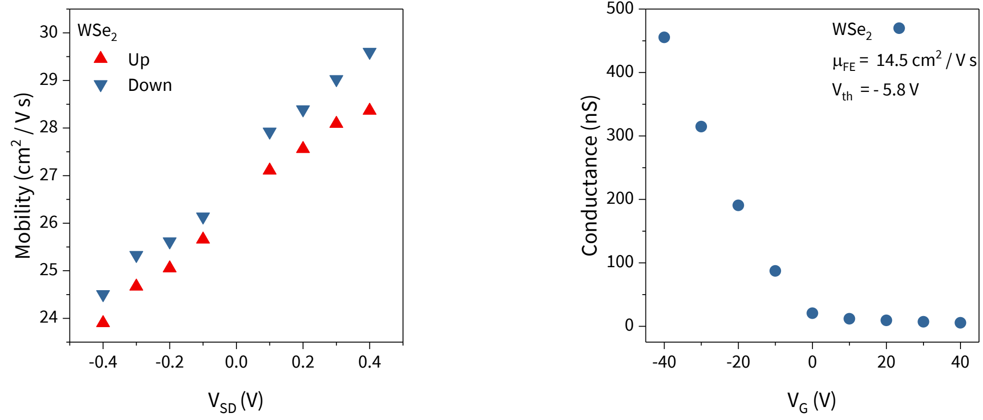

Figure 4.9 | Mobility and conductance of single-layer WSe_2: Field-effect mobility obtained from the slope of the transfer characteristics for up (up red triangle) and down sweep (down blue triangle), respectively. Conductance on the right panel exhibited field-effect mobility (μ_{FE}) of 14.5 cm^2 / V s with a threshold voltage (V_{th}) of – 5.5 V.

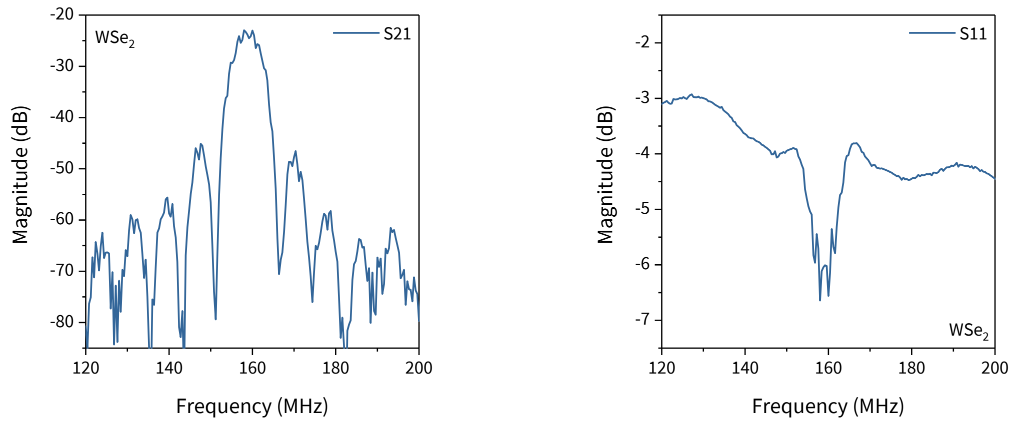

Figure 4.10 | SAW transmission and reflection parameter: Transmission parameter (S_{21}) between the IDTs shows a pronounced maximum at the design frequency f_{SAW} = 160 MHz of the 5.4 mm long delay line. Reflection parameter (S_{11}) is on the right

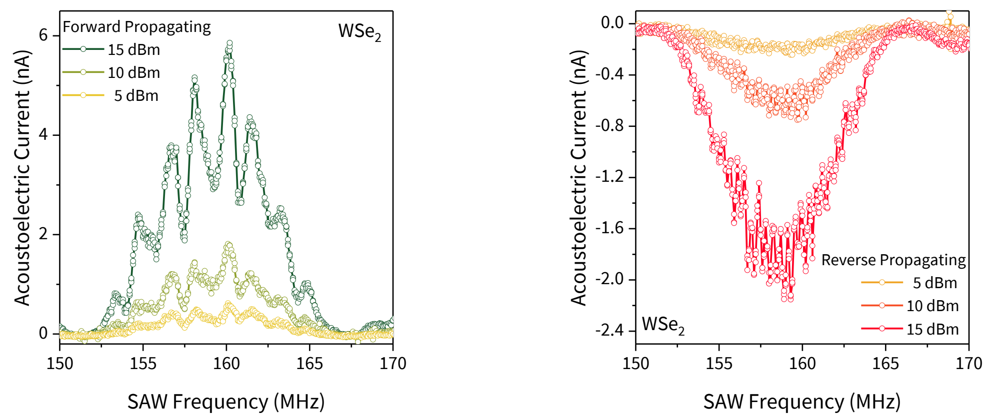

Figure 4.11 | Acoustoelectric frequency dependence: Current measurements were performed in a two-point short-circuit (V_{SD} = 0) configuration. The forward direction (left) yields positive sign and reverse direction (right) yields negative sign. Frequency dependence of the band of the SAW transmission is replicated when applying higher RF power levels.

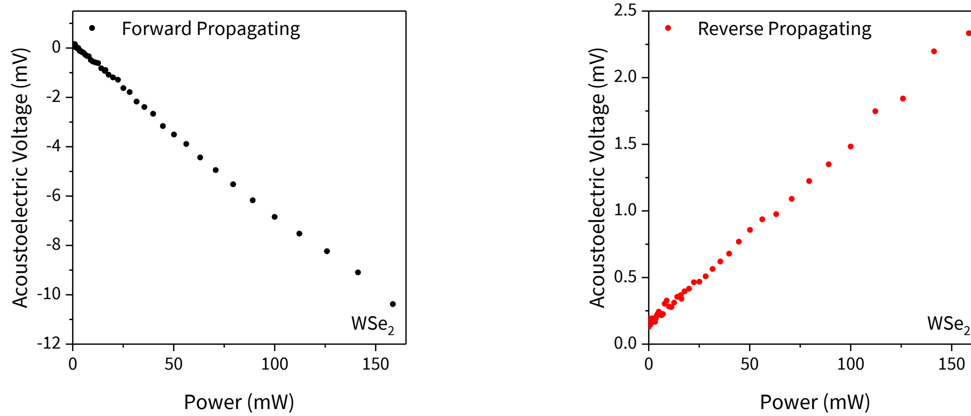

Figure 4.12 | Acoustoelectric voltage as a function of RF power (mW): Acoustoelectric voltage measured in a four-point, open-circuit configuration ($I_{SD} = 0$). Forward propagation (left) gives a negative value and a reverse propagation (right) gives a positive value, which is opposite the result seen for single-layer MoS_2.

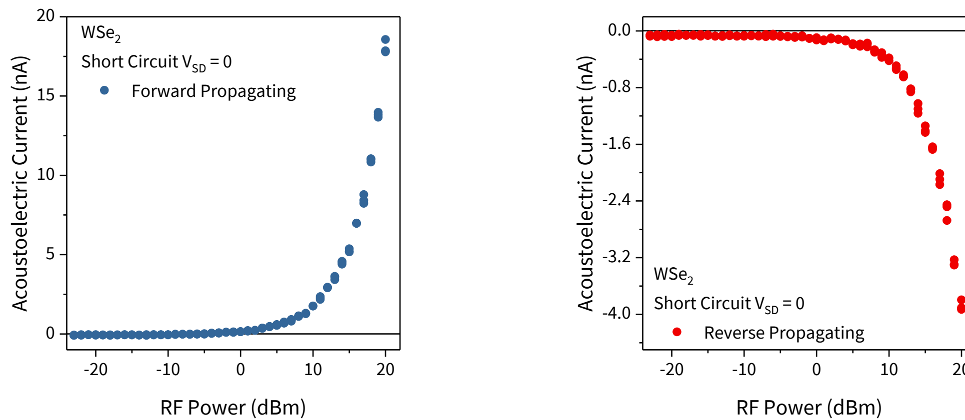

Figure 4.13 | Acoustoelectric current as a function of RF power (dBm): Positive acoustoelectric current forms for the forward propagating direction. The reverse effect occurs when switching the propagation direction, therefore attaining a negative acoustoelectric current. The signs of the acoustoelectric current and voltages correspond to p-type conductivity of the single-layer WSe_2 film.

4.5 References

[4.01] Radisavljevic, B., et al. (2011). "Single-layer MoS2 transistors." Nat Nanotechnol **6**(3): 147-150.

[4.02] Lee, K., et al. (2013). "High-performance sensors based on molybdenum disulfide thin films." Adv Mater **25**(46): 6699-6702.

[4.03] Nguyen, A., et al. (2015). "Toward Ferroelectric Control of Monolayer MoS2." Nano Lett **15**(5): 3364-3369.

[4.04] Bertolazzi, S., et al. (2013). "Nonvolatile memory cells based on MoS2/graphene heterostructures." ACS Nano **7**(4): 3246-3252.

[4.05] Movva, H. C., et al. (2015). "High-Mobility Holes in Dual-Gated WSe2 Field-Effect Transistors." ACS Nano **9**(10): 10402-10410.

[4.06] Ruppel, C. C. W., et al. (2002). "SAW devices and their wireless communications applications." IEEE Microwave Magazine **3**(2): 65-71.

[4.07] Zhao, W., et al. (2013). "Lattice dynamics in mono- and few-layer sheets of WS2 and WSe2." Nanoscale **5**(20): 9677-9683.

[4.08] Zhao, W., et al. (2013). "Evolution of electronic structure in atomically thin sheets of WS2 and WSe2." ACS Nano **7**(1): 791-797.

[4.09] O'Brien, M., et al. (2016). "Mapping of Low-Frequency Raman Modes in CVD-Grown Transition Metal Dichalcogenides: Layer Number, Stacking Orientation and Resonant Effects." Sci Rep **6**: 19476.

[4.10] Puretzky, A. A., et al. (2015). "Low-Frequency Raman Fingerprints of Two-Dimensional Metal Dichalcogenide Layer Stacking Configurations." ACS Nano **9**(6): 6333-6342.

[4.11] Del Corro, E., et al. (2016). "Atypical Exciton-Phonon Interactions in WS2 and WSe2 Monolayers Revealed by Resonance Raman Spectroscopy." Nano Lett **16**(4): 2363-2368.

[4.12] Schaufele, R. F. and M. J. Weber (1966). "Raman Scattering by Lithium Niobate." Physical Review **152**(2): 705-708.

[4.13] Liu, B., et al. (2015). "Chemical Vapor Deposition Growth of Monolayer WSe2 with Tunable Device Characteristics and Growth Mechanism Study." ACS Nano **9**(6): 6119-6127.

[4.14] Lui, C. H., et al. (2015). "Observation of interlayer phonon modes in van der Waals heterostructures." Physical Review B **91**(16).

[4.15] Clark, G., et al. (2014). "Vapor-transport growth of high optical quality WSe2 monolayers." APL Materials **2**(10): 101101.

[4.16] Pignatiello, F., et al. (2007). "Measurement of the thermal expansion coefficients of ferroelectric crystals by a moiré interferometer." Optics Communications **277**(1): 14-18.

[4.17] Okada, Y. and Y. Tokumaru (1984). "Precise determination of lattice parameter and thermal expansion coefficient of silicon between 300 and 1500 K." Journal of Applied Physics **56**(2): 314-320.

[4.18] Zhou, H., et al. (2015). "Large area growth and electrical properties of p-type WSe2 atomic layers." Nano Lett **15**(1): 709-713.

[4.19] Duan, X., et al. (2014). "Lateral epitaxial growth of two-dimensional layered semiconductor heterojunctions." Nat Nanotechnol **9**(12): 1024-1030.

[4.20] Huang, J. K., et al. (2014). "Large-area synthesis of highly crystalline WSe(2) monolayers and device applications." ACS Nano **8**(1): 923-930.

[4.21] Das, S. and J. Appenzeller (2013). "WSe2 field effect transistors with enhanced ambipolar characteristics." Applied Physics Letters **103**(10): 103501.

[4.22] Pradhan, N. R., et al. (2015). "Hall and field-effect mobilities in few layered p-WSe(2) field-effect transistors." Sci Rep **5**: 8979.

[4.23] Lee, S. T., et al. (2016). "Accurate extraction of WSe2 FETs parameters by using pulsed I-V method at various temperatures." Nano Convergence **3**(1).

[4.24] Chen, L., et al. (2014). "Screw-dislocation-driven growth of two-dimensional few-layer and pyramid-like WSe(2) by sulfur-assisted chemical vapor deposition." ACS Nano **8**(11): 11543-11551.

[4.25] Liu, B., et al. (2015). "Chemical Vapor Deposition Growth of Monolayer WSe2 with Tunable Device Characteristics and Growth Mechanism Study." ACS Nano **9**(6): 6119-6127.

[4.26] Gon Lee, Y., et al. (2013). "Influence of extrinsic factors on accuracy of mobility extraction in graphene metal-oxide-semiconductor field effect transistors." Applied Physics Letters **102**(9): 093121.

[4.27] Late, D. J., et al. (2012). "Hysteresis in single-layer MoS2 field effect transistors." ACS Nano **6**(6): 5635-5641.

[4.28] Rotter, M., et al. (1998). "Giant acoustoelectric effect in GaAs/LiNbO3 hybrids." Applied Physics Letters **73**(15): 2128-2130.

[4.29] Preciado, E., et al. (2015). "Scalable fabrication of a hybrid field-effect and acousto-electric device by direct growth of monolayer MoS2/LiNbO3." Nat Commun **6**: 8593.

5 Acoustic Photodetector MoS_2

5.1 Introduction

The acoustoelectric effect can be used for light-sensing applications by placing a thin, semiconducting film in close vicinity to the surface of a piezoelectric substrate. Upon illumination, photo-generated carriers interact with electric fields that are associated with SAW, resulting in an attenuation change. Therefore, a high-coupling coefficient substrate is essential for yielding a large acoustoelectric effect. In particular, $LiNbO_3$ offers a unique combination of substantial piezoelectric and birefringent properties. $LiNbO_3$ exhibits a large indirect bandgap of 3.95 eV, yet its lack of optical activity and semiconducting transport hamper application in optoelectronics [5.01]. For application as an optical sensor, hybridization with a lower bandgap material is of key relevance. Single-layer MoS_2 is an attractive candidate due to its direct bandgap and pronounced photoconductive response to optical (above bandgap) irradiation [5.02-04]. This unique response is the photoelectric effect, which earned Albert Einstein a Nobel Prize in Physics. This effect states [5.05]:

$$E_{photon} = \frac{hc}{\lambda} > E_{bandgap} \qquad \text{Equation 5.1}$$

Applying this response to single-layer MoS_2, the incident photon energy must be greater than the optical bandgap, or around 1.87 eV in single-layer MoS_2 [5.02].

$$E_{photon} = \frac{hc}{\lambda} > 1.87\ eV = \lambda_{photon} < \ 663\ nm$$ Equation 5.2

Only incident photons with a wavelength less than 663 nm can excite electrons from the valence band to the conduction band to generate a photocurrent. In our hybrid device, SAWs excited directly on the $LiNbO_3$ substrate induced a strong acoustoelectric effect and remotely sensed the photoconductance of single-layer MoS_2. Surface acoustic wave photoconductance spectroscopy can be performed at any point along the propagation path of a wave that extends on the millimeter length scale of a chip. This strongly contrasts with contact-based transport measurements, for which only the sample area between the contacts can be probed. A particularly exciting aspect of transport measurements using SAWs is their inherently contact-free nature, combined with their sensitivity to the limit of low conductivity. The transport properties reported for TMD materials, such as transconductance, carrier mobility, and susceptibility to gating, tend to vary widely, even for measurements on the same TMD material. From the perspective of technological application, this is highly undesirable. Charge transfer at the interface between metal contacts and the 2D TMD films, which results in band shifting/bending analogue to the formation of a Schottky barrier, has particularly been reported to affect transport measurements [5.06–08]. Therefore, SAW photoconductance spectroscopy is a powerful tool, since TMDs typically have a low conductivity. Here, the versatility and power of this approach is demonstrated through the measurement of photoconductivity of a single-layer MoS_2 film using the acoustoelectric effect.

5.2 Experimental Methods

The following section introduces all experimental methods used to measure the change in attenuation and photoconductance in our hybrid device setup. Experiments were performed in ambient temperature.

5.2.1 Measurement Techniques

Surface acoustic wave excitation and transmission experiments: The RF characteristics of the IDTs and SAW transmission lines were defined using a vector network analyzer. This measured scattering parameters of the RF network, and particularly the scattering parameter S_{21} (transmission and insertion loss).

Electrical characterization: Two-point characterization was performed using a Keithley K2400 source meter unit (SMU).

Optical spectroscopy: The photoconductivity experiments relied on red (660 nm) and infrared (850 nm) pulsed semiconductor lasers with a 80-MHz repetition rate and a pulse duration of 100 ps.

5.3 Experimental Results

Figure 5.1 presents a schematic of the hybrid device. The experimental methods section under lithographic patterning in Lithographic Patterning summarizes the fabrication process. The processed structures are composed of alignment markers, electrical contacts, and transducers. The markers are used as a global orientation for precise positioning of IDT structures, as well as to locally navigate throughout the sample. A 2D coordinate system can determine the position on the sample and thus estimate the distance to an IDT. This ensures that the location of the measurement is within the sound path. In order to avoid any distortion of the SAW field, the markers are always positioned outside of the sound paths.

5.3.1 SAW Attenuation

Surface acoustic waves in particular offer a versatile approach, as these nano-scale waves can be excited and detected on a chip and completely electronically [5.09-10]. For example, SAWs provide an extremely sensitive and fast conductivity (σ) probe and are particularly suitable for the characterization of poorly-

conductive films [5.11]. The attenuation and velocity modulation can be used to determine conductivity. Surface acoustic waves on a piezoelectric substrate are accompanied by a potential wave and generate an electric field, and they interact with the mobile carriers in a 2DEG in close vicinity to the surface. The semiconducting film influences the propagation of the SAW by changing the wave velocity and producing an attenuation of the wave. This interaction between the SAW and the charge carriers in a 2DEG is described using a simple classical relaxation model, where the SAW attenuation is given by:

$$\Gamma = K^2 \frac{\pi}{\lambda}\left[\frac{\left(\frac{\sigma_{2D}}{\sigma_M}\right)}{1+\left(\frac{\sigma_{2D}}{\sigma_M}\right)^2}\right] \qquad \text{Equation 5.3}$$

In this expression, Γ is the attenuation per unit length, $K^2 = 0.056$ is the electromechanical coupling efficiency, λ is the SAW wavelength, σ_{2D} is the sheet conductivity of single-layer MoS_2, and σ_M is the characteristic sheet conductivity of the piezoelectric substrate [5.11].

We can determine characteristic sheet conductivity σ_M with the following equation:

$$\sigma_M = v_{SAW}\, \varepsilon_0(\varepsilon_r + 1) \qquad \text{Equation 5.4}$$

Here, v_{SAW} is the propagation velocity of $LiNbO_3$, ε_0 is permittivity of free space, and ε_r is the relative permittivity of the $LiNbO_3$. The value for the characteristic sheet conductivity is $1.8 \times 10^{-6}\ \Omega^{-1}$. The characteristic channel conductance corresponds with the characteristic sheet conductivity σ_M and is determined below:

$$G_M = \sigma_M \frac{W}{L} \qquad \text{Equation 5.5}$$

This value corresponds with a characteristic channel conductance of ~ 18.5 µS in our device. The value is larger than the measured channel conductance G < 1.2 µS from the FET characteristics in Figure 3.12.

5.3.2 SAW Transmission Photoresponse of Single-Layer MoS_2

The following section reviews the optical response of single-layer MoS_2 on a piezoelectric substrate. Characterizing the SAW transmission along the delay line was achieved by measuring the S_{21} scattering parameter – i.e., the transmitted SAW intensity from one IDT to the other, as seen in Figure 5.2. A minimum insertion loss value of – 25.2 dB was measured using a vector network analyzer.

Figure 5.3 plots the variation of S_{21} as a function of time. At t = 6 s, a diffraction-limited spot in the center of the hybrid device is irradiated for $\Delta t = 5$ s by either a red ($h\nu = 1.87$ eV) or an infrared laser ($h\nu = 1.46$ eV) source at 1 mW power. Surface acoustic wave attenuation induced by the acoustoelectric effect is measured by the change of insertion loss, where the insertion loss difference with and without laser illumination is subtracted. The red laser is resonant with the fundamental optical transition of single-layer MoS_2 on $LiNbO_3$, while the photon energy of the infrared laser is less than the optical bandgap of single-layer MoS_2. A pronounced photoresponse is resolved for the red laser, manifesting in a reduction of the transmitted SAW signal ($\Delta S_{21} < 0$). Such an increase of the attenuation is expected from Equation 5.3, since photogeneration of electrons and holes leads to an increase in G, while still remaining within the $G \ll G_m$ regime. For the infrared laser, no variation of the SAW attenuation was resolved, corroborating that the observed response indeed arises from photogenerated carriers in the MoS_2.

5.3.3 Photoconductance of Single-Layer MoS_2

This interpretation is confirmed by simultaneously measuring the electrical conductivity in a two-point configuration, which is plotted in Figure 5.4. The anticipated increase of the conductance ($\Delta G > 0$) is clearly resolved. The agreement of the global features of ΔS_{21} and ΔG is remarkable; both channels indicate quasi-instantaneous responses as the laser is switched on and off, which is attributed to the presence or absence of photogenerated carriers in the MoS_2 layer. The associated processes occur on a timescale faster than the

acquisition time of each data point of 250 ms. In addition to this fast contribution, a response on longer (seconds to minutes) timescales is clearly resolved [5.03].

5.3.4 Optical Pump Series of Single-Layer MoS_2

This section presents a detailed optical pump power series. In this experiment, the laser source was repeatedly switched on for 5 seconds every minute. The optical pump power was initially increased in ΔP_{Laser} = 0.1 mW steps, from P_{Laser} = 0.1 – 1 mW, and then reduced to P_{Laser} = 0 mW. The corresponding optical power pattern is plotted in Figure 5.5. The upper and center panels compare the measured SAW (ΔS_{21}) and current (I_{SD}) responses for V_{SD} = +100 mV (Figure 5.6) and −100 mV (Figure 5.7), respectively. Clearly, both the SAW attenuation and the FET current scale with the laser power in a nonlinear manner, which is similar to the observations of Yin et al. [5.02] and Lopez-Sanchez et al. [5.04], but different from the short-channel devices of ref. [5.03]. While the sign of I_{SD} depends on the polarity of V_{SD}, ΔS_{21} decreases irrespective of the V_{SD} polarity. Furthermore, the amplitude of ΔS_{21} only depends on P_{Laser} and is independent of the applied V_{SD}. These facts prove that electro-acoustic and FET operation do not interfere. The component of the photoresponse with the longer time constant [5.03] leads to the accumulation of higher sheet conductivity over the full 20-minute duration of the experiment. Such processes are frequently observed in 2D materials and are typically attributed to traps at the interface to the substrate or in the material itself. In ref [5.03], we demonstrate the composition dependence of the phenomenon for S- and Se-based alloys.

5.4 Conclusion

The agreement of the global features of ΔS_{21} and ΔG is remarkable. Both channels show quasi-instantaneous responses as the laser is switched on and off, which is attributed to the presence or absence of photogenerated carriers in the MoS_2 layer. Direct correspondence between S_{21} and I_{SD} is confirmed; while

the S_{21} reduces irrespectively of voltages, the sign of I_{SD} is determined by the polarity of V_{SD}. SAW-based devices will ultimately have the power to provide contact-free measurements, thus opening a new avenue to gain insight into this current issue. The findings of this study suggest foreseeable non-invasive investigation of electrical properties of monolayer films in the near future.

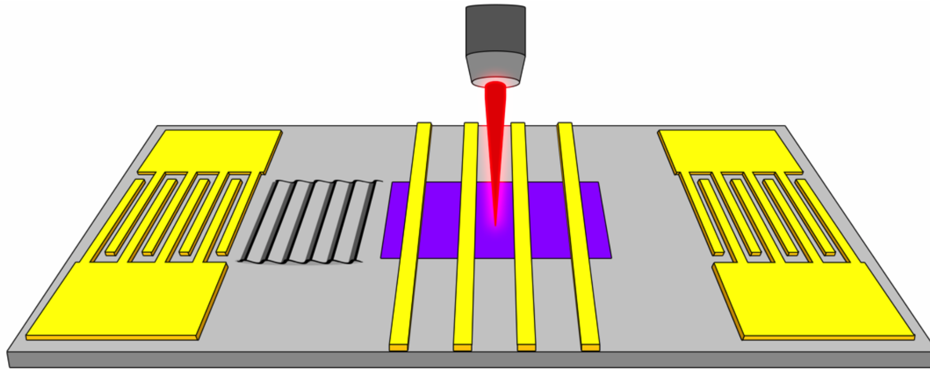

Figure 5.1 | Schematic representation of the hybrid MoS_2/$LiNbO_3$ device: Four Ti/Au electrodes form the contacts of a FET fabricated on CVD-grown single-layer MoS_2. Two opposing, non-impedance matched IDTs are used to excite SAWs across the propagation path. The sample was excited optically using 50x objective microscope with a numerical aperture (NA) of 0.55

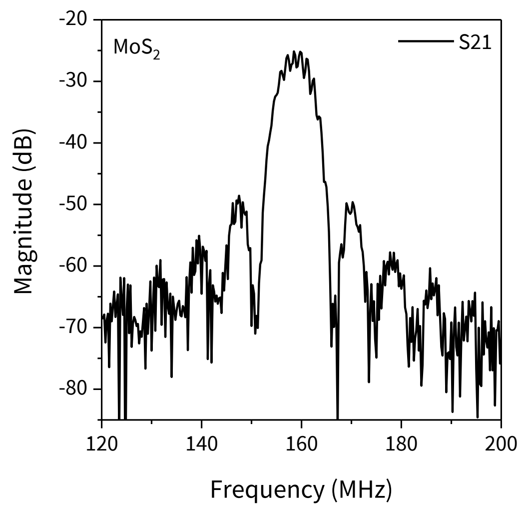

Figure 5.2 | Transmission parameter: Frequency band of the SAW transmission between IDTs plotted as the scattering parameter S_{21}

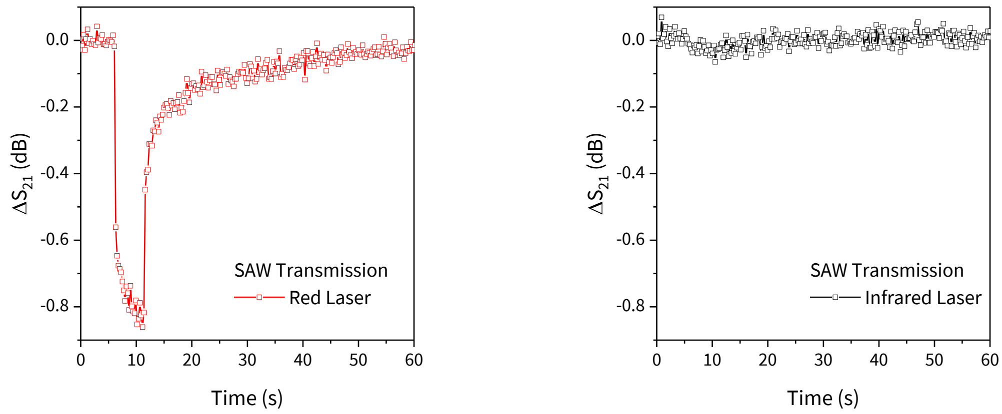

Figure 5.3 | Comparison of the time-dependent photoresponse detected by the change of the transmitted SAW intensity (ΔS_{21}): Red (left) and black (right) traces were recorded for laser power of 1 mW excitation by a red and infrared laser, respectively. These lasers are switched on for five seconds. No photoresponse detected by the infrared laser while the red laser has a profound photoresponse.

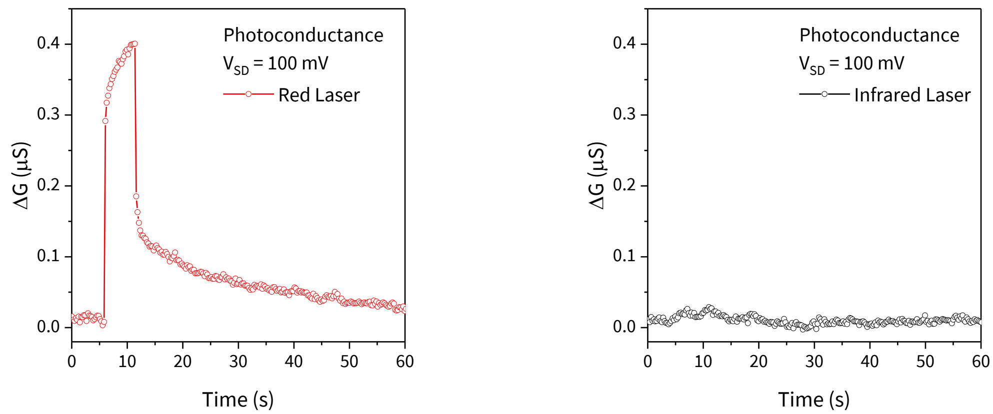

Figure 5.4 | Comparison of the time-dependent photoresponse detected by the change of the two-point conductance (ΔG) of the FET: Red (left) and black (right) traces were recorded for laser power of 1 mW excitation by a red and infrared laser, respectively. These lasers are switched on for $\Delta t = 5$ s at $t = 6$ s. Both the instantaneous and persistent features of the photoresponse are consistently resolved by both the SAW transmission and conductance. For excitation with an infrared laser, no photoresponse is detected, p roving that the signal detected for the red laser indeed stems from the single-layer MoS_2

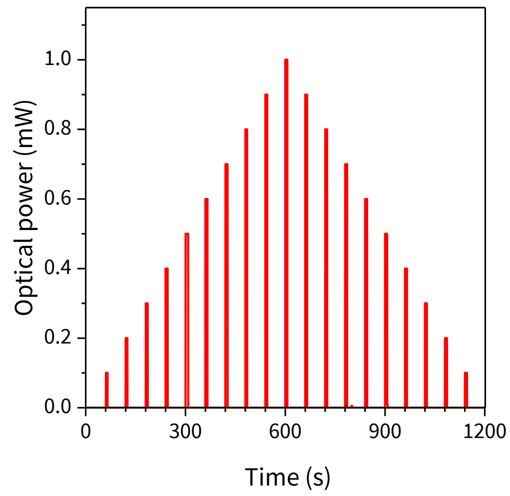

Figure 5.5 | Laser power: The laser is switched on every 1 minute for Δt = 5 s. Each successive minute P_{laser} is increased 0.1 mW until P_{laser} = 1 mW is reached. Subsequently, P_{laser} is decreased to 0 mW in steps of Δ P_{laser} = 0.1 mW.

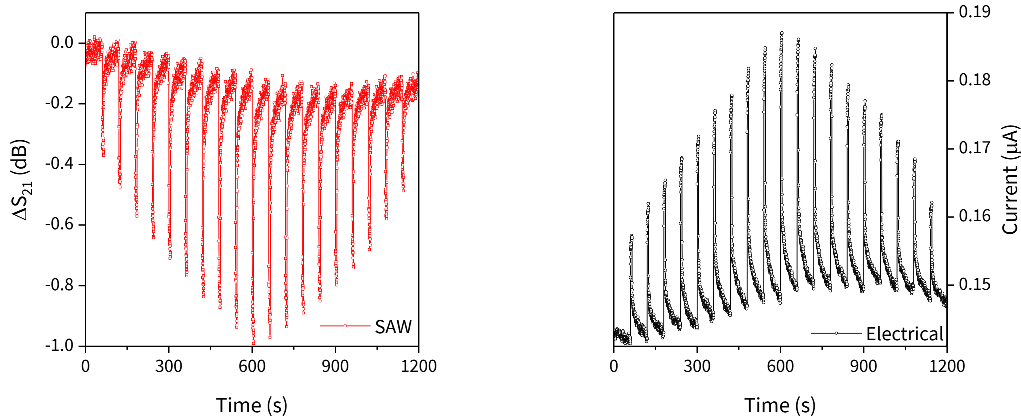

Figure 5.6 | Comparison of SAW transmission (ΔS_{21}) and photocurrent (I_{SD}) at V_{SD} = + 100 mV

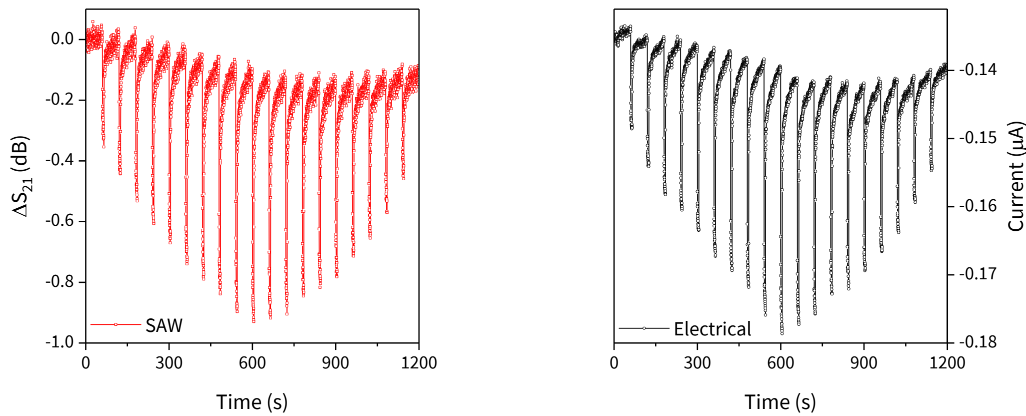

Figure 5.7 | Comparison of SAW transmission (ΔS_{21}) and photocurrent (I_{SD}) at V_{SD} = – 100 mV

5.5 References

[5.01] Bhatt, R., et al. (2012). "Urbach tail and bandgap analysis in near stoichiometric LiNbO3 crystals." physica status solidi (a) **209**(1): 176-180.

[5.02] Yin, Z., et al. (2012). "Single-layer MoS2 phototransistors." ACS Nano **6**(1): 74-80.

[5.03] Klee, V., et al. (2015). "Superlinear composition-dependent photocurrent in CVD-grown monolayer MoS2(1-x)Se2x alloy devices." Nano Lett **15**(4): 2612-2619.

[5.04] Lopez-Sanchez, O., et al. (2013). "Ultrasensitive photodetectors based on monolayer MoS2." Nat Nanotechnol **8**(7): 497-501.

[5.05] CITE.

[5.06] Pradhan, N. R., et al. (2013). "Intrinsic carrier mobility of multi-layered MoS2 field-effect transistors on SiO2." Applied Physics Letters **102**(12): 123105.

[5.07] Chen, J. R., et al. (2013). "Control of Schottky barriers in single layer MoS2 transistors with ferromagnetic contacts." Nano Lett **13**(7): 3106-3110.

[5.08] Yoon, Y., et al. (2011). "How good can monolayer MoS(2) transistors be?" Nano Lett **11**(9): 3768-3773.

[5.09] Rotter, M., et al. (1998). "Giant acoustoelectric effect in GaAs/LiNbO3 hybrids." Applied Physics Letters **73**(15): 2128-2130.

[5.10] Wixforth, A., et al. (1989). "Surface acoustic waves on GaAs/AlxGa1−xAs heterostructures." Physical Review B **40**(11): 7874-7887.

[5.11] Wixforth, A., et al. (1986). "Quantum oscillations in the surface-acoustic-wave attenuation caused by a two-dimensional electron system." Phys Rev Lett **56**(19): 2104-2106.

[5.12] Preciado, E., et al. (2015). "Scalable fabrication of a hybrid field-effect and acousto-electric device by direct growth of monolayer MoS2/LiNbO3." Nat Commun **6**: 8593.

6 Conclusion

6.1 Concluding Remarks

The work presented in this thesis is focused on the interaction of single-layer MoS_2 and WSe_2 with SAWs. Numerous intriguing phenomena stemming from SAWs have previously been used to non-invasively probe low-dimensional systems, such as quantum dots and 2DEGs. One such 2DEG system is TMDs, which offer many opportunities owing to its strong PL, significant spin-orbit coupling, and carrier mobility, which is competitive with silicon. It should be noted that although CVD growth of TMDs was developed on various substrates rather easily, relatively little work has been produced to date on piezoelectric substrates. The importance of a piezoelectric substrate is to utilize the direct and indirect piezoelectric effect in order to generate and detect propagating waves. To this end, single-layer MoS_2 and WSe_2 were independently grown on piezoelectric $LiNbO_3$ via CVD to measure the SAW interaction, which has been addressed in this work. Hybrid devices studied here were fabricated using e-beam lithography and e-beam evaporation to pattern and metallize, respectively. The major significance of this work is that this device is peculiar, as both FET functionality and SAW response were observed. Experimental cross-validation of the respective signals were measured. When the input IDT was placed under RF excitation, periodic SAWs on the piezoelectric substrate generated accompanying electric fields that interacted with charge carriers present in the semiconducting TMD. Direct measurements of the acoustoelectric current of single-layer TMDs were performed by SAW spectroscopy. In this effect, SAWs trap charge carriers in their potential minima and

generate DC current along the propagation direction of the SAW. The observed polarities provide an independent verification of majority charge carriers in the TMD film. The FETs tested at room temperature exhibited n-type and p-type behavior for single-layer MoS_2 and WSe_2 films, respectively. With regards to silicon-based counterparts, hybrid devices of single-layer MoS_2 and WSe_2 on $LiNbO_3$ exhibit comparable field-effect mobilities. Additionally, SAW transmission measurements demonstrated that single-layer MoS_2 could be used as an acoustic photodetector platform. Quasi-instantaneous response by direct measurement of photoconductivity and SAW transmission was achieved.

6.2 Future Directions

This work will contribute to future studies of 2D semiconducting materials in the TMD family, such as ReS_2 and $MoTe_2$. These materials are exceptional in nature due to their single-layer nature, which are just three atoms thick. Such materials hold tremendous opportunities for the next generation of devices in the semiconductor industry because they offer unique properties that are unlike the silicon standard, which is limited by its bulk size. This research has explored various novel strategies, such as SAW spectroscopy, through a method that implemented the use of electrical contacts to measure acoustoelectric response. Alternatively, and as evidenced by the SAW transmission measurements in Acoustic Photodetector MoS_2, these measurements can be applied by generating SAWs and using a laser source to provide insight into transport properties modulations. Future measurements can be accomplished in absence of electrical contacts. This would be a breakthrough for 2D TMDs since they possess a particular set of problems that is associated with the absence of any bulk of the material. In a bulk material, electrical contacts can affect the properties of the material locally, but over some distance, the bulk of the materials shields this perturbation. In 2D TMDs, there is no bulk; hence, little shielding and the nature of the contacts dominate the observed transport properties. Using SAWs is a way to avoid this, as these can be measured without any contacts. Surface acoustic waves do not affect the material's conductivity significantly because they propel

charge carriers, such as electrons, through the material. Energy is sourced from the SAW in the piezoelectric substrate and converted into the acceleration of electrons, which is then dissipated by the finite conductivity of 2D TMDs. This approach would utilize SAWs generated and detected by IDTs that are spaced away from the 2D TMD film. Optical excitation is used on the area of interest of the film to generate photoconductance and SAW attenuation spatial maps of all sorts of TMDs that rival measurements such as spatial PL maps. This allows the exploration of different TMDs and an ultimate understanding of their properties and limitations. Such properties include the impact of grain boundaries and other material perturbations on the local conductivity. Future research should develop a foundation for uncovering charge carrier transport in 2D semiconducting TMDs without the use of electrical contacts. This permits a different analytical technique that would allow SAWs to study the electronic properties of a variety of novel nanoscale 2D TMDs.